University of California
Santa Barbara

Tractable Quantification of Metastability for Robust Bipedal Locomotion

A dissertation submitted in partial satisfaction
of the requirements for the degree

Doctor of Philosophy
in
Electrical and Computer Engineering

by

Cenk Oguz Saglam

Committee in charge:

Professor Katie Byl, Chair
Professor Andrew R. Teel
Professor Joao P. Hespanha
Professor Bassam Bamieh
Professor Art Kuo

June 2015

The Dissertation of Cenk Oguz Saglam is approved.

_____

Professor Andrew R. Teel

_____

Professor Joao P. Hespanha

_____

Professor Bassam Bamieh

_____

Professor Art Kuo

_____

Professor Katie Byl, Committee Chair

June 2015

Tractable Quantification of Metastability

for Robust Bipedal Locomotion

Copyright © 2015

by

Cenk Oguz Saglam

To my dear family.

Without you, none of this would've been possible.

Acknowledgements

I am deeply grateful to my advisor Professor Katie Byl for coming up with such a fun topic and providing me with ready-to-be-explored research questions, and the most productive, yet comfortable, laboratory environment for me. Thanks to her support, I got to enjoy my research with a great independence during all my studies at the University of California, Santa Barbara.

I am also thankful to all the members of my thesis committee. Professor Andy Teel has always been easy-to-reach and encouraging all along. I would also like to thank Professor Joao Hespanha for his invaluable comments both for my research and career. I appreciate Professor Bassam Bamieh for being available in my committee on such short notice. I am also honored to have a leading and inspiring researcher of legged locomotion community like Professor Art Kuo in my committee.

I have always been a proud member of the UCSB Robotics Lab along with Pat Terry, Chelsea Lau, Sebastian Sovero, Giulia Piovan, Tom Strizic, Brian Satzinger, Hosein Mahjoubi, and Greg Ray.

I feel very fortunate to meet with so many great people in Santa Barbara. My journey here started with Alp Yucebilgin as my roommate and continued within a comforting group formed by Deniz Akdolu, Nazli Dereli, Emre Gul. Back in the days when our algorithms were relatively slow, Emre's suggestion to use a computer cluster in computation greatly sped up my progress. As a member of the "Turkish Village", I gained a whole new perspective with Bugra Kaytanli, Cetin Sahin, Faruk Gencel, Semih Yavuz, Onur Sinan Koksaldi, and Omer Ali Acerol. Moreover, thanks to Selim Dogru, a former member of our village, I will be transitioning to the next step in my career at Intel. In particular, I really appreciate Bugra's support as I have been preparing for the next chapter in my life. Whenever I needed, he devotedly edited numerous texts, including my state-

ments, emails, presentations - practically everything, including this sentence (You are most welcome Oguz).

Of course I would like to thank my beloved family: Abdullah, Cansin, and Aybike Saglam. Literally (and I mean this) without them I would almost certainly not have existed. Also without the support of all the members of my family, including my cousins Burak and Oguz Demirci, this work would not have been possible. I would also like to thank Beril Pisgin for supporting me from the other side of the earth all these years.

Curriculum Vitæ
Cenk Oguz Saglam

Education

2013-2015   **University of California, Santa Barbara**
Ph.D. in Electrical and Computer Engineering
GPA **4.0/4.0**

2011-2013   **University of California, Santa Barbara**
M.S. in Electrical and Computer Engineering
GPA **4.0/4.0**

Summer 2009   **University of California, Los Angeles**
Summer Session in Mechanical and Aerospace Engineering
& Mathematics
GPA **4.0/4.0**

2007-2011   **Sabanci University**, Istanbul
B.S. in Mechatronics Engineering
Minor in Mathematics
GPA **3.88/4.0**
Major GPA: **3.96/4.00**

Publications

Cenk Oguz Saglam and Katie Byl. Meshing Hybrid Zero Dynamics for Rough Terrain Walking. In *Proc. of IEEE International Conference on Robotics and Automation (ICRA)*, May 2015.

Cenk Oguz Saglam and Katie Byl. Metastable Markov Chains. In *IEEE Conference on Decision and Control (CDC)*, December 2014.

Cenk Oguz Saglam, Andrew Teel and Katie Byl. Lyapunov-based versus Poincaré Map Analysis of the Rimless Wheel. In *IEEE Conference on Decision and Control (CDC)*, December 2014.

Cenk Oguz Saglam and Katie Byl. Quantifying the trade-offs between stability versus energy use for underactuated biped walking. In *IEEE/RSJ International Conference on Intelligent Robots and Systems (IROS)*, 2014.

Cenk Oguz Saglam and Katie Byl. Robust policies via meshing for metastable rough terrain walking. In *Proc. of Robotics: Science and Systems (RSS)*, July 2014.

Cenk Oguz Saglam and Katie Byl. Switching policies for metastable walking. In *Proc. of IEEE Conference on Decision and Control (CDC)*, pages 977-983, December 2013.

Cenk Oguz Saglam and Katie Byl. Stability and gait transition of the five-link biped on stochastically rough terrain using a discrete set of sliding mode controllers. In *Proc. of IEEE International Conference on Robotics and Automation (ICRA)*, pages 5675-5682, May 2013.

Cenk Oguz Saglam, Eray A. Baran, Ahmet O. Nergiz and Asif Sabanovic. Model Following Control with Discrete Time SMC for Time-Delayed Bilateral Control Systems. In *Proc. of IEEE International Conference on Mechatronics (ICM)*, pages 997-1002, April 2011.

Abstract

Tractable Quantification of Metastability

for Robust Bipedal Locomotion

by

Cenk Oguz Saglam

This work develops tools to quantify and optimize performance metrics for bipedal walking, toward enabling improved practical and autonomous operation of two-legged robots in real-world environments. While speed and energy efficiency of legged locomotion are both useful and straightforward to quantify, measuring robustness is arguably more challenging and at least as critical for obtaining practical autonomy in variable or otherwise uncertain environmental conditions, including rough terrain. The intuitive and meaningful robustness quantification adopted in this thesis begins by stochastic modeling of disturbances such as terrain variations, and conservatively defining what a failure is, for example falling down, slippage, scuffing, stance foot rotation, or a combination of such events. After discretizing the disturbance and state sets by meshing, step-to-step dynamics are studied to treat the system as a Markov chain. Then, failure rates can be easily quantified by calculating the expected number of steps before failure. Once robustness is measured, other performance metrics can also be easily incorporated into the cost function for optimization.

For high performance and autonomous operation under variations, we adopt a capacious framework, exploiting a hierarchical control structure. The low-level controllers, which use only proprioceptive (internal state) information, are optimized by a derivative-free method without any constraints. For practicability of this process, developing an algorithm for fast and accurate computation of our robustness metric was a crucial and

necessary step. While the outcome of optimization depends on capabilities of the controller scheme employed, the convenient and time-invariant parameterization presented in this thesis ensures accommodating large terrain variations. In addition, given environment estimation and state information, the high-level control is a behavioral policy to choose the right low-level controller at each step. In this thesis, optimal switching policies are determined by applying dynamic programming tools on Markov decision processes obtained through discretization. For desirable performance in practice from policies that are formed using meshing-based approximation to the true dynamics, robustness of high-level control to environment estimation and discretization errors are ensured by modeling stochastic noise in the terrain information and belief state while solving for behavioral policies.

This thesis includes the following publications:

- ©2013 IEEE. Reprinted, with permission, from Cenk Oguz Saglam and Katie Byl. Meshing Hybrid Zero Dynamics for Rough Terrain Walking. In *Proc. of IEEE International Conference on Robotics and Automation (ICRA)*, May 2015.

- ©2013 IEEE. Reprinted, with permission, from Cenk Oguz Saglam and Katie Byl. Metastable Markov Chains. In *IEEE Conference on Decision and Control (CDC)*, December 2014.

- ©2013 IEEE. Reprinted, with permission, from Cenk Oguz Saglam, Andrew Teel and Katie Byl. Lyapunov-based versus Poincaré Map Analysis of the Rimless Wheel. In *IEEE Conference on Decision and Control (CDC)*, December 2014.

- ©2013 IEEE. Reprinted, with permission, from Cenk Oguz Saglam and Katie Byl. Quantifying the trade-offs between stability versus energy use for underactuated biped walking. In *IEEE/RSJ International Conference on Intelligent Robots and Systems (IROS)*, 2014.

- Reprinted, with permission, from Cenk Oguz Saglam and Katie Byl. Robust policies via meshing for metastable rough terrain walking. In *Proc. of Robotics: Science and Systems (RSS)*, July 2014.

- ©2013 IEEE. Reprinted, with permission, from Cenk Oguz Saglam and Katie Byl. Switching policies for metastable walking. In *Proc. of IEEE Conference on Decision and Control (CDC)*, pages 977-983, December 2013.

- ©2013 IEEE. Reprinted, with permission, from Cenk Oguz Saglam and Katie Byl. Stability and gait transition of the five-link biped on stochastically rough terrain

using a discrete set of sliding mode controllers. In *Proc. of IEEE International Conference on Robotics and Automation (ICRA)*, pages 5675-5682, May 2013.

Contents

List of Figures

List of Tables

Chapter 1

Introduction

Over the past few decades, a variety of control methods have made robots quite reliable in deterministic factory settings. One of the central challenges in robotics today is to attain robust performance under the variations[1] implied by real-world conditions. To achieve robustness for reliable operation in less-structured environments, quantification and optimization of relevant performance metrics are essential tasks. Ideally, a robot should also utilize information about the environment and modify its motion accordingly to maximize stability and autonomy.

Although the methods presented in this thesis are potentially applicable to autonomous wheeled vehicles, robotic manipulators, and a broader class of hybrid dynamical systems in general, the focus is on legged locomotion. In particular, we study two-legged under-actuated robots walking on rough terrain, for which measuring and achieving stability is still a major challenge.

While mobility is an undeniable necessity for various robotic applications, one motivation for bipedal robot walking is that this anthropomorphic approach provides powerful

---

[1] As explained by [Smith, 2012], variations can be categorized as *variability*, which means "natural variation in some quantity", and *uncertainty*, which refers to "the degree of precision with which a quantity is measured" [Belle, 2008].

means for negotiating intermittent or otherwise rough terrain, where wheels would be ineffective. Bipeds have the capability of moving on steep slopes, climbing ladders, varying their step width, passing narrow passages, easily turning corners, walking on a tightrope, avoiding obstacles, and traversing with small footprints. Developments in bipedal locomotion research will enable replacing humans in hazardous jobs, assisting people in difficult or time consuming tasks, providing better prostheses for the disabled, and rehabilitating the injured.

1.1   Stability Measurement for Bipedal Robots

Designing and comparing various robotic hardware and/or control schemes require evaluation of performance using appropriate metrics. In particular, measuring success of legged locomotion is essential toward developing more capable bipedal robots. Although the performance of highly-dynamic walkers is often quantified by speed or energy consumption [Hobbelen and Wisse, 2007], these qualities are tangentially meaningful if the robot is likely to fall in several steps. For reliable operation, the stability of walking must be measured and increased. Once a robot can walk in an unlikely-to-fall manner, other metrics such as speed and energy efficiency can be easily incorporated. As an example application, control can be optimized to maximize the probability of traversing a particular terrain with a desired speed and given limited energy capability.

There are two mainstream approaches to bipedal robot design. One approach relies heavily on ankle torque for balance. By using an appropriately large foot as a base of support, such robots can be model as fully actuated under carefully controlled operating conditions. The other approach deliberately uses an underactuated ankle. Without ankle torque, balance control requires more careful planning, but it also enables more dynamic gaits, with smaller footholds, better energy efficiency, and potentially greater capabilities

in regimes where large perturbations to a robot would cause either approach to become underactuated at the ground contact. The differences in these two approaches' design principles lead to qualitatively distinct walking motions and numerous metrics have been proposed to quantify their stability [Pratt et al., 2001], [Santos et al., 2007], [Hobbelen and Wisse, 2007], [Byl, 2008], some of which are summarized next.

1.1.1   Flat Footed Humanoids

Many well known and very capable humanoids, including the robots shown in Figure 1.1, are designed to have large feet to make locomotion task relatively easier. Although humans roll their feet while walking for energy efficiency, these humanoids are often controlled aiming to keep at least one foot flat on the ground at all times. In other words, the objective is to prevent the foot on the ground from rotating to model robot as fully actuated. Multiple methods are proposed to achieve such a balance. As [Sugihara, 2009] explains, these balance criteria are often used to show stability. However, we will later argue that distinguishing the two is an important step toward human-like walking robots.

The most elementary approach to balancing is ignoring the kinematics and dynamics of the system and modeling the robot as a mass with a support polygon[2] as shown in Figure 1.2. In case the projection of this mass' location to the ground surface is within the support polygon, the robot is statically stable. Although this approach is appealing because of its simplicity, given the dynamics of a walker, static stability is neither necessary nor sufficient condition for keeping the foot flat or walking stably.

Static stability margin concept has been modified in various ways to consider the kinematics and dynamics of the robot. One extension, which has lead to the most popular stability metric overall today, focuses on the center of pressure (CoP) on the foot instead

---

[2]Convex hull formed by the contacts between the feet and the ground [Tedrake, 2004]. In the 2D case, support polygon is a line, e.g., AB in Figure 1.2.

(a) ASIMO   (b) ATLAS   (c) HUBO

(d) SURALP   (e) NAO   (f) Darwin

Figure 1.1: Some state-of-the-art bipedal robots with large feet. ASIMO, ATLAS, HUBO and SURALP are human sized robots built for research purposes. NAO and Darwin are smaller bipeds which are commercially available.

ASIMO and ATLAS images are permitted for non-commercial use by American Honda Motor Company and The Defense Advanced Research Projects Agency (DARPA) respectively. HUBO is manufactured by Korea Advanced Institute of Science and Technology (KAIST) and its image is taken from http://dailyscene.com/wp-content/uploads/2011/12/Hubo.jpg. Prof. Kemalettin Erbatur from Sabanci University of Turkey kindly permitted the use of SURALP image. Aldebaran Robotics is the manufacturer of NAO and its image is obtained from http://hcr.mines.edu/images/NaoStand.png. Use of DARWIN image is permitted by ROBOTIS Incorporation.

(a) A statically stable object. Static stability margin is given by min(PA, PB), the minimum distance from P to the edges of the support polygon.

(b) A statically unstable object. Static stability margin is given by -PB, minus the minimum distance from P to the edges of the support polygon.

Figure 1.2: Illustration of static stability in 2D. CoM denotes the center of mass. P shows the projection of the CoM. AB, the line segment formed by points A and B, corresponds to the support polygon. If P is in (outside) AB, then the object is statically stable (unstable).

of the center of mass location [Vukobratovic and Borovac, 2004]. As shown in Figure 1.3, if the CoP is strictly inside the footprint, then the foot does not rotate and the robot is balanced. In this case CoP is equivalent to the zero moment point (ZMP).

(a) ZMP criterion is met (center of pressure is strictly within footprint). As a result, the foot does not rotate.

(b) The foot is rotated and the robot touches the ground only at a point. Then this point is where the ZMP acts.

Figure 1.3: Zero moment point criterion. P denotes the center of pressure acting on the foot. If P is strictly within footprint, then the ZMP criterion is satisfied and the foot does not rotate. ZMP based controllers aim at keeping at least one foot flat on the ground.

[Goswami and Kallem, 2004] generalizes ZMP concept by proposing a criterion based on angular momentum to preserve the balance. Algorithms based on linear and angular momentum have shown to be useful in whole body motion planning and control [Ugurlu and Kawamura, 2012] [Orin et al., 2013] [Kajita et al., 2003].

Although humanoids are typically controlled to preserve balance to establish stability, one idea in this thesis is that stability is different than balance. In human-like walking, each step is basically an intentional "fall" onto the next foot. Avoiding underactuation for bipeds often results in energy inefficiency. Indeed, the cost of transport[3] (CoT) is estimated to be 0.2 for humans and 3.2 for the infamous humanoid ASIMO shown in Figure 1.1a [Collins et al., 2005]. On the other hand, [Kuo, 2007] explains that serious advances in control are necessary to achieve the high versatility of robots like ASIMO while being as energy efficient as the walkers of next section.

1.1.2   Dynamic Walkers

Toward developing more energy efficient, dynamic, fast, agile and humanlike walking robots, Tad McGeer has been inspirational by showing that even passive bipeds (two-legged walkers that have no motors) can walk downhill in a stable manner using gravitational forces [McGeer, 1990]. A passive robot built by [Collins et al., 2001] is depicted in Figure 1.4a. A key and revolutionary aspect of these machines is that part of their walking cycle is unbalanced, but the overall walking motion is stable. This property, which is ambiguously termed as *dynamic walking*, has pioneered a major trend in bipedal locomotion research, where one of the main goals is exploiting underactuation[4] like humans rather than avoiding it as in flat footed walking.

---

[3]The non-dimensionalized energy expenditure per unit weight and unit distance [Tucker, 1975].

[4]lack of ability to control all degrees-of-freedom. Approximately, the robot in Figure 1.3a is fully actuated, but it is underactuated in Figure 1.3b.

Inspired by passive walkers, researchers have demonstrated a range of powered walkers based on exploiting natural dynamics, and the approach has led to record-breaking performance in walking with only onboard power (energetically autonomous) [Bhounsule et al., 2014]. Figure 1.4b illustrates the Cornell powered biped designed by [Collins and Ruina, 2005], which is as energy efficient as humans [Collins et al., 2005].

Although these walkers have been groundbreaking, robots that are designed dominantly for energy efficiency are typically sensitive to perturbations, thus they do not perform as well as flat footed robots like ASIMO on rough terrain. To close the gap, various dynamic walkers have been designed for better rough terrain capabilities, three of which are depicted in the bottom row of Figure 1.4. RABBIT has been a prominent test bed for theory both in simulation and experiments [Chevallereau et al., 2003]. This robot was later followed by MABEL, which proved to be a much more capable hardware on rough terrain [Grizzle et al., 2009]. Using booms, these two robots were constrained to walk in 2 dimensional space to tackle the problem of understanding underactuated walking. A more recent point-footed walker is ATRIAS [Hurst, 2015a], which very recently showed the ability to walk in 3D [Hurst, 2015b]. Notice that all three robots are underactuated because they have point feet to emulate the foot rolling in human locomotion. Once the relatively more complicated task of robust walking with no real feet is achieved, the addition of complex feet and ankle torque only helps toward making the robot more stable and capable.

Under deterministic conditions, dynamic bipeds exhibit locally stable limit cycles that repeat once per step. The stability under disturbances is then often studied by local approximations on these limit cycles by investigating deviations from the trajectories (gait sensitivity norm [Hobbelen and Wisse, 2007], H_∞ cost [Morimioto et al., 2003], and L2 gain [Dai and Tedrake, 2013]), or the speed of convergence back after such deviations (using Floquet theory [Hurmuzlu and Basdogan, 1994], [McGeer, 1990]).

(a) Passive walker   (b) Cornell powered biped

(c) RABBIT   (d) MABEL   (e) ATRIAS

Figure 1.4: Some robots that do not maintain static stability while exhibiting stable walking motion on deterministic terrain.

Professor Andy Ruina kindly allowed the use of the passive walker and Cornell powered biped images. RABBIT was designed and constructed at the Control Department of GIPSA-Lab (CNRS), at Grenoble France. Professor Carlos Canudas de Wit, Professor Jessy Grizzle, and Professor Jonathan Hurst permitted using the images of RABBIT, MABEL, and ATRIAS respectively.

Alternative, the largest single disturbance that the robot can handle without falling can be measured deterministically [Pratt et al., 2001], [Hobbelen and Wisse, 2007], [McGeer, 1990]. While this simple idea provides a good intuition for stability, we believe the *expected number of steps before failure* metric, described in the next section, is more suitable for controller optimization, and the process in obtaining it also provides valuable information to be exploited in Section 1.2.

1.1.3   Expected Number of Steps Before Failure

This thesis adopts and extends a very intuitive and meaningful stability metric introduced by [Byl, 2008], which has been applied to dynamic walkers. It is also potentially applicable to flat footed humanoids among many other hybrid dynamical systems. [Byl, 2008] presented a methodology to calculate the expected number of steps before failure under stochastic disturbances, e.g., they assumed slopes ahead of the robot generate a Gaussian distribution. This analysis can be interpreted either as estimation of failure rates under disturbances or verification of robustness to these perturbations, depending on the application.

The method, which is explained in detail in Chapter 2, was originally illustrated on two and four dimensional systems [Byl and Tedrake, 2009]. Later [Chen and Byl, 2012] applied this machinery to a six dimensional walker. One of the contributions of this thesis is avoiding the curse of dimensionality to show the applicability of this tool to even higher dimensional systems by illustrating on a robot with a 10D state space. The results indicate a clear promise in applications to even higher degrees-of-freedom humanoids with complex feet walking in 3D.

In addition to calculating expected number of steps before failure, we also extend the framework to calculate other performance measures under stochastic conditions, e.g.,

expected speed or energy consumption per step under stochastic conditions, which are different from the values associated with the limit cycle motion in deterministic environments. We can also compute metrics like expected distance or (continuous) time before failure.

1.2   Autonomous Walking

To measure performance, the framework mentioned in Section 1.1.3 works by learning the dynamics that govern the walking system. This process also provides convenient means for designing high-level behavioral algorithms that utilize state information and optional estimation of environmental parameters. Adopting such a hierarchical control structure does not only increase the stability dramatically, but it also brings autonomy to the robot. Exploiting this capability is one of the main contributions of this thesis.

High-level control proved to be greatly useful experimentally in [Park et al., 2012], where a simple policy was employed: If the last step experienced a step-down of more than 3 cm, "shock absorbing controller" was used. Otherwise the "baseline controller" was activated. On the other hand, our framework provides a systemic way of obtaining more complex and optimal policies in more general scenarios. These behavioral algorithms can also optionally use look-ahead information regarding the terrain when available.

Robots can alternatively utilize information about their environment by kinodynamic motion planning technique proposed in [Donald et al., 1993]. In comparison, our approach falls broadly into the machine learning class instead. Once the high-level control policy is obtained off-line, the only on-line calculation is to use this precomputed look-up table at each step to pick the appropriate low-level controller, which makes the approach compatible with dynamic walking.

1.3   Organization of Thesis

By focusing on a toy example, the next chapter explains the mathematical tools upon which the rest of this thesis builds on. The potential curse of dimensionality problem in using this tool is avoided in Chapter 3, where a powerful meshing method is introduced. Chapter 4 optimizes and benchmarks control action using the stability metric mentioned in Section 1.1.3. In addition, Chapter 5 adopts a hierarchical control structure to increase the performance even more dramatically by optionally using the environmental information for autonomous operation. Conclusions and potential future work are presented in Chapter 6.

Chapter 2

Metastable Walking

Metastable systems can be natural or human-made. They exist in a precarious state of stability, appearing to be locally stable for long periods of time until an external disturbance perturbs the system into a region of state space with a qualitatively different local behavior. Since these systems are guaranteed to escape such locally well-behaved regions with probability one given enough time, they cannot be classified as "stable", but it is also misleading to categorize them simply as "unstable". Physicists have explored this phenomenon in detail and have developed a number of tools for quantifying metastable behaviors [Talkner et al., 1987], [Hanggi et al., 1990], [Muller et al., 1997], [Kampen, 2011]. Metastable processes have been observed in many other branches of science and engineering including familiar systems such as crystalline structures [Larsen and Grier, 1997], flip-flops [Veendrick, 1980], and neuroscience [Fingelkurts and Fingelkurts, 2004].

While focusing on rough terrain walking, this thesis aims to deal with any metastable system for which escape (fail or success) is guaranteed due to the variations in its environment. To elaborate, consider the energy profile in Figure 2.1. Assume we start in state-M and the probability of moving to state-T goes to 1 in time due to the disturbances acting in the system. Let's name state-T as transition state, from which we either go back to

state-M or fall to a stable lower energy state, namely state-S. In this setting, state-M is not stable in the strict sense because disturbances may result in moving to state-S. However, if the transitions from state-M to state-T are rare, it is also misleading to categorize state-M simply as unstable. Since it is "long-living, but destined to eventually end" [Byl, 2008], we classify state-M metastable.
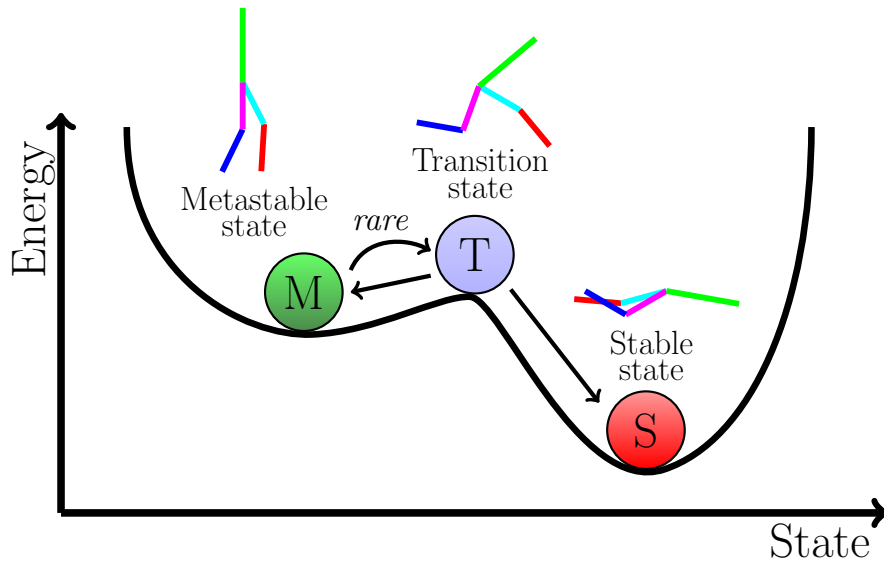
Figure 2.1: Cartoon explaining metastability. Under deterministic conditions, state-M is a locally-stable equilibria in a potential. However, with sufficient noise in the model, the particle is guaranteed to transition to lower energy state, namely state-S. If these guaranteed transitions are extremely rare, states-M is metastable.

Figure is inspired from "Meta-stability" by Georg Wiora licensed under GFDL. See [Benallegue and Laumond, 2013] for an inspiring interpretation of metastable walking.

Figure 2.2 shows how states depicted in Figure 2.1 look in human walking. The key point is to realize that even humans fail in walking from time to time for various reasons. So, walking is the metastable state in bipedal locomotion, and the transition state represents staggering or stumbling. In reality, failure to walk is not absorbing because humans and robots get up after failing. It becomes clear later in the text how, for our purposes, modeling the failure as a stable state does not ignore the ability to start walking again.

(a) Failure in human walking due to slippage

(b) Failure in human walking due to ground being lower than expected

(c) Failure in human walking due to tripping

(d) Failure in human walking due to bad infrastructure

Figure 2.2: Some common failure reasons in human walking. State-M, State-T and State-S correspond to walking, stumbling and failure as depicted in Figure 2.1

Images are take from the following YouTube vidoes: https://www.youtube.com/watch?v=aQ99VULQRI4, https://www.youtube.com/watch?v=oCEZRWZqX9w, and https://www.youtube.com/watch?v=R_B1PkgA3kA.

Before proceeding to mathematical formulation of the framework, we would like to clarify the notation of state. In the representative image of Figure 2.1, walking is a state. However, the state of the robot is actually a numeric value denoted by x which changes while walking. The goal of this chapter is to represent a walking system in the format shown in Figure 2.1.

2.1   Hybrid Model

Let x, γ, and ζ be the internal state, the randomness system experiences, and the control action respectively. To illustrate, for a walking robot, x is the robot's state, γ is the random variable representing factors such as terrain variation and system noise, and ζ is the control action which may be a function of x and γ. Define vector $y := [x; \gamma; \zeta]$ to represent them all. Then, the general hybrid model is represented as

$$
\begin{aligned}
\dot{y} &= f(y) \qquad y \in C, \\
y^+ &= g(y) \qquad y \in D.
\end{aligned}
\tag{2.1}
$$

C and D are flow and jump sets [Goebel et al., 2012]. This setting is compatible with less general cases like continuous and discrete systems with/without a control action or randomness.

2.2   Discretization for State Machine Representation

The first step in discretization precess is choosing a Poincaré-like section, noted by S, such that if the system has not failed yet, it needs to keep passing through this section. For example, the hybrid dynamics of walking systems are punctuated by discrete impacts when a foot comes into contact with the ground. These impacts provide a natural discretization of the robot motion.

15

Abuse the notation by letting x refer to the state when $y \in S$. Then, the next state is a function of the current state $x[n]$, the randomness experienced $\gamma[n]$, and the controller action during that step $\zeta[n]$, that is

$$x[n+1] = \rho(x[n], \gamma[n], \zeta[n]). \tag{2.2}$$

To obtain a (discrete) Markov decision process model, finite sets for control action, randomness, and state are needed. The first one is rather easy, finitely many low-level controllers are designed which form the controller set Z. The second (randomness), is straightforward to handle when the number of noise sources is low. For instance, $\{0, \frac{1}{k-1}, \frac{2}{k-1}, ..., 1\}$ is a uniform discretization of $[0, 1]$ with k elements. In this thesis we study 1 dimensional disturbances and the density of the randomness set Γ is a function of parameter d_γ given by

$$\Gamma = \left\{ \gamma \ : \ \frac{\gamma}{d_\gamma} \in \mathbb{Z}, \ \gamma_l \leq \gamma \leq \gamma_r \right\}, \tag{2.3}$$

where γ_l and γ_r determine the range of randomness set, which needs to be wide enough to model the terrain of interest. Having a wider than needed randomness range has no disadvantage, but too narrow range causes inaccuracy. In particular, the robot should *not* be able to walk at the boundaries of the randomness set, otherwise we extend the range.

Just like range, density of the randomness set can be chosen depending on the controllers' performance, and on the robot. Also, the randomness set does not have to be evenly spaced in general, it may be denser around values of particular interest. As we increase the density of the randomness set, we are able to capture the dynamics more accurately at the expense of higher computational costs.

If the internal state x is also low-dimensional, the entire state space can potentially be uniformly meshed to obtain state set X. However, as dimensionality increases this method becomes intractable. This potential curse of dimensionality is handled in Chapter 3.

Once control, randomness and state spaces are represented by finite sets, we simulate $\rho(x, \gamma, \zeta)$ for each $x \in X$, $\gamma \in \Gamma$, and $\zeta \in Z$ to obtain the state-transition map, which gives deterministic information about the dynamics. In case the resulting point is not in the state set, i.e., $\rho(x, \gamma, \zeta) \notin X$, we need to approximate the dynamics. The most elementary approach is 0'th order approximation given by

$$x[n+1] \approx c(\rho(x[n], \gamma[n], \zeta[n]), X), \tag{2.4}$$

where $c(\bar{x}, X)$ is the closest point $x \in X$ to $\bar{x}$ for the employed distance metric. Then the deterministic state transition matrix can be written as

$$T_{ij}^d(\gamma, \zeta) = \begin{cases} 1, & \text{if } x_j = c(\rho(x_i, \gamma, \zeta), X) \\ 0, & \text{otherwise.} \end{cases} \tag{2.5}$$

The nearest-neighbor approximation in (2.4) appears to work well in practice. More sophisticated approximations result in transition matrices not just having one or zero elements, but also fractional values in between [Abbel, 2012]. This increases memory and computational costs while, to our experience, not providing much increase in accuracy.

The deterministic state transition matrix corresponds to a state machine similar to Figure 2.3. In this figure, $x[n] \in \{x_M, x_S, x_T\}$, $\gamma[n] \in \{\gamma_1, \gamma_2\}$ and $\zeta[n] \in \{\zeta_1, \zeta_2\}$, which means there are three states possible, two actions (low-level control) available, and two random outcomes. Note that given what the randomness is, the transition is deterministic in this graph.

To derive the Markov chain model we then need to determine a policy π, which is the high-level control picking the right low-level control action at each step. Chapter 5 is devoted to deriving optimal and robust policies. Let the decided policy for the state
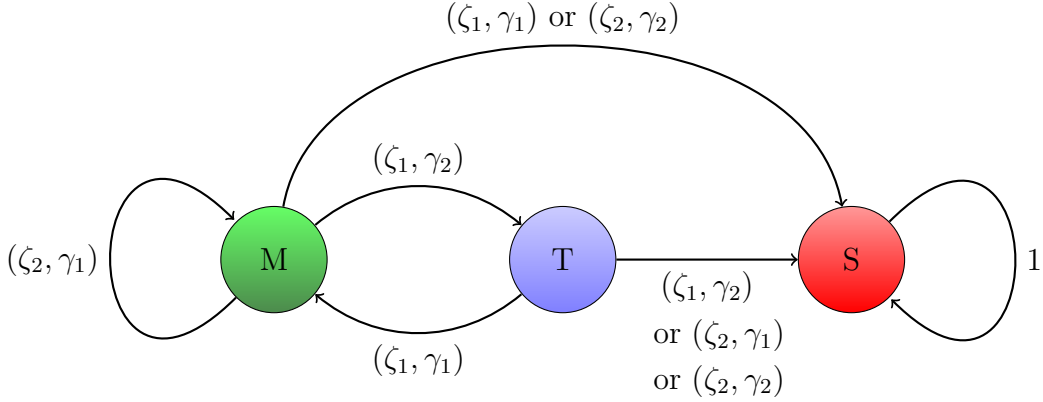
Figure 2.3: A state machine with three states (x_M, x_T, x_S), two available actions (ζ_1, ζ_2), and two possible randomness (γ_1, γ_2). Many hybrid systems can be treated as a finite-state machine. In case the dynamics are not discrete already, they need to be discretized with a Poincaré section. In addition, if the randomness and state sets are continuous, they should be meshed for finite randomness and state sets.

machine in Figure 2.3 be

$$
\pi(x[n], \gamma[n]) = \begin{cases}
\zeta_2 \text{ if } x[n] = x_M \text{ and } \gamma[n] = \gamma_1, \\[1em]
\zeta_1 \text{ if } x[n] = x_M \text{ and } \gamma[n] = \gamma_2, \\[1em]
\zeta_1 \text{ if } x[n] = x_T \text{ and } \gamma[n] = \gamma_1, \\[1em]
\zeta_2 \text{ if } x[n] = x_T \text{ and } \gamma[n] = \gamma_2.
\end{cases}
\tag{2.6}
$$

Notice that policy does not determine a control action for state x_S since nothing can be done differently at an absorbing state. When $\zeta[n] = \pi(x[n], \gamma[n])$ is used, (2.2) becomes

$$
x[n+1] = \rho(x[n], \gamma[n], \pi(x[n], \gamma[n])),
\tag{2.7}
$$

which is a function of the state and randomness only. The result is illustrated in Figure 2.4.

Although in this chapter we assume perfect state information and randomness estimation are available to the high-level control, in Chapter 5 we study the more general case.
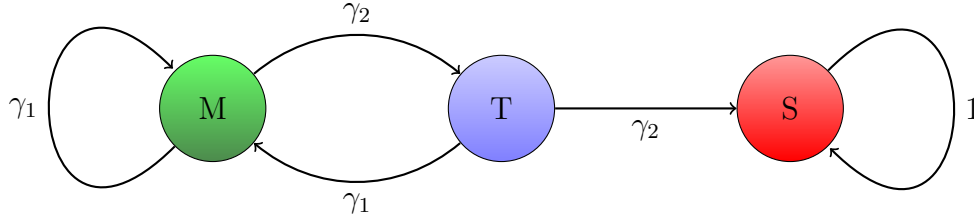
Figure 2.4: A state machine with three states (x_M, x_T, x_S) and two possible randomness (γ_1, γ_2), which can be obtained from the finite-state machine of Figure 2.3 after applying policy π defined in (2.6). Alternatively, this figure is what the model would look like if there was a single low-level controller too. The policy in that case would be using the only available controller.

2.3   Stochasticity for Markov Decision Process

Given deterministic state transition matrix, the last step before obtaining a Markov chain is to assume a distribution for randomness formulated as

$$P_\Gamma(\gamma) := Pr(\gamma[n] = \gamma). \tag{2.8}$$

Then the stochastic state-transition matrix

$$T_{ij} := Pr(x[n+1] = x_j \mid x[n] = x_i), \tag{2.9}$$

which represents the corresponding Markov Chain, can be calculated by

$$T = \sum_{\gamma \in \Gamma} P_\Gamma(\gamma) \, T^d(\gamma, \zeta). \tag{2.10}$$

In case $\zeta[n] = \pi(x[n], \gamma[n])$, the stochastic matrix becomes

$$T = \sum_{\gamma \in \Gamma} P_\Gamma(\gamma) \, T^d(\gamma, \pi(x, \gamma)). \tag{2.11}$$

This last equation will be updated when we consider noise in state information and randomness estimation in Chapter 5 .

For Figure 2.4, let $\Pr(\gamma_1) = p$, which means the probability of $\gamma[n]$ being γ_1 is p. The result is the Markov chain shown in Figure 2.5. More complicated systems end up being surprisingly similar to this figure. Note that in case $p=1$, only state-M observed if this was the initial state. So, the walking would be stable. However, no matter how close to 1, if p does not equal to 1, the probability of moving to the stable state goes to 1 in time.
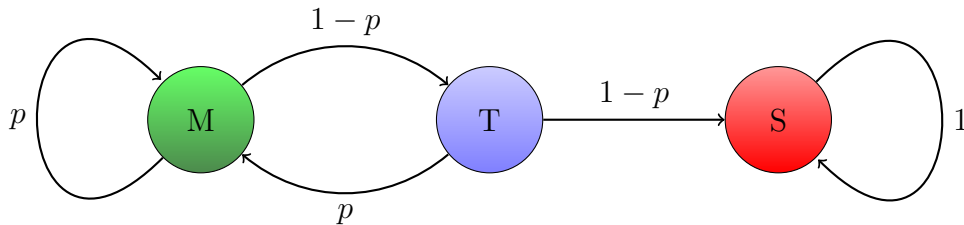
Figure 2.5: Markov chain obtained from the finite-state machine in Figure 2.4 by assuming $\Pr(\gamma_1) = p$. Note that State-S is absorbing. Moreover, State-M is metastable if p is close to but smaller than 1. This graph also looks like the following coin-flip game. Consider tossing an unfair coin, for which the probability of having tails is p. When the number of flips before two heads in a row is of interest, three states are possible: (S) Heads-heads, (M) Tails in the last flip (including 'not-flipped yet'), (T) Tails-Heads (including 'flipped once and it was heads').

At this point, it is important to note that when a policy is not yet determined, but stochasticity is added, instead of a Markov chain, we obtain a Markov decision process. The reason why we preferred to add stochasticity at the last step to obtain a Markov chain becomes clear in Chapter 4. In summary, this order clarifies the following property. By discretization, say the true dynamics of the system are approximated as a finite-state machine that is similar to Figure 2.4. Then, we can easily and very quickly compute the expected number of steps before failure for different stochasticities in the disturbance. Also, we wanted to emphasize that the discretization process is deterministic.

2.4   Eigenanalysis for Stability Metric Development

Treating the system as a Markov chain lends itself to a straightforward reliability measurement. Let λ_1 and λ_2 be the largest two eigenvalues of the transition matrix associated with the Markov chain in consideration. Since all failure modes are modeled to be an absorbing state, $\lambda_1 = 1$ and the corresponding state distribution, which is called stationary distribution, has all the probability mass at the failure state.

As explained in detail in Appendix A, after taking several steps without failing, the robot's state distribution typically almost converges to *metastable distribution*. Then, as shown in Figure 2.6, the robot is able to take the next step successfully with probability λ_2 and it fails otherwise. This allows very easy quantification of stability by

$$\text{Expected Number of Steps Before Failure} = \frac{1}{1 - \lambda_2}. \tag{2.12}$$

In this calculation we also count the step leading to failure. So, the expected number of steps before failure is larger than or equal to 1.
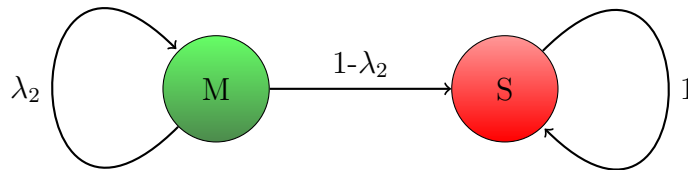
Figure 2.6: Metastable dynamics. As explained in detail in Appendix A, after taking several steps without failing, the robot's state distribution typically almost converges to *metastable distribution*, which is represented by the green ball on the left. The robot is able to take the next step successfully with probability λ_2, which implies mapping back to the metastable distribution. Otherwise the robot transitions to failure state, which is represented by the red ball on the right. Then, the stability of walking on rough terrain can be easily quantified by (2.12).

2.5   Toy Example: Rimless Wheel

As a toy example, in this section we study the system shown in Figure 2.7, where the slope may change at each step[1]. After the introduction of passive dynamic walking in [McGeer, 1990] over two decades ago, the rimless wheel has become very popular in locomotion research because this uncomplicated walker keeps many of the essential properties of dynamic walking robots [Bhounsule, 2014]. For simplicity, we focus on forward walking only and assume the mass is lumped to the center of the robot and equals m=1 kg, length of each leg is given by l=1 m, number of legs is 8, gravitational acceleration is κ=9.81 m/s^2, and legs never slip, i.e., the friction is always enough. For a more general and detailed approach to the rimless wheel compared to this section refer to [Saglam et al., 2014].
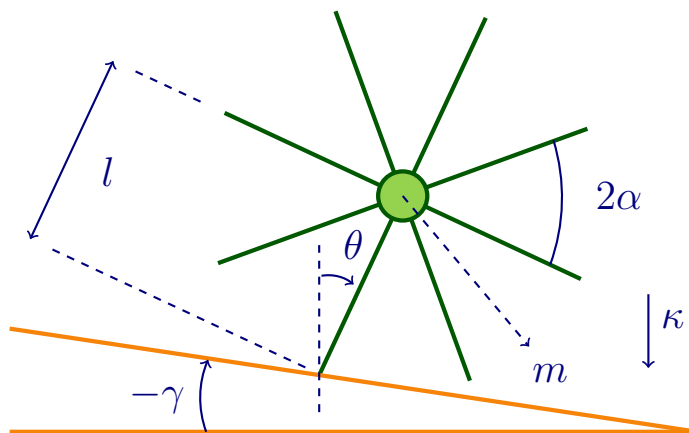
Figure 2.7: The rimless wheel as depicted in [Byl and Tedrake, 2009]. We define forward direction to be to the right (i.e., clockwise). The state for this walker is two dimensional, consisting of the angle θ and velocity $\omega = \dot{\theta}$. Negative γ values correspond to downhill.

The single support phase is when only one leg is in contact with the ground. This phase has continuous pendulum dynamics given by $\ddot{\theta} = \kappa \sin(\theta)$. The leg in contact with the ground is referred to as the stance leg. On the other hand, double support phase is

---

[1]See Appendix C for terrain modeling.

when two legs contact the ground, which is well described as an instantaneous impact event. The jump map is obtained using conservation of momentum as $\omega^+ = \cos(2\alpha)\omega$, where $\omega = \dot{\theta}$ is the angular velocity [McGeer, 1990]. Thus, the rimless wheel is a hybrid dynamical system which can be expressed in the form of (2.1). Walking is single and double support phases following one another. A step occurs between two consecutive impacts and includes one of these impacts. In this thesis, we arbitrarily define it to include the first of the two impacts. Failure refers to not being able to take another step.

For the rimless wheel example, let's take a Poincaré section at $\theta = 0$. Then, given $\omega[n] > 0$ and $\omega[n+1] \geq 0$, the next velocity of the robot (when $\theta = 0$) is given by

$$\omega[n+1] = \sqrt{\cos^2(2\alpha)(\omega^2[n] + 2\kappa(1 - \cos(\gamma[n] + \alpha))) - 2\kappa(1 - \cos(\gamma[n] - \alpha))}, \quad (2.13)$$

which can be easily verified using the conservation of energy during the flows and conservation of angular momentum at the impacts. If the argument of the square root in the equation above turns out to be negative, then the robot did not actually intersect the Poincaré section again which means failure. Note that (2.13) is a special case of (2.2) with no control action.

As mentioned, the method of this chapter requires finite and discrete slope and state sets. For the state set we use

$$\Omega = \left\{ \omega \; : \; \frac{\omega}{0.01} \in \mathbb{Z}, \; 0 < w \leq 2.5 \right\}, \quad (2.14)$$

And the slope set is

$$\Gamma = \left\{ \gamma \; : \; \frac{\gamma}{0.1} \in \mathbb{Z}, \; 0 \leq \gamma \leq 16 \right\}, \quad (2.15)$$

Both sets can be made denser for higher accuracy or coarser for faster computation. Because of low dimensionality, computation time is very small (less than a second). Also, the accuracy gained while calculating the expected number of steps with denser sets is negligible.

After determining the slope and state sets, we calculate $\omega[n+1]$ for each $\omega \in \Omega$ and $\gamma \in \Gamma$ using (2.13) and form the deterministic state transition matrix as explained in Section 2.2. To obtain Markov chain representation we assume the slopes are normally distributed with mean μ_γ and standard deviation σ_γ, i.e., $\gamma[n] \sim \mathcal{N}(\mu_\gamma, \sigma_\gamma^2)$. The Markov chain obtained and, as a result, the expected number of steps before failure calculated using (2.12) depends on the distribution of slopes as depicted in Figure 2.8.
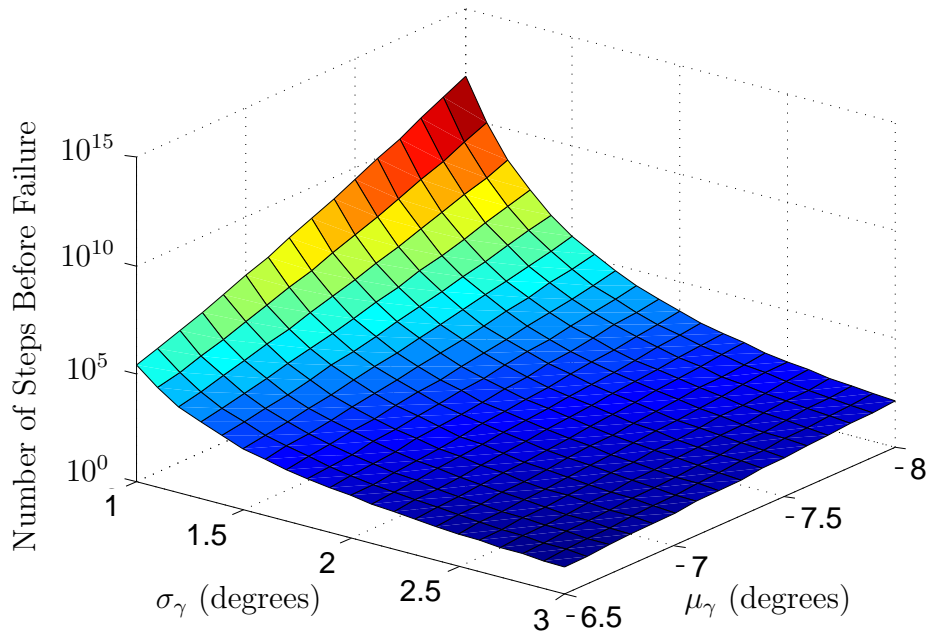
Figure 2.8: Expected number of steps before failure for rimless wheel as a function of stochasticity. Slopes ahead of the robot are assumed to be normally distributed with mean μ_γ and standard deviation σ_γ. When μ_γ is small enough for constant rolling, smaller σ_γ implies higher expected number of steps before failure.

Chapter 3

Discretization of High-Dimensional States

In applying the tool of Chapter 2, one of the steps was meshing the state space to represent it with finitely many elements, e.g., $\{0, \frac{1}{k-1}, \frac{2}{k-1}, ..., 1\}$ is a uniform discretization of $[0, 1]$ with k elements. However, uniformly meshing the entire state space becomes intractable for high dimensional systems. Thus, as mentioned in Section 2.2, there is potentially a curse of dimensionality for high degrees-of-freedom robots. However, if the intrinsic dimension of the reachable state space is low, meshing can still be achieved for systems with high-dimensional states as explained in this chapter.

3.1   Avoiding the Curse of Dimensionality

The critical observation toward avoiding the curse of dimensionality is the fact that only the *reachable state space under the given control law* needs to be meshed instead of the entire state space. Let us illustrate with the simple biped model shown in Figure 3.1. This walker has two massless legs and one actuator which controls the inter-leg angle.

Assuming second order dynamics, the state space is 4 dimensional for this walker, consisting of 2 angles and 2 velocities. To begin with, assume that immediately after each impact, the controller ensures $q = 2\alpha$ and $\dot{q} = 0$. In this case, this walker is identical to the rimless wheel we studied in Section 2.5 where 2α corresponds to the fixed inter-leg angle. Note that although this simple biped has a 4D state, the reachable state space under the mentioned control law is only 2 dimensional.
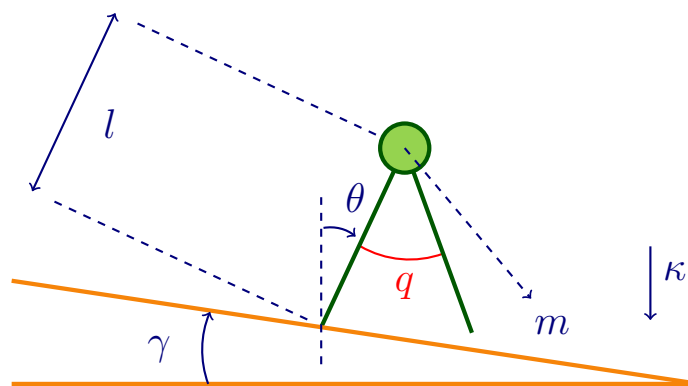
Figure 3.1: Illustration of a very simple biped model. The legs are massless and the only actuator controls the inter-leg angle q. Assuming that immediately after each impact the controller ensures $q = 2\alpha$ and $\dot{q} = 0$, then this biped behaves like the rimless wheel in Figure 2.7.

In reality, the controller may not be able to reach its references before every impact. To maximize the allowed time for converge, we take the Poincaré section just before impacts instead of $\theta = 0$ as in Section 2.5. However, even after this choice, the controller may not be able to perfectly convergence in some cases, so the reachable state space typically turns out to be a *quasi*-2D manifold. Note that the rimless wheel has 1 degree-of-freedom (DOF) but no actuators, and the massless legged biped has 2 DOF and 1 actuator. So, both these walkers are underactuated by 1 DOF. Similarly, the 5-link biped modeled in Appendix B is also underactuated by 1 DOF, because it has 5 links and 4 actuators. As a result, the reachable state space under a given control law turns out to be a quasi-2D manifold for the 5-link biped also [Saglam and Byl, 2013a].

We note that the reachable state space being a lower dimensional manifold is not an intrinsic requirement for our meshing technique, which is presented next. This section is rather an explanation why the following method does not explode and instead stays tractable when applied to high DOF robots.

3.2   Explored Meshing

Determining the state set is difficult because we are studying high dimensional systems, e.g., the 5-link walker has a 10 dimensional state (i.e., positions and velocities). So, it is *not* feasible to uniformly and densely cover a hypercube that includes the reachable state space. However, meshing the reachable state space can be achieved by starting from an initial state set X_i with very small number of points (one "good" state, such as the fixed point under mean disturbance, is enough) and deterministically expanding by iteratively simulating.

Our algorithm works as follows. We initially start by setting $\overline{X} = \{x \in X_i \ : \ x \neq x_1\}^1$, which corresponds to all non-failure states that are not simulated yet. Then we start the following iteration: As long as there is a state $x \in \overline{X}$, simulate to find all possible $\rho(x, \gamma, \zeta)$ and remove x from $\overline{X}$. For the points newly found, check their distance to the other states in X. If the distance is larger than some threshold d_{thr}, i.e., the point is far enough from all existing mesh points, then add that point to X and $\overline{X}$. We call the mesh obtained by this method *explored-mesh* and present the pseudocode in Algorithm 1.

Using the right distance metric is crucial in ensuring that X has a small number of states while accurately covering the reachable state space. Standardized (normalized) Euclidean distance turned out to be extremely useful as it dynamically adjusts the weights for each dimension according to its standard deviation at any mesh iteration. The distance

---

[1]As explained in Appendix A, without loss of generality x_1 represents all the failures no matter how robot failed.

Algorithm 1 Explored meshing algorithm

Input: Initial set of states X_i, Randomness set Γ, Controller set Z, and threshold distance d_{thr}

Output: Final set of states X, and state-transition map

1: $\overline{X} \leftarrow X_i$ (except x_1)
2: $X \leftarrow X_i$
3: **while** $\overline{X}$ is non-empty **do**
4:      $\overline{X}_2 \leftarrow \overline{X}$
5:      empty $\overline{X}$
6:      **for** each state $\overline{x} \in \overline{X}_2$ **do**
7:          **for** each slope $\gamma \in \Gamma$ **do**
8:              **for** each controller $\zeta \in Z$ **do**
9:                  Simulate a single step to get the final state $\overline{x}$ when initial state is x, slope ahead is γ, and controller ζ is used (Calculate $\overline{x} = \rho(x, \gamma, \zeta)$). Store this information in the state-transition map
10:                  **if** robot did not fall ($\overline{x} \neq x_1$) and $d(\overline{x}, X) > d_{thr}$ **then**
11:                      add $\overline{x}$ to $\overline{X}$
12:                      add $\overline{x}$ to X
13:                  **end if**
14:              **end for**
15:          **end for**
16:      **end for**
17: **end while**

---

of a vector $\bar{x}$ from X is calculated as

$$d(\bar{x}, X) := \min_{x \in X} \left\{ \sum_i \left(\frac{\bar{x}_i - x_i}{r_i} \right)^2 \right\}, \tag{3.1}$$

where r_i is the standard deviation of i'th dimension of all existing points in set X. In addition, the closest point in X to x is given by

$$c(\bar{x}, X) := \operatorname*{argmin}_{x \in X} \left\{ \sum_i \left(\frac{\bar{x}_i - x_i}{r_i} \right)^2 \right\}. \tag{3.2}$$

Our algorithm allows us to increase the accuracy of the final mesh at the expense of producing a higher number of states (larger X) by decreasing threshold distance d_{thr} for states and discretization length d_γ used for randomness set in (2.3).

While meshing the whole 10D state space for the 5-link walker we study in this thesis is infeasible, this method is able to avoid the curse of dimensionality because the reachable state space is actually a quasi-2D manifold as explained in the first section.

For the rimless wheel, Figure 3.2 shows the explored mesh obtained using $d_{thr} = 0.025$ and $d_\gamma = 0.5$. Points in this figure correspond to possible states just before impacts. The probability of being at each state is shown with color. Convex hulls of states that cover the 0.9, 0.99, 0.999, and 0.9999 of the state probability distribution are also drawn.

In Section 2.5 the state mesh was only 1 dimensional because we took a Poincaré section at $\theta = 0$. As we focus on the states just before the impact in this chapter, the reachable state space is rather 2 dimensional. However, we obtain similar results using both methods. In particular, let's consider uniformly distributed slope changes with mean $\mu_\gamma = 7°$ and standard deviation $\sigma_\gamma = 1°$ for the rimless wheel. Under these circumstances, we calculated the expected number of steps to be 1.79×10^7 and 2.1×10^7 in the previous chapter and using explored mesh of Figure 3.2 respectively.
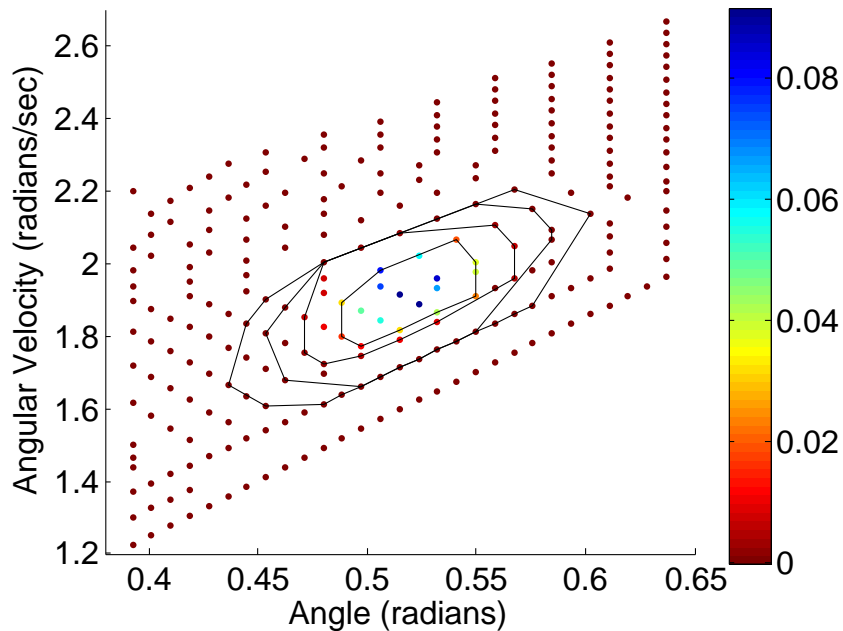
Figure 3.2: Explored meshing method applied on the rimless wheel in Figure 2.7. Threshold distance $d_{thr} = 0.025$ and slope set discretization length $d_\gamma = 0.5$ were used to obtain a mesh with 252 states shown in this figure. Colored bar depicts the probability of being at a state at the end of a step while walking. Convex hulls cover 0.9, 0.99, 0.999, and 0.9999 of the state probability distribution. The expected number of steps is calculated to be 2.1×10^7 using this mesh.

3.2.1   Two Tricks

Two important tricks to make the explored meshing algorithm run faster are as follows. First, the randomness set allows a natural cluster analysis. The distance comparison for a new point can be made only with the points that are associated with the same slope. This might result in more points in the final mesh, but it speeds up the meshing and later calculations significantly. Secondly, fix a controller ζ and a state x. Then we can simulate $\rho(x, \min(\Gamma), \zeta)$ and then potentially extract $\rho(x, \gamma, \zeta)$ for all $\gamma \in \Gamma$. To illustrate, in order for the robot to experience an impact at -30 degree, it has to pass through all the possible impact points with higher degrees, and we can extract all impact cases from a single simulation.

Chapter 4

Low-Level Control Action

Performance of highly-dynamic walkers is often quantified by speed or energy consumption under deterministic conditions [Hobbelen and Wisse, 2007]. However, legged robots need "good" disturbance rejection to operate reliably in real-world environments, and achieving this goal requires quantifying robustness. Out of the small number of metrics proposed for measuring robustness of dynamic walkers, the L2 gain calculation in [Dai and Tedrake, 2013] was successfully extended and implemented on a real robot in [Griffin and Grizzle, 2015]. Alternatively, largest terrain disturbance was maximized in [Pratt et al., 2001] and trajectories were optimized to replicate human-walking data in [Ames, 2012]. Instead, this thesis adopts the metric explained in Chapter 2, which is used to optimize and benchmark control action in this chapter. We argue that this approach provides better performance on rough terrain and it is more powerful for benchmarking purposes. Mostly, we study the particular control strategy formulated in Appendix D as a case demonstration. However, two other control schemes are also optimized for benchmarking purposes. The first one is the now-familiar hybrid zero dynamics approach [Westervelt et al., 2003] and the other is a method using piece-wise reference trajectories with a sliding mode control [Saglam and Byl, 2013b].

For optimization, we employ the "fminsearch" in MATLAB®, which uses the derivative-free method proposed by [Lagarias et al., 1998] to find the unconstrained minimum. In case we impose constraints, we use the extended version provided by [Oldenhuis, 2009] instead.

4.1 Optimization of a Given Controller

As mentioned, control action is often designed to minimize energy consumption or maximize speed. For the first one, Cost of Transport (COT) gives the non-dimensionalized energy expenditure per unit weight and unit distance [Tucker, 1975]. It is defined as the total mechanical energy spent, divided by weight times distance, i.e.,

$$\text{COT} = \frac{W}{mgd},\tag{4.1}$$

where m is the mass, g is the gravitational constant, and d is the distance traveled. In this paper we use the conservative definition of "energy spent" by regarding negative work is also done by the robot, i.e.

$$W = |W_{positive}| + |W_{negative}| = W_{positive} - W_{negative}\tag{4.2}$$

so that both acceleration and breaking require power, but there is no regenerative breaking. Compared to energy efficiency, measuring speed under deterministic conditions is even more straightforward.

To evaluate the stability obtained by optimizing for these metrics, we consider normally changing the slopes in front of the robot as in Figure C.1a. We fix the long-term mean slope to be $\mu_\gamma = 0$ and vary the standard deviation σ_γ to calculate resulting expected number of steps before failure depicted in Figure 4.1. The results reveal that optimizing for these metrics results in sensitivity to perturbations, thus performing poorly on rough terrain as expected.

On the other hand, now we have a mathematical formulation for the expected number of steps before failure, we can finally optimize for it using

$$\underset{\substack{\text{controller}\\\text{parameters}}}{\text{maximize}} \{\text{the number of steps}\} = \underset{\substack{\text{controller}\\\text{parameters}}}{\text{maximize}} \left\{ \frac{1}{1 - \lambda_2} \right\}, \tag{4.3}$$

where the right hand side comes from (2.12). To calculate this number we assume slopes are normally distributed with zero mean and standard deviation $\sigma_\gamma = 5°$. Noting that y-axis is in logarithmic scale, Figure 4.1 demonstrates that optimizing for stability using (4.3) provides extreme improvements in rough terrain walking performance. For $\sigma_\gamma = 5°$, while the other two are expected to take less than 1.5 steps, controller optimized for stability is expected to take around 10 thousand steps. The difference is even more dramatic for smaller but nonzero terrain roughness.
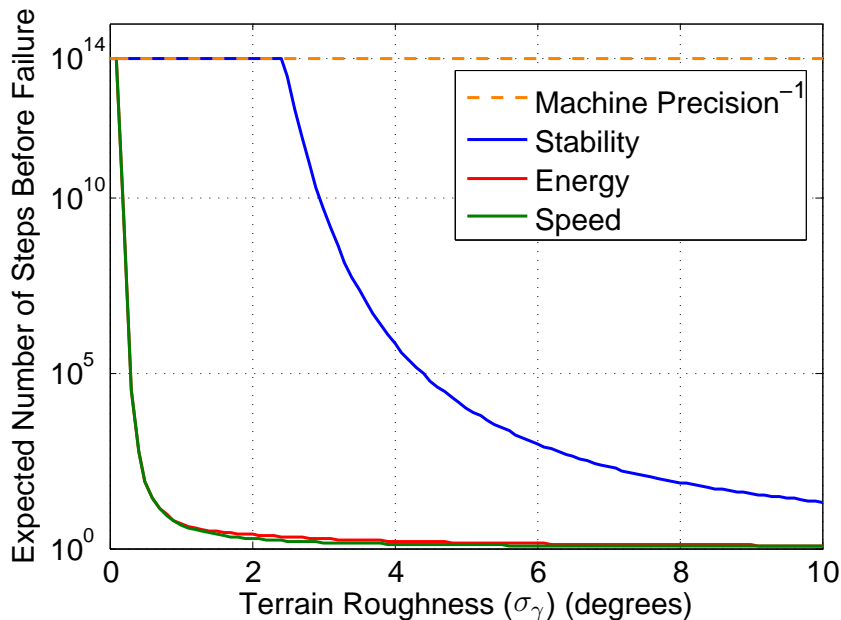
Figure 4.1: Optimization of low-level control action using different metrics. Noting that the y-axis is in logarithmic scale, figure reveals that optimizing for stability using (4.3) provides extreme improvements in rough terrain walking performance. This figure shows expected number of steps before falling calculated using (2.12) versus σ_γ. Slopes ahead of the robot are assumed to be normally distributed with $\mu_\gamma = 0$. Numerical limit at 10^{14} is due to machine precision, and it corresponds to a million tours around the world for a human-sized robot with half a meter step length.

33

Note that the number of points in the final mesh, and the accuracy obtained from (2.12) with this mesh, are inversely related to parameters d_{thr} and d_γ, where d_{thr} is the threshold distance in Algorithm 1 and d_γ is the discretization length in (2.3). We claim that, as $d_\gamma \to 0$ and $d_{thr} \to 0$, the mesh captures the true, hybrid dynamic system dynamics, and as a result, the expected number of steps before failure for the controllers, converges. To test the accuracy of our calculations, we evaluate the performance of the top controller in Figure 4.1 using $(d_{thr}, d_\gamma) \in \{(2, 2.5), (1, 1), (0.5, 0.5)\}$. The fine mesh, which is obtained using $(d_{thr}, d_\gamma) = (0.5, 0.5)$, has 77,329 states, and the coarse mesh, which is a result of using $(d_{thr}, d_\gamma) = (2, 2.5)$, consists of only 372 states. Figure 4.2 demonstrates the convergence of performance quantification with indistinguishable curves.
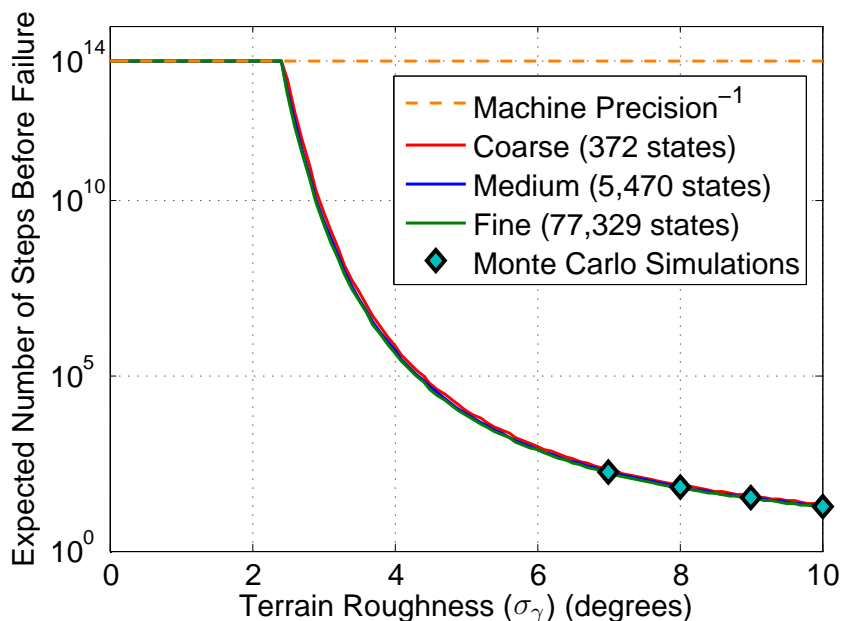
Figure 4.2: Verification of performance quantification. The fine mesh is obtained using $(d_{thr}, d_\gamma) = (0.5, 0.5)$, and the coarse mesh is a result of using $(d_{thr}, d_\gamma) = (2, 2.5)$. Closely matching curves and data points indicate our performance quantification is accurate. This figure shows expected number of steps before falling calculated using (2.12) versus σ_γ. Slopes ahead of the robot are assumed to be normally distributed with $\mu_\gamma = 0$. Numerical limit at 10^{14} is due to machine precision, and it corresponds to a million tours around the world for a human-sized robot with half a meter step length.

34

For further verification of our results, we also carry Monte Carlo simulations for $\sigma \in \{7°, 8°, 9°, 10°\}$. For each case we simulate 10^4 times until failure. The average number of steps are also provided in Figure 4.2. Closely matching results validates our approach once again. At this point we would like to clarify some clear advantages of our methodology over Monte Carlo simulations. While obtaining a *single point* in Figure 4.2 required "$10^4 \times$average number of steps" simulations for Monte Carlo method, all of the curve associated with the coarse mesh was obtained by 372 simulations only! So, with far fewer simulations we were able to create a whole curve instead of getting a single data point. This is because once the system is discretized, addition of stochasticity and calculation of λ_2 are fast operations. Note that Monte Carlo simulations become quickly intractable as the number of steps increases, whereas the numerical limit in our method is very high and can be enlarged by increasing the machine precision when necessary. Furthermore, calculating the curve is just one of the outcomes in our methodology. This complete tool, for example, also provides invaluable information for high-level control design as we will see in the next chapter.

[Benallegue and Laumond, 2013] presents a method based on Monte Carlo simulations to compute the expected number of steps before failure when it is very high. The method relies on the property that for a fixed controller dynamic walkers return very close to their limit-cycle over and over again as they keep walking. In a future work, this method will be used to verify the curves in Figure 4.2 also for low σ_γ values.

4.2   Benchmarking Controller Schemes

In addition to optimization capabilities, benchmarking is a powerful use of our mathematical tool, which we already employed to present Figure 4.1 and 4.2. In this section, we look at how different controller schemes optimized for stability compare. The first one

is the now-familiar hybrid zero dynamics (HZD) approach [Westervelt et al., 2003]. The second is a method using piece-wise reference trajectories with a sliding mode control (PC-SMC) [Saglam and Byl, 2013b]. Finally, extended hybrid zero dynamics (EHZD) controller is the scheme adopted throughout this paper, which is explained in detail in Appendix D. We optimize all three controller schemes using (4.3). Figure 4.3 demonstrates EHZD is a more capable controller algorithm compared to the other two. As a future work, we are extremely interested in adding more controller schemes to this figure, such as time-varying controllers, ZMP-based algorithms (when applicable), and central pattern generators [Brown, 1914], [Kuo, 2002]. We also encourage other researchers to use our methods to demonstrate capabilities of the controllers they designed or optimized.
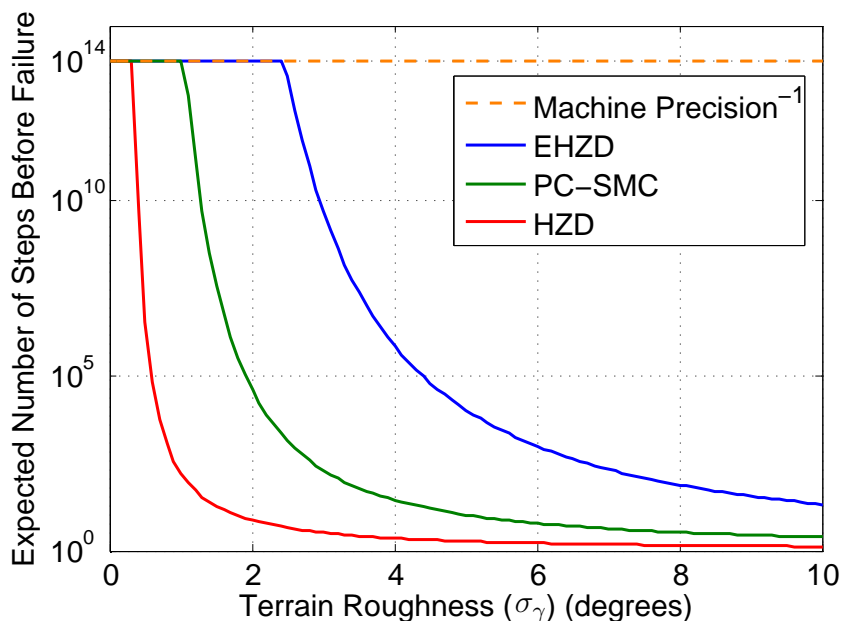
Figure 4.3: Benchmarking various controller schemes. Extended hybrid zero dynamics controller turns out to be more capable in rough terrain walking. However, the goal of this figure is to show benchmarking capability of our mathematical tool. This figure shows expected number of steps before falling calculated using (2.12) versus σ_γ. Slopes ahead of the robot are assumed to be normally distributed with $\mu_\gamma = 0$. Numerical limit at 10^{14} is due to machine precision, and it corresponds to a million tours around the world for a human-sized robot with half a meter step length.

36

4.3   Comparison to Other Work

We finally compare our results with the state-of-the-art. Like this thesis, [Dai and Tedrake, 2013] adopts the RABBIT robot model provided in Appendix B. However, instead of using normal distributions as we have done so far, they uniformly distribute the slopes ahead of the robot. Then, they optimize a time-varying control structure for the L2 gain to minimize deviations due to ground variations. To test their resulting controller, they assume the slopes ahead of the robot is normally distributed between -2 and +2 degrees and simulate 40 times until failure. The robot takes 20.325 steps on average as depicted in Figure 4.4, where our controller greatly outperforms in terms of stability. Note that to obtain the curve for our controller, we did not discretize the
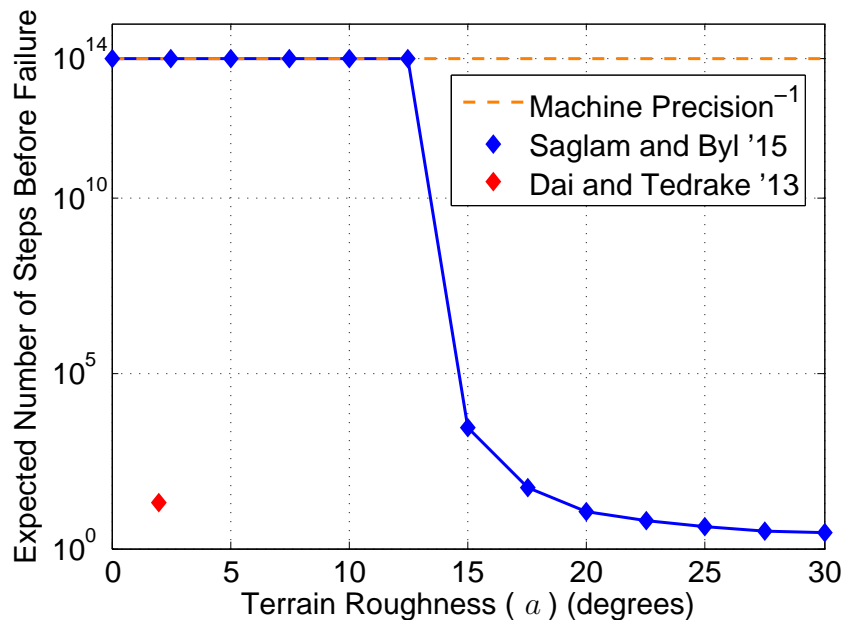
Figure 4.4: First comparison with the state-of-the-art. Our controller outperforms the [Dai and Tedrake, 2013] and we were able to present our results with more data points using fewer simulations. This figure shows expected number of steps before falling calculated using (2.12) versus a. Slopes ahead of the robot are assumed to be <u>uniformly</u> distributed between $\pm a$ degrees. Numerical limit at 10^{14} is due to machine precision, and it corresponds to a million tours around the world for a human-sized robot with half a meter step length.

dynamics again. We simply used our discretization from the previous section and added a different form of stochasticity. The computation took only several seconds.

We would like to explain why there is a sudden fall in expected number of steps around $\sigma_\gamma = 14°$ in Figure 4.4 unlike the previous 2 figures, where we used normal distributions. Say the slopes are normally distributed between $\pm a$ degrees. Imagine a robot which can walk in a stable manner when $a = 14$ degrees. Assume the robot falls in two steps beyond this limit. Now, if we look at $a = 12.5°$, then we should expect to hit the numerical limit in Figure 4.4. However, if $a = 15°$, then there is around $1/15^2 \approx 0.00444$ chance the robot will fail after the following two steps, which corresponds to only 225 steps on average. On the other hand, when we employ normal distributions we consider a very wide range of slopes possible with finite probabilities for all, which might be extremely small at the tails. But this gives us smooth transitions and allows calculating any σ_γ value, whereas calculations for a values outside slope set are not always trustable. That's why Figure 4.4 only uses the data points shown to form the curve, while the previous two figures uses a much denser standard deviation set, so each data point are not shown to avoid clutter.

In addition to Figure 4.4, we also followed the method in [Dai and Tedrake, 2013] and simulated 40 times until failure independent from the discretization process. Instead of limiting slopes between -2 and +2 degrees, where our robot seems unlikely to fall, we used -17.5 and +17.5 degrees to take 77.525 steps on average as listed in Table 4.1.

Table 4.1: First comparison with the state-of-the-art. Slopes ahead of the robot are changing uniformly. Simulations are carried 40 times until failure.

	Terrain Roughness	Average Number of Steps
Hongkai Dai and Russ Tedrake, 2013	$[-2°, 2°]$	20.325
Cenk Oguz Saglam and Katie Byl, 2015	$[-17.5°, 17.5°]$	77.525

In another state-of-the-art work, [Griffin and Grizzle, 2015] again uses uniform distribution, but this time instead of slopes ahead of the robot, step heights change as illustrated in Figure C.1b. They simulate 50 times until failure, but they limit each iteration to 10^4 steps to reduce computational cost. They report that their controller was able finish 4 of the 50 trials when step heights are uniformly distributed between ± 4 cm. On average the robot takes 4,616 as shown in Figure 4.5. In comparison, although our
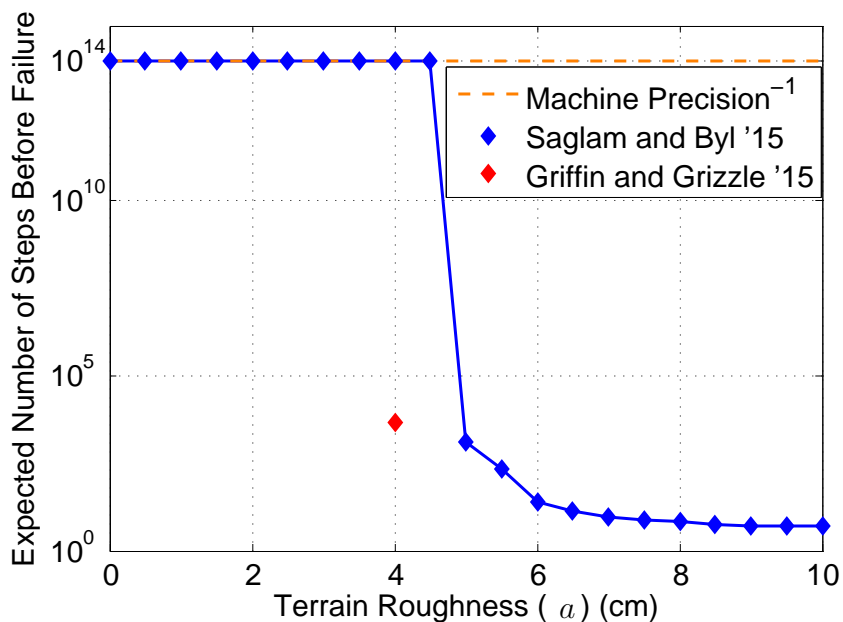
Figure 4.5: Second comparison with the state-of-the-art. Our controller also outperforms the [Griffin and Grizzle, 2015] and we were able to present our results with more data points using fewer simulations. This figure shows expected number of steps before falling calculated using (2.12) versus a. Step heights ahead of the robot are assumed to be *uniformly* distributed between $\pm a$. Numerical limit at 10^{14} is due to machine precision, and it corresponds to a million tours around the world for a human-sized robot with half a meter step length.

controller was optimized for a *normally distributed sloped terrain*, it outperforms on a *uniformly distributed step terrain* as shown in Figure 4.5. Independently from this figure, we also simulated 50 times when step heights are uniformly distributed between ± 4 cm, and our robot was able to complete all trials as listed in Table 4.2. We should also note that while we and [Dai and Tedrake, 2013] are working on RABBIT shown in Figure 1.4c,

[Griffin and Grizzle, 2015] use a model for ATRIAS pictured in Figure 1.4e.

Table 4.2: Second comparison with the state-of-the-art. Step heights ahead of the robot are changing uniformly. Simulations are carried 50 times until failure or reaching the limit at 10^4 steps.

	Terrain Roughness	Finished Trials
Brent Griffin and Jessy Grizzle, 2015	$[-4, 4]$ cm	4/50
Cenk Oguz Saglam and Katie Byl, 2015	$[-4, 4]$ cm	50/50

4.4   Incorporating Secondary Metrics

Finally, once stability is quantified, it is straightforward to incorporate other metrics. To illustrate, the controller parameters obtained using (4.3) turns out to produce a relatively slow walking motion as shown in Table 4.3. However, if we allow extra room for the optimization to also consider other metrics, we obtain walking gaits that are faster and more energy efficient as the table demonstrates. The cost function given by $2\times\text{COT}-\text{speed}$ was empirically chosen and the potential trade-off can be easily adjusted depending on the application.

The fact that optimal controller depends on what the objective (or cost) function is motivates adopting the hierarchical control structure of the next chapter. In particular, section 5.3 studies the advantages of switching between the two controllers listed in Table 4.3.

Table 4.3: Incorporating secondary metrics on low-level control design. The second column gives the expected number of steps before failure when slopes are normally distributed with zero mean and standard deviation equals 5 degrees.

	Expected Number of Steps	Speed	COT
$\underset{\substack{\text{controller} \\ \text{parameters}}}{\text{maximize}} \left\{ \dfrac{1}{1 - \lambda_2} \right\}$	$\approx 10^4$	0.462	0.212
$\underset{\substack{\text{controller} \\ \text{parameters}}}{\text{minimize}} \left\{ 2 \times \text{COT} - \text{speed} \right\}$ subject to $\dfrac{1}{1 - \lambda_2} \geq 10^2$	$\approx 10^2$	0.7	0.185

Chapter 5

High-Level Behavioral Policy

What is very intuitive but has lacked sufficient attention in the robotics community is that humans do not walk the same way on every ground type. They modify their walk depending on various conditions, such as whether the surface is pavement or clay, whether the ground is triangular (slopes), or rectangular (stairs), whether it's uphill or downhill, and whether there are obstacles on the way, just to name some terrain features. It is not possible or necessary to design a specific controller for each specific case. However, if we have multiple controllers (potentially designed with different general cases in mind) available, the robot may increase stability by appropriately switching among controllers. While switching using only internal (proprioceptive) state information (blind-walking) is advantageous [Park et al., 2012], [Saglam and Byl, 2014c], a dramatic improvement is obtained with use of upcoming terrain information [Saglam and Byl, 2013b]. Instead, work to date has typically focused either on remaining robust when blind to upcoming terrain [Raibert et al., 2008], [Park et al., 2013] or on achieving particular footstep lengths [Hodgins and Raibert, 1991], without more generally addressing the issue of planning on partly-known terrain. In this chapter we propose a systematic way to solve this problem.

Figure 5.1 displays the hierarchical control structure adopted in this thesis, which features a high-level control picking one of the low-level controllers at each step. As expressed in Chapter 2 when there are multiple low-level controllers available to the robot, discretization yields a Markov decision process, which is solved to obtain a Markov chain and to quantify reliability. In the general form, policies (high-level controllers) are functions of the state estimation and noisy terrain information. Simpler policies are special cases in this setting. The goal is to obtain robust, near-optimal control policies for low-level controllers using dynamic programming tools [Bellman, 1957], [Saglam and Byl, 2014c].

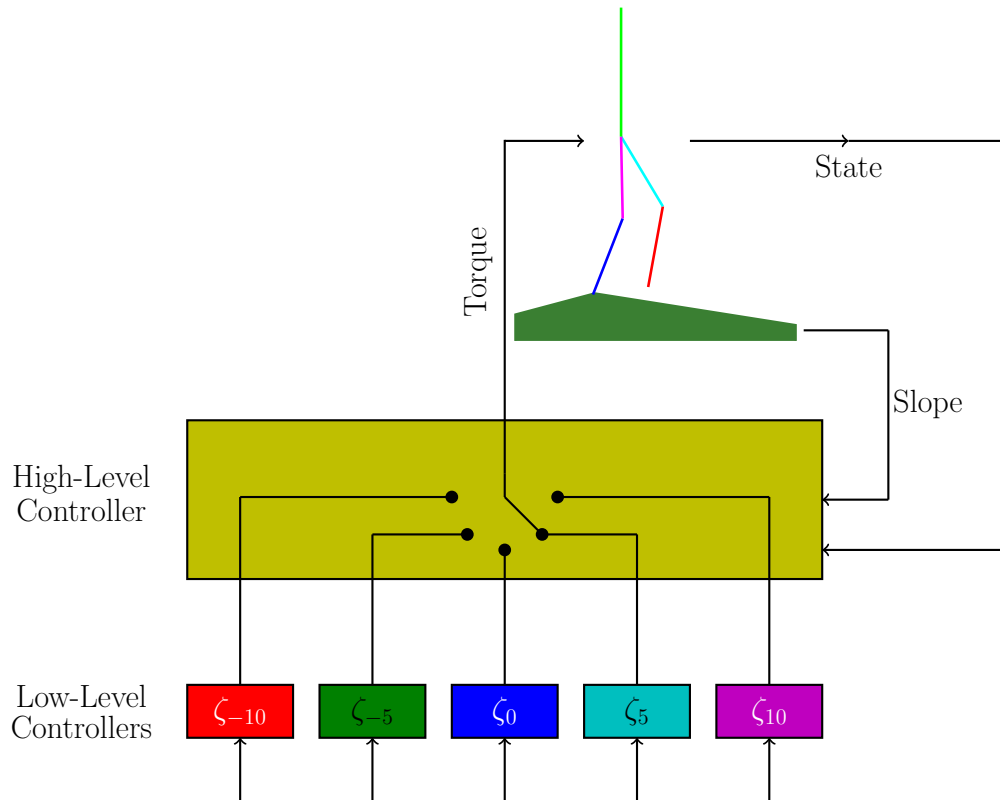Figure 5.1: Hierarchical control structure. At each step, the high-level controller picks a low-level controller to use given state estimation and optional noisy terrain information. In this figure there are five low-level controllers available. ζ_i denotes the low-level control optimized for a normally distributed terrain with mean $\mu_\gamma = i$ degrees and standard deviation $\sigma_\gamma = 5°$ using Chapter 4's method.

Let ζ_i denote the low-level control optimized for a normally distributed terrain with mean $\mu_\gamma = i$ degrees and standard deviation $\sigma_\gamma = 5°$ using Chapter 4's method. To begin with, we use the controller set given by $Z = \{\zeta_{-10},\ \zeta_{-5},\ \zeta_0,\ \zeta_5,\ \zeta_{10}\}$ and discretize the dynamics using Algorithm 1 with $d_{thr} = 1$ and $d_\gamma = 1°$. The resulting mesh has 59,804 states.

5.1   Optimal Policies

In this section we look at the benefits of using environment and state information to switch between low-level controllers. Initially we assume none of these are available to the robot, so the policy is to use one of the fixed controllers. Then we investigate the improvements gained by using slope <u>or</u> state information only. In these cases the robot is said to do visual or blind walking respectively. On the other hand, in general a policy is a function of both slope and state estimation, so the policy is given by

$$\zeta[n] = \pi(x[n], \gamma[n]), \tag{5.1}$$

as used in Chapter 2. We refer to this choice as sighted walking.

5.1.1   Fixed Controllers

The simplest policy is to use just one controller, i.e.,

$$\zeta[n] = \zeta_i \tag{5.2}$$

for fixed i. In this case T is calculated as in (2.10) for a given μ_γ and σ_γ. We then derive the expected number of steps before failure using (2.12). To evaluate the performance of the individual controllers in Z depending on the long-term mean slope, we fix σ_γ to be 5 degrees. The results are demonstrated in Figure 5.2, where the x-axis is μ_γ, and the y-axis shows the expected number of steps before failure.

We note that the optimal choice for using one of the fixed controllers in Z depends on the long term mean slope. If the mean slope is close to 0 degrees, the fixed controller policy needs to be using ζ_0 for optimality.
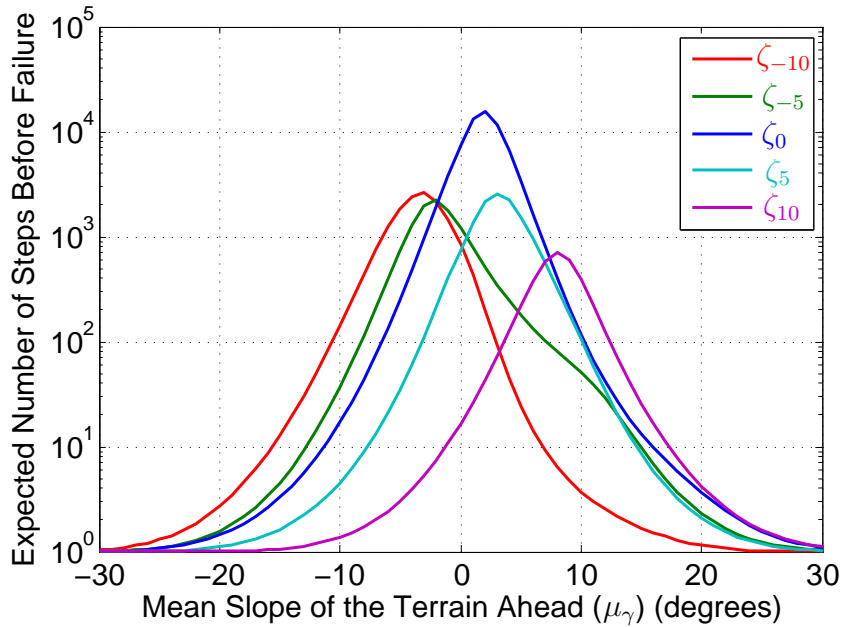
Figure 5.2: Performance of individual low-level controllers. Let ζ_i denote the low-level control optimized for a normally distributed terrain with mean $\mu_\gamma = i$ degrees and standard deviation $\sigma_\gamma = 5°$ using Chapter 4's method. The controllers shown in this picture are ζ_{-10}, ζ_{-5}, ζ_0, ζ_5, and ζ_{10} from left to right. The expected numbers of steps before falling are calculated using (2.12) versus μ_γ. Slopes ahead of the robot are assumed to be normally distributed with $\sigma_\gamma = 5$ deg.

5.1.2   Visual Walking

After seeing that the performance of the individual controllers depends significantly on the mean slope ahead, we consider policies using only one-step lookahead ($\gamma[n]$) information, which are in the form of

$$\zeta[n] = \pi(\gamma[n]). \tag{5.3}$$

A trivial idea is to look at the slope ahead and using the controller which was optimized for the nearest slope. In other words, $\pi(\gamma[n]) = \zeta_i$ and $i = c(\gamma, \{-10, -5, 0, 5, 10\})$, where function c is as defined in (3.2). To illustrate, we use controller ζ_0 when $-2.5° \leq \gamma \leq 2.5°$. We present the performance of this *trivial policy* in Figure 5.3. It is rather surprising to see how bad this intuitive policy turns out to be. To improve the performance, we used genetic algorithm to obtain the *visual policy* given by

$$\pi(\gamma[n]) = \begin{cases} \zeta_{-10}, & \gamma \leq -28.5° \\ \zeta_{-5}, & -28.5° < \gamma \leq -17.5° \\ \zeta_0, & -17.5° < \gamma \leq 24.5° \\ \zeta_5, & 24.5° < \gamma \leq 29.5° \\ \zeta_{10}, & 29.5° < \gamma, \end{cases} \tag{5.4}$$

which performs better when $\mu_\gamma = 0$.

Although the improvements gained by using slope estimation seem to be small in this specific case, we later discover in the following sections that single-step lookahead to terrain is very useful when used together with state information.
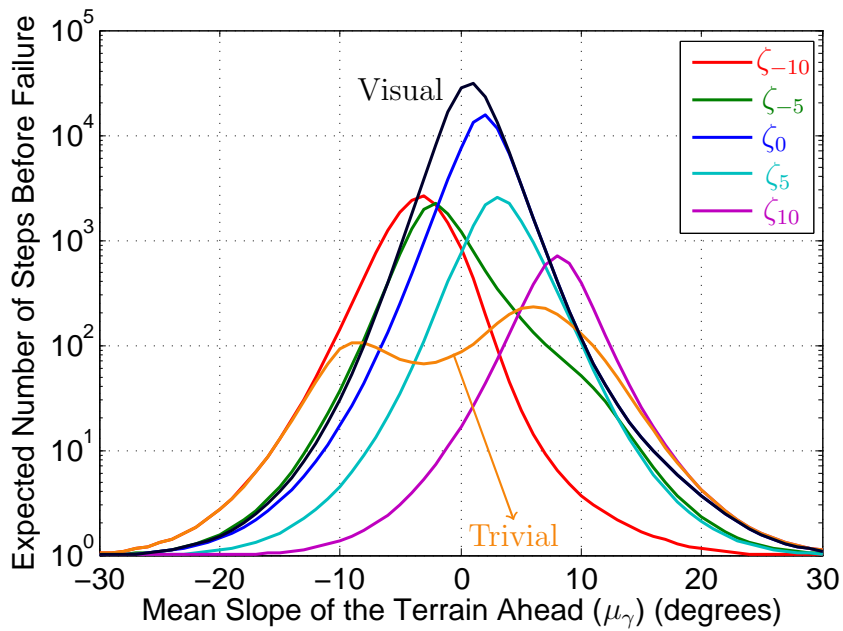
Figure 5.3: Performance of a two visual policies. The trivial high-level controller uses $\pi(\gamma[n]) = \zeta_i$ and $i = c(\gamma, \{-10, -5, 0, 5, 10\})$, where function c is as defined in (3.2). To illustrate, it picks ζ_0 when $-2.5° \leq \gamma \leq 2.5°$. Visual policy is defined in (5.4). See Figure 5.2 to distinguish five fixed controllers shown in this picture. The expected numbers of steps before falling are calculated using (2.12) versus μ_γ. Slopes ahead of the robot are assumed to be normally distributed with $\sigma_\gamma = 5$ deg.

5.1.3   Blind (to the terrain) Walking

In practice the robot knows its state and it is typical to assume policy to be a function of the state in Markov Decision Processes, i.e.,

$$\zeta[n] = \pi(x[n]). \tag{5.5}$$

The optimal policy is commonly solved using value iteration [Bellman, 1957], which works by recursively calculating

$$V(i) := \max_{\zeta} \left\{ \sum_{j} P_{ij}(\zeta) \, (R(j) + \alpha \, V(j)) \right\}, \tag{5.6}$$

where V is the value, $P_{ij}(\zeta)$ is the probability of transitioning from x_i to x_j when ζ is used, $R(j)$ is the reward for transitioning to x_j, and $\alpha \in [0,1]$ is the discount factor, which is chosen to be 0.9. This equation is iterated until convergence to get the optimal policy.

Remember that the failure state is x_1. The value of the failure state is initially set to zero, i.e.,

$$V(1) = 0, \tag{5.7}$$

and it always stays as zero, because the reward for taking a successful step is one, while falling is zero, i.e.,

$$R(j) = \begin{cases} 0, & j = 1, \\ 1, & \text{otherwise.} \end{cases} \tag{5.8}$$

Note that the reward function we use does not depend on the controller, slope ahead, or current state. Use of more sophisticated reward functions (e.g., considering energy, speed, step width) is a topic of Section 5.3 and [Saglam and Byl, 2014b]. However, our initial focus is only on stability in this chapter. Substituting (5.7) and (5.8) into (5.6) yields

$$V(i) := \max_{\zeta} \left\{ \sum_{j \neq 1} P_{ij}(\zeta) \, (1 + \alpha \, V(j)) \right\}. \tag{5.9}$$

The probability of 'transitioning from x_i to x_j when ζ is used' is

$$P_{ij}(\zeta) = \sum_{\gamma \in \Gamma} P_\Gamma(\gamma) \, T_{ij}^d(\gamma, \zeta). \tag{5.10}$$

So we can alternatively write the value iteration algorithm as

$$V(i) := \max_\zeta \left\{ \sum_{\gamma \in \Gamma} P_\Gamma(\gamma) \sum_{j \neq 1} T_{ij}^d(\gamma, \zeta) \, (1 + \alpha \, V(j)) \right\}. \tag{5.11}$$

Optimization results for $\mu_\gamma = 0$ and $\sigma_\gamma = 5$ deg are shown in Figure 5.4. In the light of this figure, we conclude that even blindly switching between the controllers may provide dramatic improvements on the overall performance. However, it is also important to note that we have not studied discretization errors yet. So, Figure 5.4 may be overselling the improvements obtained by blind-to-the-terrain switching.

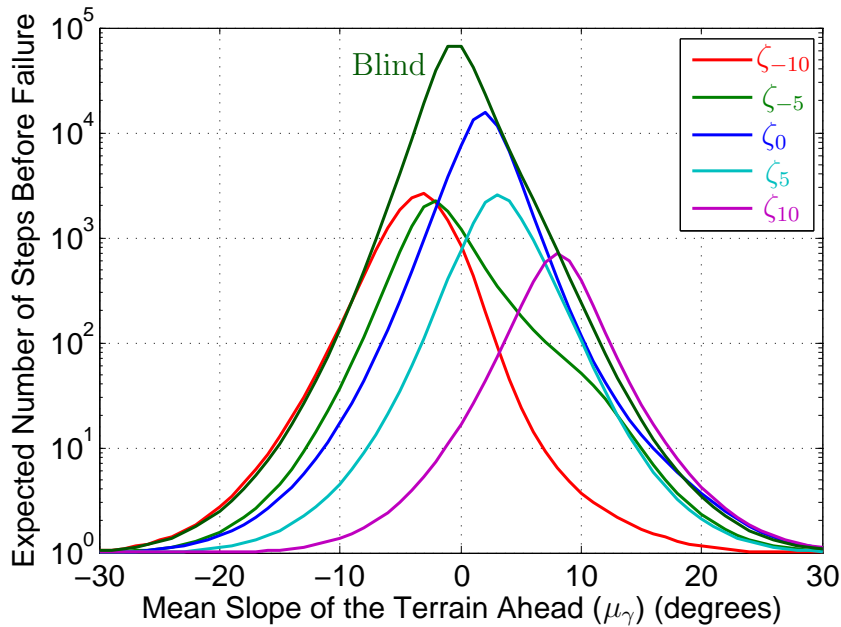Figure 5.4: Blind walking. The high-level controller knows the state but it is blind to the environment. Value iteration is used to get the optimal policy. See Figure 5.2 to distinguish five fixed controllers shown in this picture. The expected numbers of steps before falling are calculated using (2.12) versus μ_γ. Slopes ahead of the robot are assumed to be normally distributed with $\sigma_\gamma = 5$ deg.

5.1.4   Sighted Walking

In sighted walking the high-level controller uses both the state information and one-step lookahead to terrain, i.e., the policy is given by (5.1). To use the one-step lookahead in deriving policy, we modify the value iteration in (5.11) as

$$V(i) := \sum_{\gamma \in \Gamma} \max_{\zeta} \left\{ P_{\Gamma}(\gamma) \sum_{j \neq 1} T_{ij}^d(\gamma, \zeta) \left(1 + \alpha \, V(j)\right) \right\}. \tag{5.12}$$

So, maximization operation is carried for each slope in Γ.

Instead of modifying the value iteration algorithm, we could define a new 11D state, including the slope in addition to the 10D state of the robot. However, (5.12) makes the analysis of the following parts easier, reduces computational cost, and requires less memory. Note that $P_{\Gamma}(\gamma)$ gives the probability of 'the slope ahead being γ' and $T_{ij}^d(\gamma, \zeta)$ is the probability of 'transitioning from x_i to x_j when ζ is used and the slope is γ'.

We optimize for $\mu_\gamma = 0$ and $\sigma_\gamma = 5$ degrees to get the performance shown in Figure 5.5. Noting the logarithmic y-axis, it is clear that sighted walking is significantly better than visual and blind walking, as one would intuitively expect. The ability to quantify this intuition is a driving goal of our work.

Although the optimal high-level control in Figure 5.5 is obtained by optimizing for $\mu_\gamma = 0$ and $\sigma_\gamma = 5$ degrees, the figure demonstrates that it also performs well for $\mu_\gamma \neq 0$. In the following sections we observe that the same argument follows for $\sigma_\gamma \neq 5$ degrees.

The dramatic improvement gained by using one-step terrain lookahead along with state information motivates measuring how much a two-, three- and infinite-step lookahead increases the stability, which is a topic of future work.
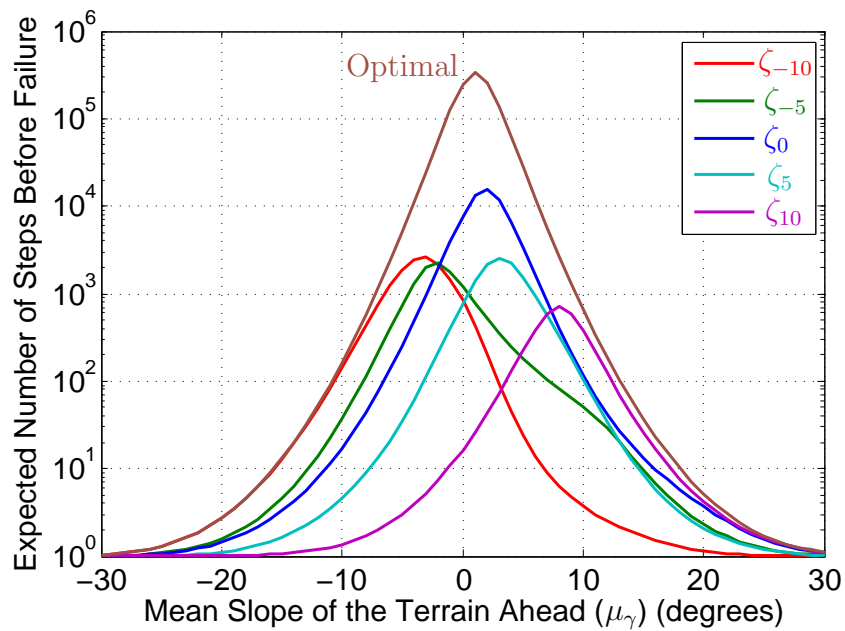
Figure 5.5: Sighted walking. The high-level controller uses both the state information and one-step lookahead to terrain. See Figure 5.2 to distinguish five fixed controllers shown in this picture. The expected numbers of steps before falling are calculated using (2.12) versus μ_γ. Slopes ahead of the robot are assumed to be normally distributed with $\sigma_\gamma = 5$ deg.

5.2   Robustness of Switching

Although Figure 5.5 is impressive, for this methodology to be applicable to real-life problems, policies must be robust to uncertainties. In particular, considering the noise in the inputs of high-level controller is crucial. So, in this section we study and improve robustness of sighted walking to terrain estimation and state information. The results motivate experimenting the methods and controllers of this thesis on a real robot.

5.2.1   Noisy Terrain Estimation

We start our robustness study by considering the addition of noise to slope information. The slope ahead is still defined by variable γ, but let's say the controller thinks it is (closest to) $\tilde{\gamma} \in \Gamma$, due to the noise $l \in \Gamma$. The relationship is given by

$$\tilde{\gamma} = max(min(\Gamma), min(max(\Gamma), \gamma + l)). \tag{5.13}$$

Note that this equation simply says $\tilde{\gamma} = \gamma + l$ except at boundaries of the slope set. $P_L(l)$ is defined by

$$P_L(l) := Pr(l[n] = l), \tag{5.14}$$

and normally distributed with zero mean and standard deviation σ_l, i.e.,

$$l[n] \sim \mathcal{N}(0, \sigma_l^2). \tag{5.15}$$

In the presence of noise, the policy is a function of $\tilde{\gamma}$, not γ. Thus, we have

$$\zeta[n] = \pi(x[n], \tilde{\gamma}[n]). \tag{5.16}$$

Then the stochastic state-transition matrix in (2.10) becomes

$$T = \sum_{\gamma \in \Gamma} \sum_{l \in \Gamma} P_\Gamma(\gamma) \; P_L(l) \; T^d(\gamma, \pi(x, \tilde{\gamma})). \tag{5.17}$$

To account for noise in the slope information while optimizing, we first rewrite the modified value iteration algorithm as

$$V(i) := \sum_{\tilde{\gamma} \in \Gamma} \max_{\zeta} \left\{ \sum_{\gamma \in \Gamma} P_{\Gamma}(\gamma) P(\gamma, \tilde{\gamma}) \sum_{j \neq 1} T_{ij}^d(\gamma, \zeta) \left(1 + \alpha \, V(j)\right) \right\}, \qquad (5.18)$$

where $P(\gamma, \tilde{\gamma})$ is the probability of 'actual slope being γ when robot thinks it is $\tilde{\gamma}$'. This probability is given by

$$P(\gamma, \tilde{\gamma}) = \sum_{l \in \tilde{\Gamma}} P_L(l), \qquad (5.19)$$

where $\tilde{\Gamma} = \{l \in \Gamma \mid \tilde{\gamma} = max(min(\Gamma), min(max(\Gamma), \gamma + l))\}$.

Note that in this setting the sighted policy of Figure 5.5 is a special case that is obtained assuming no sensor noise, i.e., $\sigma_l = 0°$. Figure 5.6 shows what happens to this policy in the presence of noise. As σ_l increases we rapidly start performing worse than the
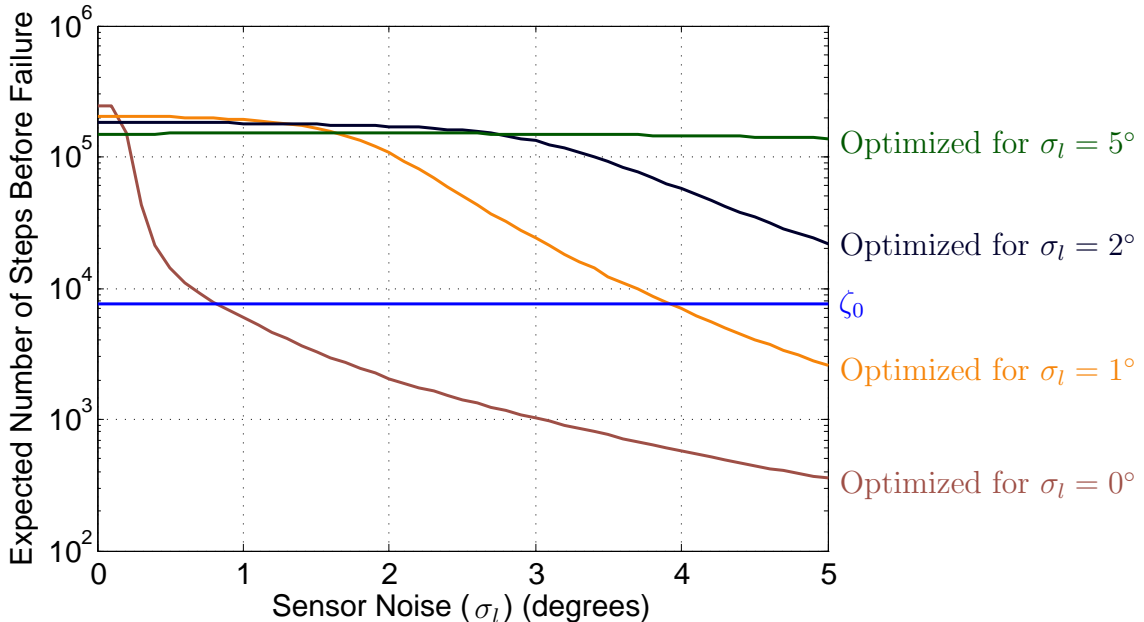
Figure 5.6: Noisy terrain estimation. Sighted policy from Figure 5.5 performs poorly with $\sigma_l \neq 0$. Considering noise while optimizing provides robustness while keeping almost all the optimality. The expected numbers of steps before falling are calculated using (2.12) versus σ_l. Slopes ahead of the robot are assumed to be normally distributed with $\mu_\gamma = 0$ and $\sigma_\gamma = 5$ deg. Fixed controller ζ_0 is drawn for reference.

fixed controller ζ_0. The figure also demonstrates that considering noise while optimizing provides robustness to terrain estimation while mostly keeping the optimality. Although optimizing for very high σ_l values seem tempting in this graph, it is important to note that we have not considered discretization errors yet and as we assume higher σ_l while optimizing, the high-level controller tends to rely more on the state information.

Next, we assume the sensor noise is given by $\sigma_l = 1°$. In practice this number can be easily and conservatively calculated. The performance of the high-level control optimized for $\sigma_l = 2°$ versus mean slope is presented in Figure 5.7.
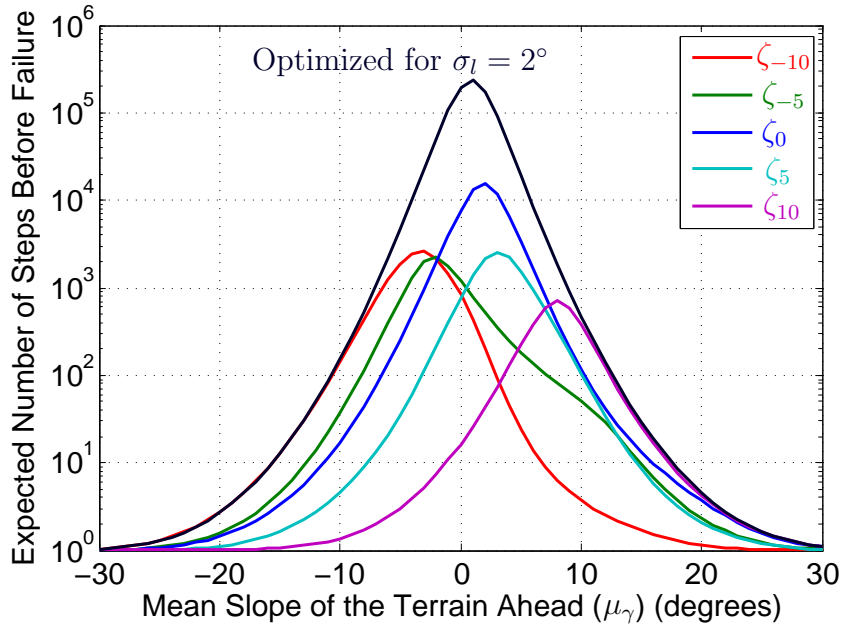
Figure 5.7: A policy which is robust to sensor noise. Comparing with Figure 5.5, we conclude that we obtain nearly optimal performance even under the presence of sensor noise in terrain estimation. See Figure 5.2 to distinguish five fixed controllers shown in this picture. The expected numbers of steps before falling are calculated using (2.12) versus μ_γ. Slopes ahead of the robot are assumed to be normally distributed with $\sigma_\gamma = 5$ deg. Slope estimation experiences a normal noise with zero mean and standard deviation $\sigma_l = 1°$.

5.2.2   Discretization Errors

Up until now, we optimized policies and evaluated resulting performance using the same ($d_{thr} = 1$) mesh. In this section, we keep optimizing on the coarse ($d_{thr} = 1$) mesh, but we estimate performance using a denser, more refined ($d_{thr} = 0.7$) mesh, intended to better approximate the true system dynamics. The high-resolution mesh, which has 199,358 states, is used to tune the real performance of high-level control and ensure its robustness to discretization errors. First, we need to explain how the coarse-mesh policy can be applied when the noisy slope ahead estimation $\tilde{\gamma}[n]$ may not be in the slope set, and/or state $x[n]$ may not be in the mesh. In these cases, we apply the most basic idea formulated by

$$\zeta[n] = \pi(c(x[n], X), c(\tilde{\gamma}[n], \Gamma)), \tag{5.20}$$

where function c is as defined in (3.2). In its general form, let us denote the dense mesh by X_d, which is obtained from a slope set Γ_d. Using this mesh, we can approximate how (5.20) would behave in practice by

$$\zeta[n] = \pi(c(x_d[n], X), c(\tilde{\gamma}_d[n], \Gamma)), \tag{5.21}$$

where $x_d \in X_d$ and $\tilde{\gamma}_d \in \Gamma_d$. The definition and calculation of T remain the same, but this time X_d and Γ_d is used in obtaining it. Figure 5.8 shows that the policy from Figure 5.7 performs poorly when evaluated on the dense mesh. We must once again refine our algorithm, this time to improve robustness to meshing discretization.

In our approach to fix this issue, we consider the following: While the actual state is x_i, the robot may think it is x_k. To make this clear, we rewrite the value iteration algorithm as

$$V(k) := \sum_{\tilde{\gamma} \in \Gamma} \max_{\zeta} \left\{ \sum_{\gamma \in \Gamma} P_\Gamma(\gamma) P(\gamma, \tilde{\gamma}) \sum_i P(i, k) \sum_{j \neq 1} T_{ij}^d(\gamma, \zeta) \left(1 + \alpha \, V(j)\right) \right\}, \tag{5.22}$$

where $P(i, k)$ is the probability of 'actual state being x_i when robot thinks it is x_k'.
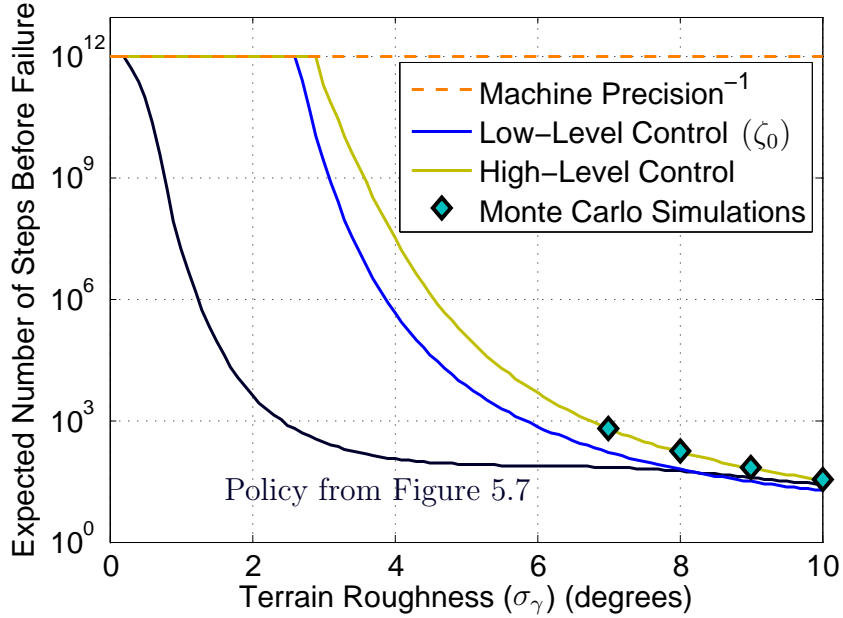
Figure 5.8: Performance evaluation on the dense mesh. The policy from Figure 5.7 performs poorly. However, discretization errors can be handled to obtain the robust policy shown in this graph. Compare to Figure 4.2, where the stability of low-level controller was verified with Monte Carlo simulations. The expected numbers of steps before falling are calculated using (2.12) versus σ_γ. Slopes ahead of the robot are assumed to be normally distributed with $\mu_\gamma = 0$. Sensor noise is given by $\sigma_l = 1°$. Fixed controller ζ_0 is drawn for reference. Numerical limit at 10^{12} is due to machine precision, and it corresponds to a 10 thousand tours around the world for a human-sized robot with half a meter step length.

Finding the best calculation for $P(i, k)$ is an open question. However, it is intuitive that for a given state k (the robot thinks the state is x_k), $P(i, k)$ should be smaller for i for which $d(x_i, x_k)$ is larger. Among many other methods, inverse distance weighting as in [Shepard, 1968] did not provide desirable performance. In [Saglam and Byl, 2014c], we illustrate that an exponential distribution works well. In this thesis, to show the applicability of various distributions, we use power distribution given by

$$P(i, k) = \frac{\lambda^c}{\sum_c \lambda^c} \approx \lambda^c (1 - \lambda), \tag{5.23}$$

where x_i is the cth closest state to x_k and $0 \leq \lambda \leq 1$ is the distribution parameter[1].

---

[1] Assume $0^0 = 1$ when using (5.23).

Note that this is just a power distribution scaled to have $\sum_k P(i,k) = 1$. As we increase λ, robustness increases but performance drops. $\lambda = 0$ would mean $P(i,i) = 1$ and $P(i,k) = 0$ for $i \neq k$, i.e., what we had before this section. $\lambda = 1$ would try to consider all points in the mesh[2] with equal probability. Then the high-level controller would not make use of state information, so it would be a visual policy.

To derive final high-level control policy, we again use $\sigma_l = 2°$ for optimization and quickly tune $\lambda = 0.5$ by trial and error using the dense mesh. The resulting performance is demonstrated in Figure 5.8. The stability of the high-level controller turns out to be more than 2 orders of magnitude depending on the terrain roughness. To illustrate, for $\mu_\gamma = 0°$ and $\sigma_\gamma = 3.5°$, while the most stable low-level controller (ζ_0) is expected to take 1.4×10^7 steps, the high-level controller increases this number to 1.8×10^9. As in Figure 4.2, we conduct Monte Carlo simulations for higher σ_γ values as shown in Figure 5.8 and Table 5.1. The close matches verify the performance of the final high-level control policy. To compare it with all the low-level controllers available to the robot, we present Figure 5.9, where we assumed $\mu_\gamma = 0$ and $\sigma_\gamma = 5$ deg.

Table 5.1: Monte Carlo simulations for final high-level control policy. Slopes are normally distributed with $\mu_\gamma = 0$ and $\sigma_\gamma = 5$ deg. One step look ahead experiences a normal noise with zero mean and standard deviation $\sigma_l = 1°$. 10 thousand iterations were conducted until failure and the results are presented on the last row. Estimation using (2.12) is carried on the dense mesh.

	$\sigma_\gamma = 7°$	$\sigma_\gamma = 8°$	$\sigma_\gamma = 9°$	$\sigma_\gamma = 10°$
Estimation using $\dfrac{1}{1 - \lambda_2}$	637.4	167.9	66.45	33.99
Monte Carlo simulations	633.23	171.41	68.35	35.24

---

[2]Note that c is bounded between zero and number of states minus 1.
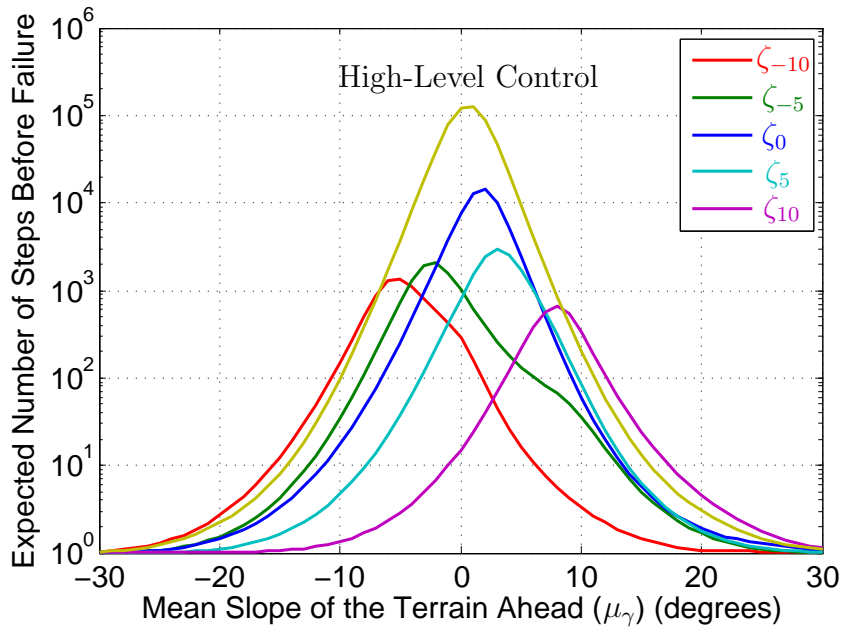
Figure 5.9: Stability of the final high-level policy. For this specific roughness the performance is an order of magnitude improvement compared to the most stable low-level controller. See Figure 5.2 to distinguish five fixed controllers shown in this picture. The expected numbers of steps before falling are calculated using (2.12) versus μ_γ. Slopes ahead of the robot are assumed to be normally distributed with $\sigma_\gamma = 5$ deg. Slope estimation experiences a normal noise with zero mean and standard deviation $\sigma_l = 1°$.

5.3   Incorporating Secondary Metrics

In section 4.4 we showed how to incorporate metrics like speed and energy efficiency into low-level controller optimization. Here we repeat the same process for high-level control as in [Saglam and Byl, 2014b]. As case demonstration in this chapter, we employ the two controllers in Table 4.3, one of which is more energy efficient but less stable. Intuitively the high-level controller should prefer the efficient controller when the slope ahead is mild and state is appropriate. For stability, it better pick the more stable low-level controller otherwise.

For simplicity and proof of concept, in this section we neglect the sensor noises and discretization errors. To incorporate energy efficiency into high-level control design, unlike (5.6) and (5.12), we use

$$V(i) := \sum_{\gamma \in \Gamma} \max_{\zeta} \left\{ P_\Gamma(\gamma) \sum_{j} T_{ij}^d(\gamma, \zeta) \left(R_{ij}(\gamma, \zeta) + \alpha \, V(j) \right) \right\}. \qquad (5.24)$$

The reward is given by

$$R_{ij}(\gamma, \zeta) = \begin{cases} 0, & j = 1, \\ 1 - \beta \, \mathrm{COT}(x_i, \gamma, \zeta), & \text{otherwise,} \end{cases} \qquad (5.25)$$

where $\mathrm{COT}(x_i, \gamma, \zeta)$ is the cost of transport when the robot takes a step from state x_i using controller ζ and the slope ahead is γ. Figure 5.10 shows the performance of high-level controller obtained using $\beta = 1$. It is as stable as the robust controller and almost as energy efficient as the other controller. To derive the expected cost of transport, we computed the expected energy expenditure and expected distance using the methodology explained in Appendix A.3.

Comparing Figure 5.10 and Table 4.3, we note that the relatively energy efficient low-level controller turned out to be a little off from what is calculated before, but the results are fairly close.

59
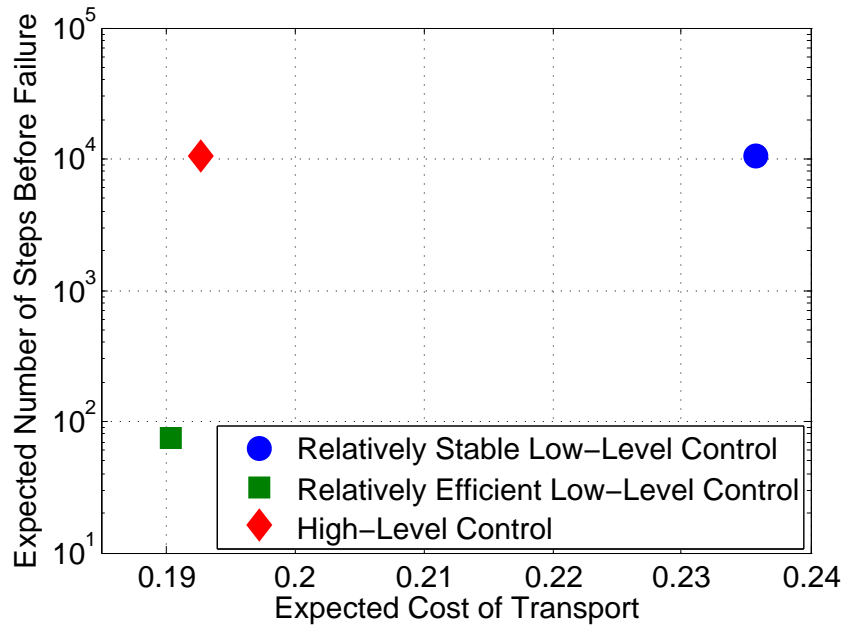
Figure 5.10: Incorporating secondary metrics on high-level control design. The low-level controllers are as listed in Table 4.3. The high-level controller is stable as the robust low-level controller and almost as energy efficient as the other low-level controller. To derive the expected cost of transport, we first needed to calculate expected energy expenditure and expected distance using the methodology explained in Section A.3. The expected numbers of steps before falling are calculated using (2.12). Slopes ahead of the robot are assumed to be normally distributed with $\mu_\gamma = 0$ and $\sigma_\gamma = 5$ deg.

Overall this chapter motivates the use of high-level controller for increased autonomy and better performance, including stability, speed, and energy efficiency.

Chapter 6

Conclusions and Future Work

Toward capable robots operating reliably in real-world environments, this thesis quantified robustness to variations with an intuitive and meaningful metric, which is later used to optimize and benchmark a given control scheme. Specifically, we introduced extended hybrid zero dynamics framework which produced quantitatively good performance for two-legged walking on rough terrain.

The proposed mathematical tool in this thesis is based on discretization of dynamics to treat the system as a Markov chain representation which, in addition to reliability, was used to calculate expected speed and energy consumption under variations such as rough terrain. As importantly, the process of learning the discretized system provided extremely valuable information about the dynamics which was later used to obtain high-level behavioral algorithms for autonomous walking. Overall, this thesis proposes a systematic way of obtaining controllers that are autonomous and reliable in a quantifiable manner.

On top of obtaining a Markov chain representation in Chapter 2, Appendix A explained our approach with toy examples to motivate researchers to employ our methodology. These newly designed tools are highly applicable to a wide range of robotic systems such as 3D bipeds, hopping, running, and experimental robots. Moreover, many interest-

ing applications can be identified and addressed in various other dynamical systems that are highly amenable to quantification of performance under stochasticity, which includes physical and social graphs, epidemics, queues, and teleoperation.

One of two major future directions is to exploit this mentioned applicability. Second, we would like to keep developing the tools of this thesis to advance the science of highly-dynamic robots. In particular, for two-legged walking we are interested in more realistic and higher dimensional biped and terrain models. The former can potentially be a 3D walker with complex foot, while the latter can consider varying friction coefficient, obstacles, and holes to be avoided. The framework is already capable of measuring the advantages of additional control actions such as reflexes. We also would like to study the benefits of more than one-step lookahead to the terrain. Very interestingly, our powerful optimization technique allows directly mapping terrain estimation and state information to torques, which is to be exploited in a future work. Incorporating more advanced machine learning techniques has potential to provide even better autonomy and robustness to the system.

Appendix A

First Passage Value

Many interesting applications can be identified and addressed in various dynamical systems that are highly amenable to quantification of performance under stochasticity, including robots, physical and social graphs, epidemics, and teleoperation. Often for such systems, eigenalysis yields a meaningful and intuitive measure of overall stability, namely system-wide mean first passage time, which we mainly refer to as expected number of steps before failure in this thesis.

First passage time, aka first hitting time, gives survival duration until a specific event or set of events, such as death or failure. In discrete-time models, the expected number of discrete time steps of survival corresponds to mean first passage time (MFPT). While different initial conditions (states) often result in different MFPTs, for many *metastable*[1] systems a scalar called *system-wide* MFPT is an accurate estimate across a large set of states, and it can potentially well represent the stability.

More recently, the tools for quantifying metastable systems has been applied to walking robots to predict how a robot performs over variable terrain for a given control policy [Byl and Tedrake, 2009], [Saglam and Byl, 2014c]. For such analyses, the walking robot,

---

[1]See Chapter 2 for metastability.

the environment, the system noise, and the control actions can be modeled together as a Markov chain as explained in Chapter 2. Assuming that the initial state of the robot lies within "metastable region" of state space, the eigenvalues of the state transition matrix of the Markov chain, specifically the largest eigenvalue not associated with the (absorbing) failed system state, can be used to predict the number of steps the robot can take before failing.

Using a Europe tour game, this chapter explains the robotic locomotion community the dynamics of metastable walking. It also aims to encourage countless controls applications of MFPT calculation for metastable systems. Finally, a more generalized concept of first passage time, namely first passage value, is presented to discuss both the mean and variability of a value of interest for a metastable system.

A.1   Toy Example: Europe Tour

Consider a person traveling between some of the largest cities in Europe shown in Figure A.1. After spending a day that person either stays in the same city, or moves to one of the connected cities. The probability of action is directly proportional to the population of the next city. For instance, when in Madrid,

$$\text{Probability of staying in Madrid} = \frac{\text{Population of Madird}}{\text{Population of Madird} + \text{Population of Paris}}.$$
(A.1)

For the Europe tour game, Istanbul represents failure[2] for a robot. The number of days before reaching Istanbul is analogous to the number of steps before failure for a walker. Each of the remaining cities corresponds to a (discretized) state of the robot. For an explanation of discretization, please see Chapter 2.

---

[2]Istanbul may also represent success depending on the application. See epidemics example of this appendix. In general we are interested in expected number of steps before escape (failure or success).

Figure A.1: Populations of Europe's most populated 8 cities excluding Russia. Cities are ordered by their population as indicated in parenthesis. For instance, Athens (State 3) is the third most crowded city in this map. Consider a person traveling between these cities. After spending a day that person either stays in the same city, or moves to one of the connected cities. The probability of action is directly proportional to the population of the next city. The resulting Markov Chain has similarities with walking dynamics.

The author would like to thank Beril Pisgin for drawing this picture.

Note that as time goes to infinity, the probability of visiting Istanbul becomes 1. However, if the population of Paris was infinite, then being in Paris would be stable and the tourist would spend infinitely many days without going to Istanbul. This behavior is analogous to periodic walking on flat terrain. For an appropriate initial condition, the robot would never leave the periodic orbit under deterministic conditions, which implies walking infinitely many steps without failure. By taking a Poincaré section intersecting walking motion, this periodic orbit can be represented as a fixed point on the corresponding Poincaré map. So, Paris is analogous to the fixed point on the Poincaré map for the robot walking in terms of mapping back to itself at each step. Moreover, Madrid, London, Rome, and Berlin are in the basin of attraction for stable walking. Starting from

any one of those cities means going to Paris. However, Athens is destined to be absorbed rapidly, because it is only connected to Istanbul. Similar to a tripped walker, Kiev is a risky state, because it may lead to Istanbul, which means failure. Otherwise going Berlin results in stable walking at Paris.

For dynamic walking on rough terrain, metastability is present if the number of steps before failure is very high but finite. In the tour example, we assume the population of Paris is 1 billion to study metastability. Then, Istanbul is globally asymptotically stable, but a tourist in Paris is expected to spend a large number of days before going to Istanbul. Define reachable (controllable) subspace as the union of states that might transition from (to) Paris. Then, Paris, Madrid, London, Rome, and Berlin are reachable and controllable states, whereas Athens is not a controllable or a reachable state. In addition, imagine having Barcelona in this map too, from which the tourist can go to Madrid, but not vice versa. Then Barcelona would be a controllable but not reachable state. As following sections justify, unreachable states do not affect the system-wide MFPT value. Thus, only reachable state space needs to be meshed for a walking robot and the curse of dimensionality can be avoided.

A.2   Absorbing Markov Chains

To calculate the expected number of steps before a specific 'escape' event, the corresponding set needs to be modeled as an absorbing 'halt' state. For the Europe tour game, this modeling is achieved by assuming it is impossible to leave Istanbul. Remember that Istanbul is analogous to the set of failure modes for a walking robot, no matter how the robot failed. Without loss of generality, let the halt state be State 1 (x_1) and note that absorption assumption does not change the dynamics until State 1.

For the Markov Chain under consideration, the state distribution vector at step n is

denoted by $\mathbf{p}[n]$ and defined by

$$p_i[n] := \Pr(\mathbf{X}[n] = x_i). \tag{A.2}$$

So $p_i[n]$ corresponds to the probability of being at state x_i at step n. Since probability cannot be negative, $\mathbf{p}[n]$ is a non-negative vector, and because the system has to be at a state at any step, $\mathbf{p}[n]$ sums to 1. The state transition matrix, aka the Markov matrix or the stochastic matrix, is defined by

$$T_{ij} := \Pr(\mathbf{X}[n+1] = x_j \mid \mathbf{X}[n] = x_i). \tag{A.3}$$

So, the entry of $\boldsymbol{T}$ on the ith row and jth column gives the probability of transitioning from state x_i to state x_j. To illustrate, the Markov chain for the Europe tour game is represented with

$$\boldsymbol{T} = \begin{bmatrix} 1 & 0 & 0 & 0 & 0 & 0 & 0 & 0 \\ 0 & 0.0082 & 0 & 0.0035 & 0 & 0 & 0 & 0.9883 \\ 0.7905 & 0 & 0.2095 & 0 & 0 & 0 & 0 & 0 \\ 0.0138 & 0.0081 & 0 & 0.0034 & 0 & 0.0028 & 0 & 0.9720 \\ 0 & 0 & 0 & 0 & 0.0032 & 0 & 0 & 0.9968 \\ 0.6899 & 0 & 0 & 0.1714 & 0 & 0.1387 & 0 & 0 \\ 0.0139 & 0 & 0 & 0 & 0 & 0 & 0.0027 & 0.9833 \\ 0 & 0.0082 & 0 & 0.0035 & 0.0032 & 0 & 0.0027 & 0.9825 \end{bmatrix}. \tag{A.4}$$

Indices on Figure A.1 yield that $T_{64} = 0.1714$ is the probability of moving from Kiev to Berlin. Just like $\mathbf{p}[n]$, $\boldsymbol{T}$ is non-negative. And because any state transitions (possibly to the halt state or the starting state itself) after each step, each row sums to one. Let $\ell > 1$ be the number of states. So, the state transition matrix is ℓ by ℓ. The state transition matrix gives the next state distribution, given the current one by

$$\mathbf{p}[n+1] = \boldsymbol{T}' \, \mathbf{p}[n] = (\boldsymbol{T}')^{n+1} \, \mathbf{p}[0], \tag{A.5}$$

67

where the prime ($'$) symbol denotes the transpose operation.

Let λ be an eigenvalue of $\boldsymbol{T}$. Then, there exists a non-zero vector $\mathbf{v}$ such that

$$\boldsymbol{T}\mathbf{v} = \lambda\mathbf{v}. \tag{A.6}$$

As in [Matthews, 1995], let k be such that $|v_j| \leq |v_k|$ for all $1 \leq j \leq \ell$. Equating the k-th components in equation (A.6) gives

$$\sum_j T_{kj}v_j = \lambda v_k. \tag{A.7}$$

As a result,

$$|\lambda v_k| = |\lambda|\,|v_k| = \left|\sum_j T_{kj}v_j\right| \leq \sum_j T_{kj}|v_j| \leq \sum_j T_{kj}|v_k| = |v_k|, \tag{A.8}$$

where $T_{kj} \geq 0$ and $\sum_j T_{kj} = 1$ are used. $|\lambda||v_k| \leq |v_k|$ implies $|\lambda| \leq 1$.

For the rest of this chapter, the transpose of $\boldsymbol{T}$ is used to make the following sections easier to follow. Since $\boldsymbol{T}$ is square, $\boldsymbol{T}'$ has the same eigenvalues as $\boldsymbol{T}$. Due to the nature of transpose operation and the structure of $\boldsymbol{T}$, each column of $\boldsymbol{T}'$ sums to one.

Remember that x_1 is an absorbing state, which represents the end of game. Then, $\boldsymbol{T}'$ can be partitioned as

$$\boldsymbol{T}' = \begin{bmatrix} 1_{1\times 1} & \mathbf{T_1} \\ \mathbf{0} & \hat{\boldsymbol{T}} \end{bmatrix}_{\ell\times\ell}. \tag{A.9}$$

Note that $\lambda = 1$ and $\mathbf{v} = [1\ 0\ ...\ 0]'$ satisfies the equation

$$\boldsymbol{T}'\mathbf{v} = \lambda\mathbf{v}. \tag{A.10}$$

To distinguish (possibly non-distinct) eigenvalues, note them by λ_j, where $1 \leq j \leq \ell$. Without loss of generality, let $\lambda_1 = 1$ and the associated basis vector be $\mathbf{v}_1 = [1\ 0\ ...\ 0]'$.

Existence of Jordan normal form for any square matrix is fundamental to Linear Algebra. Consider a Jordan normal form of $\hat{\boldsymbol{T}}$ given by

$$\hat{\boldsymbol{T}} = \hat{\boldsymbol{V}}\hat{\boldsymbol{J}}\hat{\boldsymbol{V}}^{-1}, \tag{A.11}$$

68

Then, as will be verified, a Jordan normal form of $\boldsymbol{T'}$ is given by

$$\boldsymbol{T'} = \boldsymbol{V}\boldsymbol{J}\boldsymbol{V}^{-1}, \tag{A.12}$$

$$\text{where } \boldsymbol{J} = \begin{bmatrix} 1 & \mathbf{0} \\ \mathbf{0} & \boldsymbol{\hat{J}} \end{bmatrix}, \tag{A.13}$$

$$\text{and } \boldsymbol{V} = \begin{bmatrix} 1 & -[1 \,...\, 1]\boldsymbol{\hat{V}} \\ \mathbf{0} & \boldsymbol{\hat{V}} \end{bmatrix}. \tag{A.14}$$

Note that the sum of each column of $\boldsymbol{V}$ equals zero, except the first one. Furthermore, these columns form a basis in $\mathbb{R}^\ell$. Equation (A.12) can be verified as follows. The inverse of $\boldsymbol{V}$ is

$$\boldsymbol{V}^{-1} = \begin{bmatrix} 1 & [1 \,...\, 1] \\ \mathbf{0} & \boldsymbol{\hat{V}}^{-1} \end{bmatrix}. \tag{A.15}$$

Then, the right hand side of (A.12) can be calculated as

$$\begin{bmatrix} 1 & [1 \,...\, 1] - [1 \,...\, 1]\boldsymbol{\hat{V}}\boldsymbol{\hat{J}}\boldsymbol{\hat{V}}^{-1} \\ 0 & \boldsymbol{\hat{V}}\boldsymbol{\hat{J}}\boldsymbol{\hat{V}}^{-1} \end{bmatrix} = \begin{bmatrix} 1 & [1 \,...\, 1](\mathbf{I} - \boldsymbol{\hat{T}}) \\ 0 & \boldsymbol{\hat{T}} \end{bmatrix}. \tag{A.16}$$

Equation (A.12) is thus verified because $\mathbf{T_1} + [1 \,...\, 1]\boldsymbol{\hat{T}} = [1 \,...\, 1]$ (columns of $\boldsymbol{T'}$ sum to one).

The spectrum of $\boldsymbol{\hat{T}}$, denoted by $\sigma(\boldsymbol{\hat{T}})$, is the set of distinct eigenvalues of $\boldsymbol{\hat{T}}$. The spectral radius of $\boldsymbol{\hat{T}}$ is given by

$$\rho(\boldsymbol{\hat{T}}) = \max_{\lambda \in \sigma(\boldsymbol{\hat{T}})} |\lambda|. \tag{A.17}$$

Let the spectral radius be $r = \rho(\boldsymbol{\hat{T}})$. As proven in [Meyer, 2000], because $\boldsymbol{\hat{T}}$ is a non-negative square matrix,

1. $r \in \sigma(\boldsymbol{\hat{T}})$ (r is an eigenvalue of $\boldsymbol{\hat{T}}$),

2. $\hat{\boldsymbol{T}}\mathbf{z} = r\mathbf{z}$ for some $\mathbf{z} \in \mathcal{N} = \{v| \ v \geq 0 \text{ with } v \neq 0\}$.

Let $\lambda_2 := r$ and $\mathbf{v_2}$ refer to the associated column in $\boldsymbol{V}$. Then, $\mathbf{v_2} = [- \|\mathbf{z}\|_1 \ \mathbf{z}']'$. Now, consider the state distribution

$$\phi := \begin{bmatrix} 0 \\ \dfrac{\mathbf{z}}{\|\mathbf{z}\|_1} \end{bmatrix} = \mathbf{v_1} + \frac{1}{\|\mathbf{z}\|_1}\mathbf{v_2}. \tag{A.18}$$

ϕ is called the *metastable distribution*. Note that it is a valid initial state distribution since it sums to one and each element is non-negative. For the metastable Europe tour,

$$\lambda_2 \approx 1 - 9.2393 \times 10^{-5} \text{ and } \phi \approx \begin{bmatrix} 0 \\ 0.0081 \\ 0 \\ 0.0035 \\ 0.0031 \\ 1.1 \times 10^{-5} \\ 0.0027 \\ 0.9826 \end{bmatrix} \tag{A.19}$$

λ_2 being close to one means escapes are rare and the system is metastable. The first element of ϕ is the probability of being at x_1, and it equals zero by definition. In this metastable distribution, the probability of being in Paris is high due to its high population. However, Athens does not appear in the metastable distribution, because it is connected only to the absorbing state. The probability of being in Kiev is close to zero, because several steps are typically enough to move directly from Kiev to either Istanbul (the absorbing state) or Berlin. The latter almost implies going to Paris in the following step due to high population there.

Taking a step when ϕ is the initial condition results in

$$\boldsymbol{T}'\phi = \boldsymbol{T}'\left(\mathbf{v_1} + \frac{1}{\|\mathbf{z}\|_1}\mathbf{v_2}\right) = \mathbf{v_1} + \frac{\lambda_2}{\|\mathbf{z}\|_1}\mathbf{v_2}. \tag{A.20}$$

Naturally, the resulting distribution is also non-negative and sums to one. In addition, the first component is

$$1 + \frac{\lambda_2}{\|\mathbf{z}\|_1}(-\|\mathbf{z}\|_1) = 1 - \lambda_2, \tag{A.21}$$

which means the system escaped with probability $1 - \lambda_2$. Furthermore, given the system did not escape, $\boldsymbol{\phi}$ is the final probability distribution for the states. This fact can be seen by zeroing the first component of $\boldsymbol{T}'\boldsymbol{\phi}$ and scaling to sum to one. So, when $\boldsymbol{\phi}$ is the initial state distribution, the probability of escaping is $1 - \lambda_2$, the probability of staying in the same distribution ($\boldsymbol{\phi}$) is λ_2.

Now let the initial condition be $\boldsymbol{\phi}$, that is $\mathbf{p}[0] = \boldsymbol{\phi}$. The expected number of steps before escape corresponds to the term mean first passage time (MFPT) in [Byl and Tedrake, 2009]. The higher MFPT is, the more stable a system is said to be. Two cases are possible depending on the probability of taking a step: If $\lambda_2 = 1$, then the probability of escape is zero. In this case the system takes infinitely many steps without escaping to the halt state. The other case ($\lambda_2 < 1$) is relatively more complicated and interesting as focused next.

A.2.1   System-wide First Passage Time

Given the probability of taking a step without escaping is $\lambda_2 < 1$, the probability of taking n steps only, equivalently escaping at the nth step is

$$\Pr(\mathbf{X}[n] = x_1, \ \mathbf{X}[n-1] \neq x_1) = \lambda_2^{n-1}(1 - \lambda_2). \tag{A.22}$$

Realize that as $n \to \infty$, the right hand side goes to zero, which means the escape is inevitable. The step ended up escaping also counts as a step, which can be verified considering escaping at the first step (taking 1 step only). When $n = 1$ is substituted,

$1 - \lambda_2$ is obtained as expected. Then, the expected number of steps can be calculated as

$$
\begin{aligned}
\text{MFPT} &= \text{E[FPT]} \\
&= \sum_{n=1}^{\infty} n \, \text{Pr}(\mathbf{X}[n] = x_1, \ \mathbf{X}[n-1] \neq x_1) \\
&= \sum_{n=1}^{\infty} n \lambda_2^{n-1}(1 - \lambda_2) = \frac{1}{1 - \lambda_2},
\end{aligned}
\tag{A.23}
$$

where FPT stands for first passage time and the fact that $\lambda_2 < 1$ is used. As a result, MFPT can then be calculated using

$$
M = \begin{cases}
\infty & \lambda_2 = 1, \\
\dfrac{1}{1 - \lambda_2} & \lambda_2 < 1.
\end{cases}
\tag{A.24}
$$

The MFPT for the Europe tour is

$$
M \approx 10{,}823.
\tag{A.25}
$$

So, if $\mathbf{p}[0] = \phi$, then the system takes approximately 10,823 steps on average.

The standard deviation of FPT can be calculated by

$$
\begin{aligned}
\text{E[FPT}^2] &= \sum_{n=1}^{\infty} n^2 \, \text{Pr}(\mathbf{X}[n] = x_1, \ \mathbf{X}[n-1] \neq x_1) \\
&= \sum_{n=1}^{\infty} n^2 \lambda_2^{n-1}(1 - \lambda_2) = \frac{1 + \lambda_2}{(1 - \lambda_2)^2}
\end{aligned}
$$

$$
\implies \sqrt{\text{E[FPT}^2] - (\text{E[FPT]})^2} = M\sqrt{\lambda_2}.
\tag{A.26}
$$

Then for the Europe tour, the standard deviation of FPT is $M\sqrt{\lambda_2} \approx 10{,}822$. Note that λ_2 being close to one results in a standard deviation close to the mean.

The MFPT vector, $\mathbf{m}$, gives the MFPT for each state and it is defined as

$$
m_i := \begin{cases}
0 & i = 1, \\
1 + \sum_{j} T_{ij} m_j & otherwise.
\end{cases}
\tag{A.27}
$$

Equation (A.27) says it takes zero steps to go to the halt state if the system escaped already. Otherwise, the number of steps until halt is 1 less after a step is taken. For the Europe tour, the solution to (A.27) is

$$\mathbf{m} \approx \begin{bmatrix} 0 \\ 10,825 \\ 1 \\ 10,652 \\ 10,825 \\ 2,121 \\ 10,674 \\ 10,824 \end{bmatrix}. \tag{A.28}$$

This vector says if the initial state is x_2, then $10,825$ steps are expected before escape. Note that London, Paris, Madrid, Berlin and Rome have MFPT close to the system-wide MFPT M. Also the MFPT of Istanbul and Athens are very small. However, Kiev has a MFPT that is not close to zero or the system-wide MFPT, because $m_1 = 0$, $m_4 \approx M$, and

$$m_6 = \boldsymbol{T_{61}} m_1 + \boldsymbol{T_{64}} m_4 + \boldsymbol{T_{66}} m_6 \tag{A.29}$$

implies

$$m_6 \approx \frac{\boldsymbol{T_{64}}}{1 - \boldsymbol{T_{66}}} = 2,153. \tag{A.30}$$

For walking robots, the picture is the same. Metastable states are almost equally stable ($m_2 \approx m_4 \approx m_5 \approx m_7 \approx m_8 \approx M$) and some states are doomed to fail ($m_3 = 1$). Also some states are risky and likely to fail in the next step, otherwise they are mapped to the metastable region, just like Kiev. This structure is the case when memory constant, which is to be defined shortly, is small.

By using (A.9), it is straightforward to obtain

$$m = \begin{bmatrix} 0 \\ (\mathbf{I} - \hat{\boldsymbol{T}}')^{-1}\mathbf{1} \end{bmatrix}. \tag{A.31}$$

$(I - \hat{T}')$ is invertible when $\lambda_2 < 1$, which is the hidden assumption made while defining the MFPT vector. The system-wide MFPT calculated in (A.23) can be also obtained by

$$M = \mathbf{m}'\boldsymbol{\phi} = \frac{1}{\|\mathbf{z}\|_1}[1\ ...\ 1](\mathbf{I} - \hat{\boldsymbol{T}})^{-1}\mathbf{z}. \tag{A.32}$$

This equivalence makes sense because each state has its own MFPT, and MFPT of the metastable distribution is just a convex combination of each state's MFPT weighted according to $\boldsymbol{\phi}$. Indeed

$$\begin{aligned}
\hat{M} &= \frac{1}{\|\mathbf{z}\|_1}[1\ ...\ 1](\mathbf{I} - \hat{\boldsymbol{T}})^{-1}\mathbf{z} \\
&= \frac{1}{\|\mathbf{z}\|_1}[1\ ...\ 1](\mathbf{I} - \hat{\boldsymbol{T}})^{-1}(\mathbf{I} - \hat{\boldsymbol{T}} + \hat{\boldsymbol{T}})\mathbf{z} \\
&= \frac{1}{\|\mathbf{z}\|_1}[1\ ...\ 1](\mathbf{I} + (\mathbf{I} - \hat{\boldsymbol{T}})^{-1}\hat{\boldsymbol{T}})\mathbf{z} \\
&= \frac{1}{\|\mathbf{z}\|_1}[1\ ...\ 1]\mathbf{z} + \frac{1}{\|\mathbf{z}\|_1}[1\ ...\ 1](\mathbf{I} - \hat{\boldsymbol{T}})^{-1}\hat{\boldsymbol{T}}\mathbf{z} \\
&= 1 + \lambda_2 \frac{1}{\|\mathbf{z}\|_1}[1\ ...\ 1](\mathbf{I} - \hat{\boldsymbol{T}})^{-1}\mathbf{z} \\
&= 1 + \lambda_2\hat{M} \quad \Longrightarrow \quad \hat{M} = 1/(1 - \lambda_2) = M.
\end{aligned} \tag{A.33}$$

Note that M is upper bounded by the largest element in $\mathbf{m}$. In fact, any initial state distribution, $\mathbf{p}[0]$, has a MFPT that is a convex combination of the m_i values.

MFPT of the metastable distribution is useful for various reasons. First of all, it is a lower bound for average steps taken from at least one of the states, because it is a convex combination of m_is. So, there exists state(s) at least as stable. Secondly, it is a meaningful and intuitive measure of overall stability. Often systems quickly converge to their metastable distributions, where MFPT becomes the true value. Thirdly, system-wide MFPT also has advantages over calculating the MFPT vector. In case $\boldsymbol{T}$ is large,

estimating the second largest eigenvalue is relatively easy, whereas finding the inverse to calculate MFPT vector costs more time. Also, a scalar representing the stability is much easier to understand than a possibly huge vector.

Assume $\boldsymbol{T}$ has distinct eigenvalues. Please see [Saglam and Byl, 2014a] for other cases. Denote the initial distribution as

$$\mathbf{p}[0] = c_1\mathbf{v_1} + c_2\mathbf{v_2} + ...c_\ell\mathbf{v_\ell}. \tag{A.34}$$

Note that $c_1 = 1$ to have $\|\mathbf{p}[0]\|_1 = 1$. Then,

$$\mathbf{p}[n] = (\boldsymbol{T'})^n\mathbf{p}[0] = \mathbf{v_1} + c_2\lambda_2^n\mathbf{v_2} + ... + c_\ell\lambda_\ell^n\mathbf{v_\ell}. \tag{A.35}$$

In the light of this section, the metastable distribution is also given by

$$\phi_i = \lim_{n\to\infty} \Pr(X[n] = x_i \ |X[n] \neq x_1]), \tag{A.36}$$

when the limit exists. It exists, for example, when the eigenvalues are distinct.

A.2.2   How Quickly is the Initial Distribution Forgotten?

The initial distribution (condition) is forgotten if either the distribution is the metastable distribution ($\mathbf{p} = \boldsymbol{\phi}$) or the game ended ($\mathbf{p} = [1 \ 0 \ ... \ 0]'$). So, the question can be paraphrased as "how quickly does the system converge toward the metastable distribution, given it is not absorbed yet?". For systems with distinct eigenvalues,

$$\text{memory constant} = \frac{1 - \lambda_2}{1 - |\lambda_3|} \tag{A.37}$$

is a dimensionless indicator of the convergence speed.

The definition of the memory constant is motivated by the fact that $\sum_{n=0}^{\infty} \lambda_i^n = 1/(1 - \lambda_i)$ for $|\lambda_i| < 1$. Although this property also holds for complex λ_i values, since $|\lambda_3^n| = |\lambda_3|^n$, memory constant uses $1/(1-|\lambda_3|)$ to quantify how many steps it takes before

vanishing. Higher λ_3 results in larger $1/(1 - |\lambda_3|)$, which means the initial condition is forgotten slower and more steps are required to forget the same amount of initial condition information. λ_3 gives the worst case scenario, so the memory constant is a conservative value. $(1/(1 - |\lambda_3|))$ is divided by $M = 1/(1 - \lambda_2)$ for a relative memory constant, which is upper bounded by 1.

Note that the memory constant being smaller than ε implies $M > 1/\varepsilon$. Thus, small memory constants require metastability. If, on the other hand, the memory constant is very close to one, then there is another mode almost as stable as the one associated with λ_2. In such cases it may be useful to use the next $|\lambda_i|$ instead of $|\lambda_3|$, until a small memory constant is obtained. In particular, when the eigenvalues are not necessarily distinct, it might be the case that $\lambda_2 = |\lambda_3|$.

For the Europe tour example, the memory constant is 1.1688×10^{-4}. This small memory constant indicates the structure mentioned earlier, where there are metastable states, controllable unreachable states, doomed states, risky states, and halt state. Some other motivating applications of MFPT calculation is presented later in this Chapter.

A.3   Mean First Passage Value

Calculating the discrete time to a state of interest has potential to be greatly useful, but in some applications, metrics other than expected number of steps before absorption are of interest. To illustrate, instead of how many decisions it took before reaching Istanbul, travel-time or distance to Istanbul might be needed. For this matter, MFPT can be generalized as mean first passage value (MFPV), where "value" depends on the task, for example, mean first passage distance. So, MFPT is a special case of MFPV, where value is discrete time steps.

Redefining $\mathbf{m}$ from (A.27) as the MFPV vector gives the MFPV for each state as

$$m_i := \begin{cases} 0 & i = 1 \\ \sum_j T_{ij} R_{ij} + \sum_j T_{ij} m_j & otherwise, \end{cases} \tag{A.38}$$

where R_{ij} is the reward (value) of transitioning from state x_i to x_j. Then, vector $\mathbf{m}$ can be calculated as

$$\mathbf{m} = \begin{bmatrix} 0 \\ (\mathbf{I} - \hat{\boldsymbol{T}}')^{-1} \begin{bmatrix} \sum_j T_{2j} R_{2j} \\ . \\ . \\ . \\ \sum_j T_{\ell j} R_{\ell j} \end{bmatrix} \end{bmatrix}. \tag{A.39}$$

And the (system-wide) MFPV is

$$M = \mathbf{m}' \boldsymbol{\phi}. \tag{A.40}$$

For the metastable Europe tour example, consider the information provided in Table A.1. Then, using (A.40) mean first passage distance can be calculated to be 325.68 thousand km. This calculation is achieved by setting, for example, $R_{24} = 1,098$ km, which corresponds to the distance between London, and Berlin.

	Time (h:m)	Distance (km)
London (2) - Paris (8)	5:06	454
London (2) - Berlin (4)	10:25	1,098
Madrid (5) - Paris (8)	11:10	1,270
Rome (7) - Paris (8)	12:46	1,419
Berlin (4) - Paris (8)	9:18	1,055
Berlin (4) - Kiev (6)	14:41	1,329
Berlin (4) - Istanbul (1)	21:39	2,210
Kiev (6) - Istanbul (1)	19:00	1,459
Rome (7) - Istanbul (1)	22:46	2,262
Athens (3) - Istanbul (1)	11:13	1,095

Table A.1: Travel times and distances for the roads of Europe map in Figure A.1. For the game explained in that figure's caption, the values in this table are used to calculate the expected distance and time before visiting Istanbul.

The travel-time only (excluding the days spent in a city) is calculated by setting $R_{ii} = 0$. Then, it takes 128 days on average before Istanbul. The MFPV vector for this case is

$$\mathbf{m} = \begin{bmatrix} 0 \\ 128.4756 \\ 0.4674 \\ 126.6098 \\ 128.7334 \\ 25.9478 \\ 127.0149 \\ 128.2681 \end{bmatrix} \text{ days.} \quad (A.41)$$

Remember that a random decision is made after spending a day in the city. For the MFPV calculation, to include those days spent in a city, the reward needs to be set such that $R_{ii} = 1$ day. This setting results in a MFPV of 29 years, which is much higher than 128 days. One reason of this difference is because once in Paris, there is a 0.9825 probability to stay in Paris.

In addition, MFPV does not need to have a physical meaning. Multiple objectives can be included in a single value function, for example for walking robots failure events, such as falling down, can be penalized while also rewarding fast speed and low energy use. The value, or the cost function, does not need to have a physical correspondence. Number of steps minus 10^{-3} times energy consumption is a valid value definition. Please see [Saglam and Byl, 2014b] for further details and usage of this example.

A.4   Confidence Levels on Value

In some applications, instead of the mean FPV, a conservative FPV bound for a particular "confidence level" pr is needed. In other words, a value above lower first passage time (LFPT) would be observed with probability pr, and a value below upper first passage time (UFPT) would be observed with probability pr.

A.4.1   First Passage Time

The probability of taking more than LFPT steps is λ_2^{LFPT}. Then, the lower bound on number of steps taken with probability pr can be calculated by

$$\text{LFPT}(pr) = log_{\lambda_2} pr. \tag{A.42}$$

Note that LFPT(1)=0, so taking only a single step is guaranteed, which leads to the halt state. The probability of taking less than UFPT steps is $1 - \lambda_2^{\text{UFPT}-1}$. Then, the upper

bound on number of steps taken with probability pr is

$$\text{UFPT}(pr) = log_{\lambda_2}(1 - pr) + 1. \tag{A.43}$$

Since $\lim\limits_{pr \to 1} \text{UFPT}(pr) = \infty$, it may theoretically take infinitely many steps before converging to the halt state. Then FPT can be limited for a given probability as

$$\text{LFPT} \leq \text{FPT} \leq \text{UFPT}. \tag{A.44}$$

Having LFPT<UFPT requires $pr > \lambda_2/(1 + \lambda_2)$, where right hand side equals 0.5 for $\lambda_2 = 1$. To illustrate the advantage of looking to FPT, consider the metastable Europe tour example. The probability of the journey taking more than $M = 10,823$ days is only 36.79 %. On the other hand,

$$1,140 \leq \text{FPT}(0.9) \leq 24,921,$$
$$108 \leq \text{FPT}(0.99) \leq 49,842. \tag{A.45}$$

These numbers are not coincidence. As $\lambda_2 \to 1$, the probability of taking M steps is

$$\lim\limits_{\lambda_2 \to 1} \lambda_2^{1/(1-\lambda_2)} = \frac{1}{e} \approx 0.3679. \tag{A.46}$$

In fact, 0.3679 is an upper limit for the probability of taking $1/(1 - \lambda_2)$ steps for any λ_2. In addition, when λ_2 and pr are close to one,

$$\text{LFPT}(pr) = \frac{ln(pr)}{ln(\lambda_2)} \approx \frac{1 - pr}{1 - \lambda_2} = (1 - pr)M, \tag{A.47}$$

$$\text{UFPT}(pr) = \frac{ln(1 - pr)}{ln(\lambda_2)} + 1 \approx -ln(1 - pr)M, \tag{A.48}$$

where M denotes MFPT.

LFPT is of interest for walking systems, to give a conservative bound on steps to failure, while UFPT would be helpful in modeling epidemics, to obtain a conservative time when everyone is healthy, which means recurrence to an "all-healthy" system state.

A.4.2   First Passage Value

Using MFPT and MFPV value per step can be used to write

$$\text{FPV} = \frac{\text{MFPV}}{\text{MFPT}} \, \text{FPT}, \tag{A.49}$$

where FPV denotes first passage value. When the value is the distance in the metastable Europe tour example,

$$3.4 \times 10^4 \leq \text{FPV}(0.9) \leq 7.5 \times 10^5,$$
$$3.2 \times 10^3 \leq \text{FPV}(0.99) \leq 1.5 \times 10^6. \tag{A.50}$$

So, with probability 0.99, the journey takes more than 3.2 thousand or less than 1.5 million kilometers.

A.5   Controlling the Europe Tour

In order to control a system, a goal is needed. For instance, going to Istanbul as quickly as possible could be a goal for the Europe tour. It is then useful to quantify the performance toward achieving that goal. For example, number of days before reaching Istanbul would be a meaningful metric to minimize. FPV analysis provides useful metrics for many applications. To illustrate, the more steps a walking robot takes before failure, the more stable it is said to be. Once the performance is quantified, the control can be optimized.

Control action comes into play in two ways: Low-level and high-level. For the Europe tour, say the probability for city change is directly proportional to population to the power k, e.g.,

$$\text{Probability of staying in Madrid} = \frac{(\text{Population of Madird})^k}{(\text{Population of Madird})^k + (\text{Population of Paris})^k}, \tag{A.51}$$

where $k \in \{1, 2, 3\}$. This means a Markov Decision Process with three control actions. Previous analysis was a special case of this setting with $k = 1$ (see (A.1)). Any choice of k gives a Markov Chain, for which FPV is calculated as shown. Choosing a k or a set of k values for the whole system is the low-level control problem we discuss in Chapter 4. Moreover, if multiple k values are available, deciding on which k to use for a given city is the high-level control problem, which we tackle in Chapter 5.

A.6 Applications

A.6.1 Coin Toss

Consider tossing an unfair coin, for which the probability of having tails is p. As illustrated in Figure 2.5, when the number of flips before two heads in a row is of interest, three states are possible: (1) Heads-heads, (2) Tails in the last flip (including 'not-flipped yet'), (3) Tails-Heads (including 'flipped once and it was heads'). When $p = 0.01$, the system-wide MFPT is $M \approx 10,099$ and the memory constant is 1.0001×10^{-4}. The MFPT vector and the metastable distributions are given by

$$\mathbf{m} \approx \begin{bmatrix} 0 \\ 10,100 \\ 10,000 \end{bmatrix} \text{ and } \boldsymbol{\phi} \approx \begin{bmatrix} 0 \\ 0.9901 \\ 0.0099 \end{bmatrix} \tag{A.52}$$

So, if the initial state is x_2, $10,100$ flips are expected before two heads in a row.

A.6.2 Epidemics

For the susceptible-infected-susceptible (SIS) model explained in [Ahn and Hassibi, 2013], the number of discrete time steps to everyone being healthy can be calculated. As a toy example, consider a network of only 2 people with no birth or death. Each person

is either susceptible or infected, so four states are possible as listed in Table A.2. Note that when both patients are susceptible (State 1), the state does not change, because noone can become infected.

	State 1	State 2	State 3	State 4
Patient 1	Susceptible	Susceptible	Infected	Infected
Patient 2	Susceptible	Infected	Susceptible	Infected

Table A.2: Possible states for SIS model of epidemics with 2 people

Let 'the probability of recovery when a node is infected' be $\delta = 0.01$, and 'the probability to be infected when the other node is infected' be $\beta = 0.8$. Then, the stochastic matrix is given by

$$
\boldsymbol{T} = \begin{bmatrix}
1 & 0 & 0 & 0 \\
(1-\beta)\delta & (1-\delta)(1-\beta) & \beta\delta & \beta(1-\delta) \\
(1-\beta)\delta & \beta\delta & (1-\delta)(1-\beta) & \beta(1-\delta) \\
\delta\delta & \delta(1-\delta) & \delta(1-\delta) & (1-\delta)(1-\delta)
\end{bmatrix}
$$

$$
= \begin{bmatrix}
1 & 0 & 0 & 0 \\
0.002 & 0.198 & 0.008 & 0.792 \\
0.002 & 0.008 & 0.198 & 0.792 \\
0.001 & 0.0099 & 0.0099 & 0.9801
\end{bmatrix}.
$$

(A.53)

λ_2 is such that MFPT is $M = 6.8383 \times 10^3$. In addition, $\lambda_3 = 0.19$, and the memory

constant is 1.8×10^{-4}. The MFPT vector and the metastable distribution are given by

$$\mathbf{m} \approx \begin{bmatrix} 0 \\ 6822.7 \\ 6822.7 \\ 6838.7 \end{bmatrix} \text{ and } \boldsymbol{\phi} \approx \begin{bmatrix} 0 \\ 0.0122 \\ 0.0122 \\ 0.9757 \end{bmatrix}. \tag{A.54}$$

Small memory constant results in states having a MFPT close to either zero or M. It is interesting to see that with a high probability (0.9757), both people are infected during the epidemic while all healthy state is the stable one.

Estimating survival times of epidemic spreads can potentially be useful for public health research to optimize actions while minimizing deaths and expenditures.

A.6.3   Driving a Car

Arguably, given enough time (millions of years if necessary), any driver will be involved in an accident. The same is true for autonomous cars including the Google car. The expected miles driven between accidents can be estimated to quantify and increase the safety.

A.6.4   Queueing and Polling Systems - Traffic Intersection

Queueing theory deals with waiting lines and queues. One application of polling systems, which are extensions of queueing systems, is traffic intersections with multiple lines as illustrated in [Miculescu and Karaman, 2014]. As a toy example, consider the intersection with two lines shown in Figure A.2. The goal of the traffic light of the intersection is to avoid traffic jam, which is defined as having more than 4 cars in a lane. Assume that each turn a single car may pass through the intersection and new cars come stochastically to each line. Let the number of cars arriving at each lane have Poisson distribution with

parameter $\lambda = 0.1$. This intersection can be easily treated as a Markov Decision Process. If the controller always allows the same line to proceed, the expected discrete-time to traffic jam is around 10. The exhaustive policy allows a line to proceed until that line is empty and then switches to the other lane. This policy results with 1.09×10^6 turns before traffic jam.
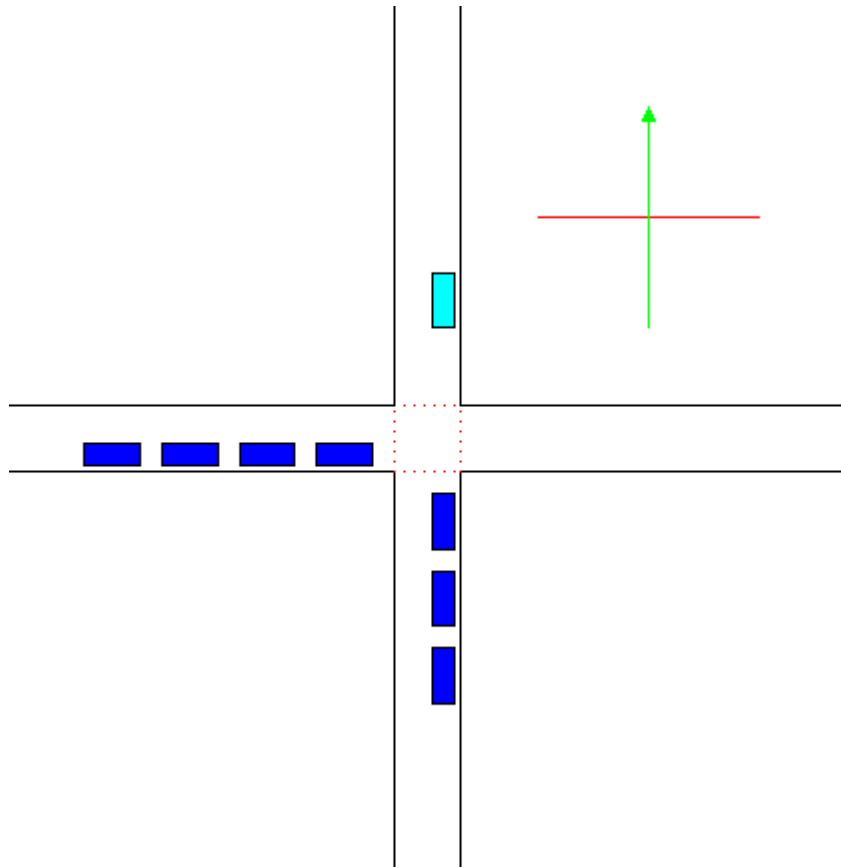

Figure A.2: An intersection with two lanes. Cars are either going from west to east or south to north. Blue cars are waiting to pass through the intersection. Cyan colored car recently moved to the north side of the intersection. The arrow shows which lane is allowed to proceed. In this toy example, traffic jam corresponds to 5 or more cars in a lane. The goal of the traffic lights is to minimize the traffic jam rates. Each turn a single car may pass through the intersection and new cars come stochastically to each line. The number of cars arriving at each lane has Poisson distribution with parameter $\lambda = 0.1$. This intersection can be easily treated as a Markov Decision Process.

A.7   Conclusion

This appendix studied first passage time, which is a survival metric. It presented system-wide mean first passage time (MFPT), which is calculated using the second largest eigenvalue of the stochastic transition matrix. The chapter also illustrated that for metastable systems, system-wide MFPT is an accurate indicator across a large set of states of those frequently visited. Then mean first passage value (MFPV) was introduced, which gives a more general value of interest, such as energy expenditure, distance, or time. Bounds on first passage value (FPV) was provided for a given confidence level. The chapter also showed how these tools explained can be used to low-level and high-level control hybrid systems.

Appendix B

Biped Model

The methods of this paper are appropriate and useful for various systems. To show applicability to high degree of freedom (DOF) robots (compared to 2-link walker in [Byl and Tedrake, 2009] and 3-link walker of [Chen and Byl, 2012]), the analysis in this thesis is carried out with the 5-link biped shown in Figure B.1. The model is based on the RABBIT robot shown in Figure 1.4c [Chevallereau et al., 2003].

RABBIT has point feet, 5 degrees-of-freedom (DOF) and four actuators located at the internal joints. Since the robot cannot produce ankle torques, it is underactuated by 1 DOF. While studying RABBIT, we restrict our attention to planar motion and assume links are rigid. The angles shown in the figure form $q := [q_1 \quad q_2 \quad q_3 \quad q_4 \quad q_5]^T$, the ten dimensional state of the robot is defined as $x := [q^T \quad \dot{q}^T]^T$, and sh denotes the height of the swing foot. The model parameters are taken from RABBIT [Westervelt et al., 2007] and listed in Table B.1.

Depending on the number of legs in contact with the ground, the robot is either in the single or double support phase. Walking consists of these two phases in sequence. The single support (swing) phase has continuous dynamics. Using a Lagrangian approach, the

Table B.1: Model parameters for the five-link robot based on RABBIT [Westervelt et al., 2007]

| Description	Parameter Label	Value
Torso Mass	m_T	12 kg
Femur Mass	m_f	6.8 kg
Tip Mass	m_t	3.2 kg
Torso Inertia	I_T	1.33 kg m^2
Femur Inertia	I_f	0.47 kg m^2
Tip Inertia	I_t	0.20 kg m^2
Torso Length	l_T	0.63 m
Femur Length	l_f	0.4 m
Tip Length	l_t	0.4 m
Torso Mass Center	p_T	0.24 m
Femur Mass Center	p_f	0.11 m
Tip Mass Center	p_t	0.24 m
Gravitational Acceleration	g_0	9.81 m/s^2
Gear Ratio	n_g	50
Ground Friction Coefficient	μ_s	0.6
Saturation Limit	u_{sat}	50 Nm
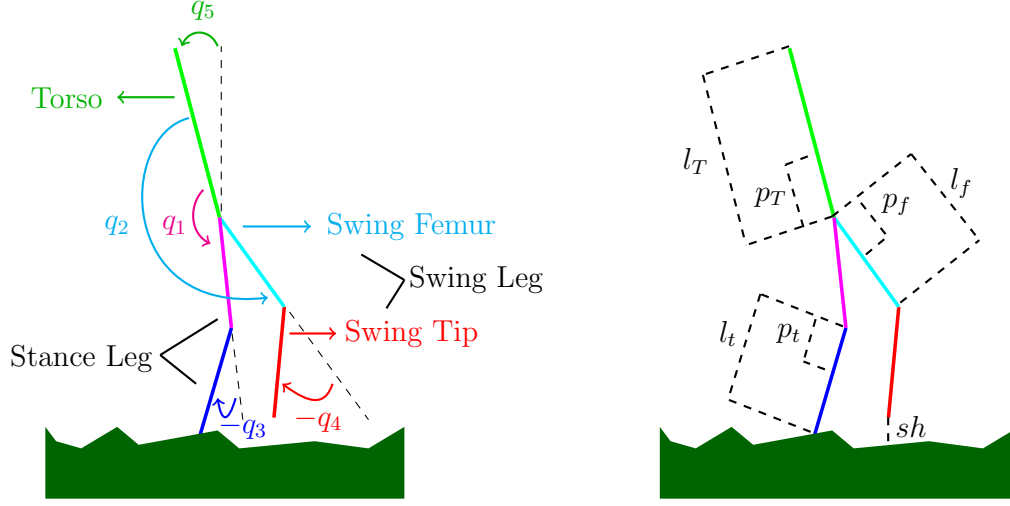
Figure B.1: Illustration of the five-link robot with identical legs that is used as our biped model in this thesis. This model is based on RABBIT shown in Figure 1.4c.

equations of motion can be derived in the canonical form of

$$D(q)\ddot{q} + C(q,\dot{q})\dot{q} + G(q) = Bu, \tag{B.1}$$

where u is the input. An important point is that q consists of the five angles depicted in Fig. B.1 whereas u has only four elements. The system has this degree of underactuation because of the passive joint at the stance tip. The swing dynamics can be equivalently expressed as

$$\dot{x} = \begin{bmatrix} \dot{q} \\ D^{-1}(-C\dot{q} - G + Bu) \end{bmatrix} =: f(x) + g(x)u. \tag{B.2}$$

During the swing phase of a successful step, the swing leg takes off from the ground, passes the stance leg and lands on a further point on the ground. So, each single support phase starts and ends with double support phases. As the robot has point feet, the double support (stance) phase can be well captured as an instantaneous impact event. The robot experiences this impact whenever the swing foot hits the ground ($sh = 0$) from above

$(\dot{s}h < 0)$. Let us denote this impact surface, aka the jump set, by S. Then we have

$$x^+ = \Delta(x^-) := \begin{bmatrix} \Delta_q \, q^- \\ \Delta_{\dot{q}}(q^-) \, \dot{q}^- \end{bmatrix} \qquad x \in S, \tag{B.3}$$

where $x^- = [(q^-)^T \ (\dot{q}^-)^T]^T$ and x^+ are the states just before and after the impact respectively. Conservation of energy and the principle of virtual work gives the mapping Δ [Westervelt et al., 2007], [Hurmuzlu and Marghitu, 1994]. Essentially, this model assumes instantaneous, inelastic collisions between the swing leg tip and the ground, with instantaneous changes in velocities to reflect the effects of impulsive forces exerted on the robot.

Although the robot's position and orientation do not actually change according to the impact model, we relabel the legs every step, so the previous swing leg becomes the new stance leg and vice versa. So, Δ_q is such that we have $\Delta_q[q_1 \ \ q_2 \ \ q_3 \ \ q_4 \ \ q_5]^T = [q_2 \ \ q_1 \ \ q_4 \ \ q_3 \ \ q_5]^T$. Without relabeling, a periodic walking gait would have two steps as its period.

Since a step consists of a single support phase and an impact event, it has hybrid dynamics as illustrated in Figure B.2. In our modeling, we assume the impact event occurs first, but the order in the definition of a step is an arbitrary choice, so long as one remains consistent after deciding. As seen in Figure B.2, for a step to be successful, certain "validity conditions" must be satisfied, which we list next. After impact, the former stance leg must lift from ground with no further interaction with the ground until the next impact. Also, the swing foot must have progressed past the stance foot before the impact of the next step occurs. Only the feet should contact the ground. Furthermore, the force on the stance tip during the swing phase, and the force on the swing tip at the impact should satisfy the friction constraint given by

$$F_{friction} = F_{normal} \, \mu_s > |F_{transversal}|. \tag{B.4}$$

If validity conditions are not met, the step is labeled as "unsuccessful" and the system is modeled as transitioning to a failure state. This is a conservative model, because in reality violating these conditions does not necessarily mean failure.
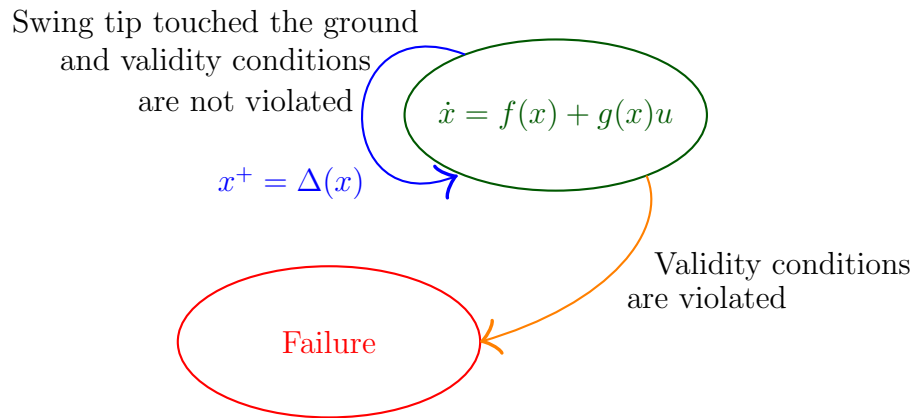

Figure B.2: Hybrid model of a step and the failure state. Swing phase is governed by continuous dynamics or flows, which are interrupted by discontinuous impacts.
Image inspired by [Westervelt et al., 2007].

91

Appendix C

Modeling Rough Terrain

To study rough terrain walking, the methodology in Chapter 2 assumes stochastically changing terrain, which requires modeling ground with finitely many dimensions. Two most elementary models, which are only one dimensional disturbances to the robot, are presented in Figure C.1. This thesis mainly assumes sloped terrain model, but results when heights are varying instead are also presented in Section 4.3.
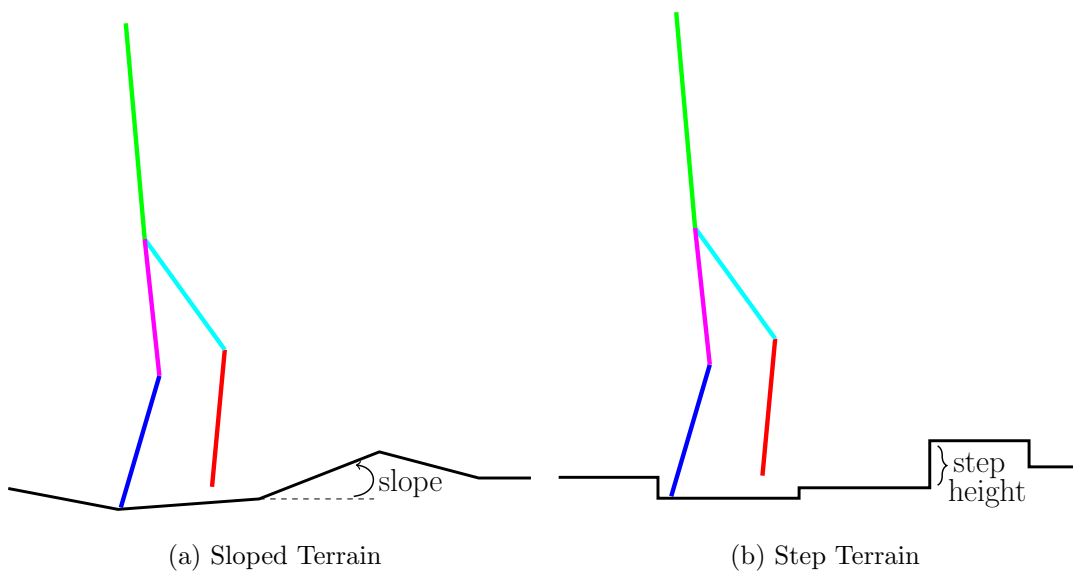

(a) Sloped Terrain   (b) Step Terrain

Figure C.1: One dimensional terrain disturbances

A natural concern is related to the validity of these terrain models. Consider the higher dimensional terrain disturbance in Figure C.2. Red dashed line shows the trajectory of the swing foot for a specific initial condition and the controller employed. Given this trajectory, all three terrains shown on the right hand side of Figure C.2 are equivalent to the original terrain. In particular, the terrain in the right bottom is generated with *double-sloped* terrain model. In addition to the sloped terrain of Figure C.1a, this model has an extra dimension which stores the slope experienced at impact. Adopting double-sloped terrain is a topic of future work.
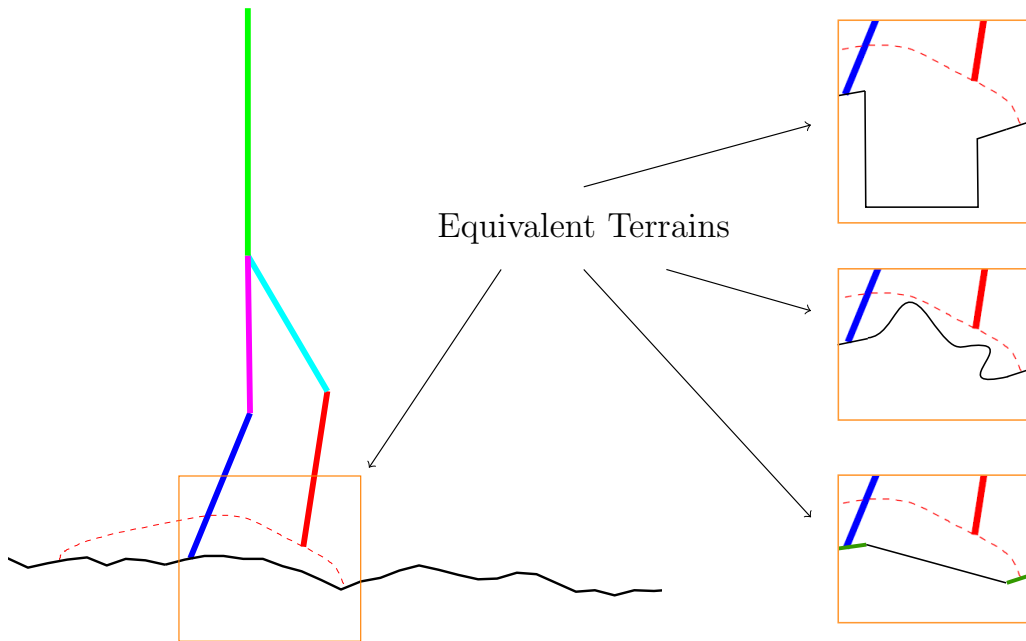

Figure C.2: Higher dimensional terrain disturbances

Appendix D

Extended Hybrid Zero Dynamics

Any one of the numerous control schemes proposed for bipedal locomotion can be optimized and benchmarked using the methods presented in this thesis. As case demonstration, we illustrate our results mainly on the extended hybrid zero dynamics framework explained in this Appendix.

In the literature of bipedal locomotion control, typically time trajectories are imposed to achieve a desired walking motion. However, time-invariant controllers have critical advantages over their time-varying counterparts. For example, imagine someone holding the robot in the mid-step for a second. After released, instead of hurrying to catch up the time trajectories for re-synchronization, the robot better continue the interrupted motion. For this reason, defining an internal clock which defines how far the robot is at a step is a meaningful approach, which has led to the hybrid zero dynamics (HZD) framework [Westervelt et al., 2003]. The controller scheme introduced in this thesis is a generalization of the now-famous HZD control in two-ways. First, we modify it for non-flat terrain as in [Yadukumar et al., 2012] and [Saglam and Byl, 2015]. Secondly, and much more importantly, HZD controllers assume deterministic terrain by design, where the internal clock ticks from 0 to 1 at every step. In this thesis, we extend the

94

trajectories to cover from 0 to 1.4, thus the extended hybrid zero dynamics (EHZD). The start and end points were empirically chosen and can be extended further in both ways when necessary. Finally, we use B-splines instead of Bézier polynomials just as a design choice. For optimization and benchmark results of this strategy along with the original HZD controller and a piecewise reference trajectories using a sliding mode control, see Chapter 4.

D.1 The Structure

First, we choose a phase-variable which will work as an internal-clock. The phase should be monotonic through the step, e.g., hip location moves forward with an almost constant velocity in humans [Ames, 2012]. As in [Westervelt et al., 2007], we choose θ shown in Figure D.1 as our phase variable, which corresponds $\theta = cq$ with $c = [-1\ 0\ -1/2\ 0\ -1]$ since femur and tip lengths are equal in RABBIT robot.
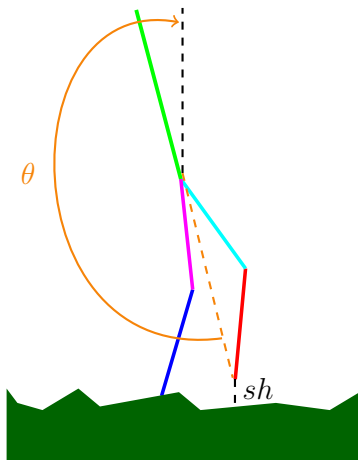

Figure D.1: Phase θ and swing tip height sh. Since femur and tip lengths are equal in RABBIT robot, $\theta = cq$ with $c = [-1\ 0\ -1/2\ 0\ -1]$. The robot experiences an impact whenever $sh = 0$ and $\dot{sh} < 0$, i.e., swing tip hits the ground from above.

Second, we decide on four independent variables to control h_0 because the robot has four actuators only. It is intuitive to control the relative (internal) angles, i.e., $h_0 := [q_1 \ q_2 \ q_2 \ q_3 \ q_4]^T$. Then h_0 is in the form of $h_0 = \mathrm{H}_0 \, q$, where $\mathrm{H}_0 = [\mathrm{I}_4 \ 0]$. Changing h_0 later is an easy step in this framework and it does not affect the performance to the author's experience.

Third, let $h_d(\theta)$ be the references for h_0. Then the tracking error is given by

$$h(q) := h_0(q) - h_d(\theta) = \mathrm{H}_0 q - h_d(cq). \tag{D.1}$$

Taking the first derivative with respect to time yields

$$\dot{h} = \frac{\partial h}{\partial x}\dot{x} = \frac{\partial h}{\partial x}f(x) =: \mathcal{L}_f h = \langle \nabla h, f \rangle, \tag{D.2}$$

where we used the fact that $\dfrac{\partial h}{\partial x}g(x) = 0$. For the clarity of later equations, we will use the Lie derivative ($\mathcal{L}$) notation. Then, we have

$$\ddot{h} = \mathcal{L}_f^2 h + \mathcal{L}_g \mathcal{L}_f h \ u. \tag{D.3}$$

Substituting the linearizing controller structure

$$u = (\mathcal{L}_g \mathcal{L}_f h)^{-1}(-\mathcal{L}_f^2 h + v) \tag{D.4}$$

to (D.3) yields

$$\ddot{h} = v. \tag{D.5}$$

There are various methods to design v in (D.4) to force h (and $\dot{h}$) to zero [Ames et al., 2012]. While even a PD controller could be sufficient, a sliding mode control (SMC) is preferable, due to its finite time convergence [Sabanovic and Ohnishi, 2011], which we summarize next.

D.2   Sliding Mode Control

Remember that h corresponds to tracking error. The generalized error is defined as

$$\sigma_i = \dot{h}_i + h_i/\tau_i, \quad i = \{1, 2, 3, 4\}, \tag{D.6}$$

where τ_is are time constants for h_i. Note that when the generalized error is driven to zero, i.e. $\sigma_i = 0$, we have

$$0 = \dot{h}_i + h_i/\tau_i. \tag{D.7}$$

The solution to this equation is given by

$$h_i(t) = h_i(t_0) \ exp(-(t - t_0)/\tau_i), \tag{D.8}$$

which drives h_i to 0 exponentially fast. Finally, v in (D.4) is given by

$$v_i = -k_i|\sigma_i|^{2\alpha_i - 1} sign(\sigma_i), \quad i = \{1, 2, 3, 4\}, \tag{D.9}$$

where $k_i > 0$ and $0.5 < \alpha_i < 1$ are called the convergence coefficient and convergence exponent respectively. Note that if we had $\alpha_i = 1$, this would simply be a standard PD controller. Then, k_i/τ_i and k_i are analogous to the proportional and derivative gains of a PD controller. However, $0.5 < \alpha_i < 1$ ensures finite time convergence. In this thesis we used $\alpha_i = 0.75$, $\tau_i = 0.1$, $k_i = 10$ for all controllers, but h_d was different for each low-level controller.

What the controller does is driving the system to the "zero dynamics manifold", noted by $\mathcal{Z}$, where $h = 0$ and $\dot{h} = 0$. The following two sections consider the dynamics on this manifold. The final goal is to design h_d such that the desired walking motion is generated.

D.3   Swing Phase Zero Dynamics

Let V be the potential energy of the robot, $\gamma_0(q)$ be the last row of D and define
$\gamma := \gamma_0 \dot{q}$. Then, $\mathcal{L}_g \gamma = 0$ and $\mathcal{L}_f \gamma = -\left.\dfrac{\partial V}{\partial q_5}\right|_{\mathcal{Z}}$. For $x \in \mathcal{Z}$ we transform coordinates by

$$\xi_1 = \theta, \qquad \xi_2 = \gamma, \tag{D.10}$$

to equivalently express the system dynamics during the swing phase as

$$\dot{\xi}_1 = c\dot{q}, \qquad \dot{\xi}_2 = \mathcal{L}_f \gamma, \tag{D.11}$$

where the right-hand sides are evaluated at

$$q = \mathrm{H}^{-1} \begin{bmatrix} h_d \\ \xi_1 \end{bmatrix} \qquad (\text{because } \xi_1 = \theta = cq \text{ and } \mathrm{H}_0 q = h_0 = h_d \text{ for } x \in \mathcal{Z}),$$
$$\tag{D.12}$$

and $\dot{q} = \begin{bmatrix} \dfrac{\partial h}{\partial q} \\ \gamma_0 \end{bmatrix}^{-1} \begin{bmatrix} 0 \\ \xi_2 \end{bmatrix} \qquad (\text{because } \dot{h} = 0 \text{ for } x \in \mathcal{Z} \text{ and } \xi_2 = \gamma = \gamma_0 \dot{q}).$

To evaluate $\dot{q}$, we can alternatively differentiate q from above to get

$$\dot{q} = \mathrm{H}^{-1} \begin{bmatrix} \dfrac{\partial h_d}{\partial \theta} \\ 1 \end{bmatrix} \dot{\theta} \tag{D.13}$$

Using (D.12) we can write (D.11) as

$$\dot{\xi}_1 = \kappa_1(\xi_1)\xi_2, \qquad \dot{\xi}_2 = \kappa_2(\xi_1). \tag{D.14}$$

D.4 Hybrid Zero Dynamics Impact

As we will see, h_d will be designed such that $x^- \in \mathcal{Z}$ implies $x^+ \in \mathcal{Z}$. Now assume the swing foot passed the stance foot and had an impact. Let q_0^- denote the angles just before the impact on h_d. Then, q_0^- is a solution to

$$
\begin{bmatrix} h(q) \\ sh \end{bmatrix} = 0,
\tag{D.15}
$$

where sh is the swing tip height as drawn in Figure D.1. At the impact, the angles are relabeled as in (B.3). So, after the impact we have $q_0^+ = \Delta_q q_0^-$. The phases at the beginning and end of the step are simply $\theta^+ := c q_0^+$ and $\theta^- := c q_0^-$ respectively.

Similarly let $\dot{q}_0^-$ and $\dot{q}_0^+$ denote the velocities just before and after the impact respectively. ξ_2^- and ξ_2^+ are the corresponding ξ_2 values. Then, using (D.12) we get

$$
\dot{q}_0^- = \begin{bmatrix} \dfrac{\partial h}{\partial q}(q_0^-) \\ \gamma_0(q_0^-) \end{bmatrix}^{-1} \begin{bmatrix} 0 \\ 1 \end{bmatrix} \xi_2^- =: \overline{\lambda}_{\dot{q}} \, \xi_2^-
\tag{D.16}
$$

From (B.3), we obtain $\dot{q}_0^+ = \Delta_{\dot{q}}(q_0^-) \, \dot{q}_0^-$ and $\xi_2^+ = \gamma_0(q_0^+) \, \dot{q}_0^+$. Defining

$$
\delta_{\text{zero}} := \gamma_0(q_0^+) \, \Delta_{\dot{q}}(q_0^-) \, \overline{\lambda}_{\dot{q}},
\tag{D.17}
$$

the impact map on zero dynamics manifold is given by

$$
\xi_1^+ = \theta^+, \qquad \xi_2^+ = \delta_{\text{zero}} \, \xi_2^-.
\tag{D.18}
$$

D.5 Poincaré Analysis

We then define a Poincaré section just before the impact. We already know the angles are q_0^-. To find the fixed point on this Poincré map (if it exists), we also need a fixed

ξ_2^-. Define $\xi_{2b} := \xi_2^2/2$. ξ_{2b}^+ and ξ_{2b}^- denote its value at the beginning and end of the step respectively. Then, we have

$$\frac{d\xi_{2b}}{d\xi_1} = \frac{\kappa_2(\xi_1)}{\kappa_1(\xi_1)}. \tag{D.19}$$

Integration over a step gives

$$\xi_{2b}^- - \xi_{2b}^+ = \int_{\theta^+}^{\theta^-} \frac{\kappa_2(\xi_1)}{\kappa_1(\xi_1)} d\xi_1. \tag{D.20}$$

Since impact maps ξ_{2b} to $\delta_{\text{zero}}^2 \xi_{2b}$, the fixed point ξ_{2b}^* is obtained by solving

$$\xi_{2b}^* - \delta_{\text{zero}}^2 \xi_{2b}^* = \int_{\theta^+}^{\theta^-} \frac{\kappa_2(\xi_1)}{\kappa_1(\xi_1)} d\xi_1. \tag{D.21}$$

Then, the fixed points for the zero dynamics are

$$\xi_1^* = \theta^-, \qquad \xi_2^* = \sqrt{\frac{-2}{1 - \delta_{\text{zero}}^2} \int_{\theta^+}^{\theta^-} \frac{\kappa_2(\xi_1)}{\kappa_1(\xi_1)} d\xi_1}. \tag{D.22}$$

D.6 Under deterministic conditions

[Westervelt et al., 2007] carries a Poincaré analysis, where the stability is formulated analytically and shown numerically. Using the fixed point as initial condition, they simulate the 2D dynamics described in (D.11) until $\theta = \theta^-$ and calculate the steady-state cost of transport (COT) defined in (4.1). However, we demonstrate in Figure 4.1 that optimizing for energy efficiency results in sensitivity to perturbations, thus poor performance on rough terrain.

During optimization, [Westervelt et al., 2003] impose many constraints such as friction violations and torque saturation limits. On the other hand, our method deals with stochastic conditions to maximize global stability and no constraints are necessary for optimization because it considers the full dynamics where, for example, the controller can hit the saturation limit.

D.7   Reference Design

While forming trajectories in phase instead of time, we first scale and shift θ to have

an internal clock which ticks from 0 to 1 on the limit cycle using

$$\tau(q) := \frac{\theta(q) - \theta^+}{\theta^- - \theta^+}. \tag{D.23}$$

Then, the reference trajectory is determined as

$$h_d(\theta) := \begin{bmatrix} b_1(\tau) \\ b_2(\tau) \\ b_3(\tau) \\ b_4(\tau) \end{bmatrix}. \tag{D.24}$$

To form trajectories defined by $b_j(\tau)$s, we use B-splines as formulated in [Patrikalakis

and Maekawa, 2010]. Each of the four trajectories is then defined as a linear combination

of control points α_i^j and B-spline basis functions $N_{i,k}(\tau)$ given by

$$b_j(\tau) = \sum_{i=0}^{n} \alpha_i^j N_{i,k}(\tau), \qquad n \geq k - 1, \qquad \tau \in [\tau_{k-1}, \tau_{n+1}], \tag{D.25}$$

where k is order of the curve and the number of control points equals $n + 1$. The basis

functions $N_{i,k}(\tau)$ are uniquely determined by the knot vector

$$\boldsymbol{T} = \left(\tau_0, \tau_1, ..., \tau_{k-1}, \tau_k, \tau_{k+1}, ..., \tau_{n-1}, \tau_n, \tau_{n+1}, ..., \tau_{n+k}\right), \tag{D.26}$$

which consist of $n + k + 1$ elements. We use 4th order curves on the knot vector

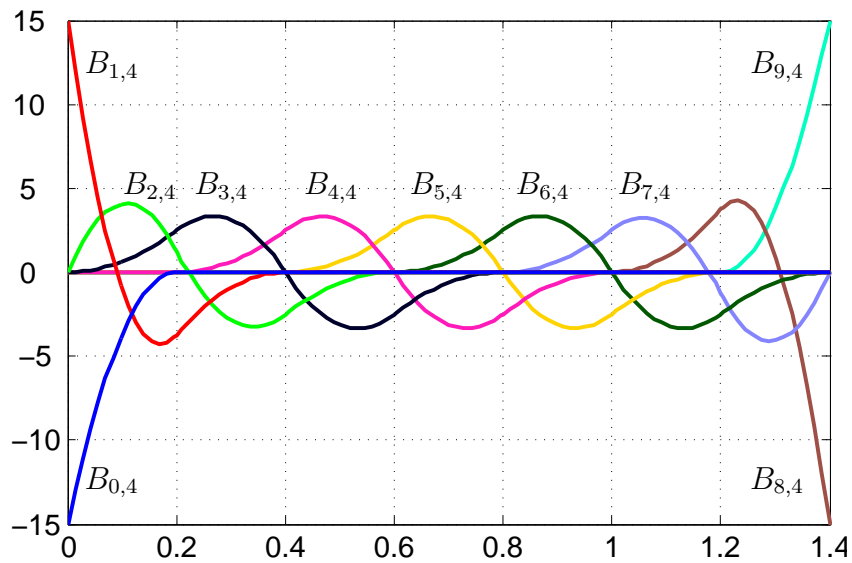$$\boldsymbol{T} = (0, 0, 0, 0, 0.2, 0.4, 0.6, 0.8, 1, 1.2, 1.4, 1.4, 1.4, 1.4). \tag{D.27}$$

The resulting 10 basis functions and their derivatives are pictured in Figure D.2.

10 basis functions imply 10 control points for each of the 4 $b_j(\tau)$s. So, $10 \times 4 = 40$

α_i^j parameters need to be optimized. However, we demand hybrid invariance, so $x^- \in \mathcal{Z}$
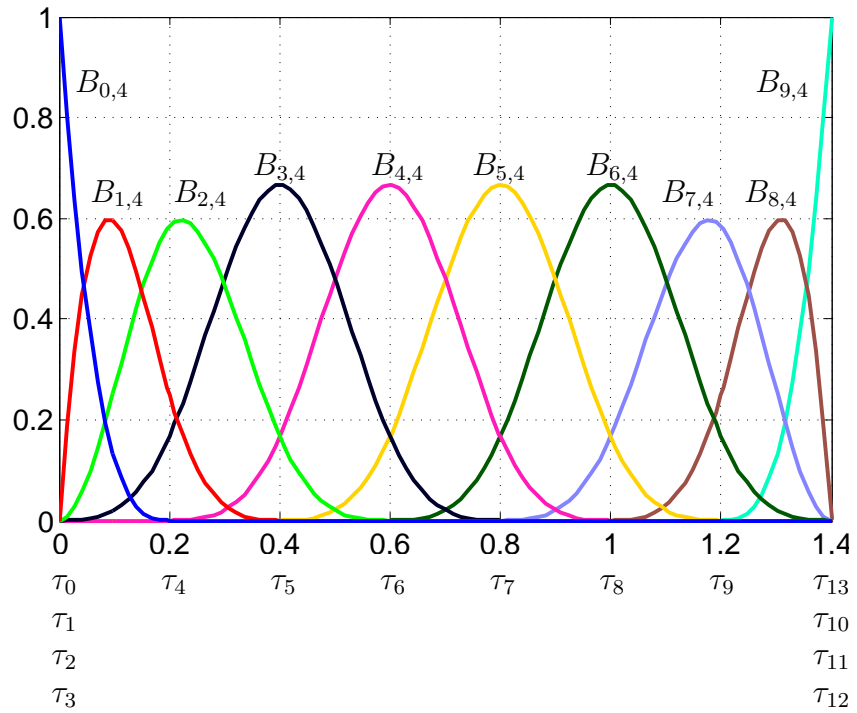
(a) Basis functions

(b) Derivatives of basis functions

Figure D.2: 10 basis functions of order 4 with uniform knot vector in (D.27) and their derivatives. On the limit cycle, the internal clock ticks from $\tau = 0$ to $\tau = 1$. We extend the knots until $\tau = 1.4$ for impacts on uneven terrain.

on the limit cycle should imply $x^+ \in \mathcal{Z}$, i.e., once the walker is on the zero dynamics manifold it should stay there under deterministic conditions. Hybrid invariance constraint eliminates $2 \times 4 = 8$ of the 40 parameters. This is achieved by calculating α_0^j and α_1^j in terms of the other α_i^j values.

First, assume $h = 0$ at the impact when $\tau = 1$. Note that $h_d|_{\tau=1}$ is independent from α_0^j and α_1^j (see Figure D.2a). Also $h_d|_{\tau=0}$ is a function of α_0^j only. Achieving $h = 0$ after the impact requires

$$q_0^+ = \Delta_q q_0^-$$

$$H^{-1} \begin{bmatrix} h_d|_{\tau=0} \\ \theta^+ \end{bmatrix} = \Delta_q H^{-1} \begin{bmatrix} h_d|_{\tau=1} \\ \theta^- \end{bmatrix} \tag{D.28}$$

$$\begin{bmatrix} h_d|_{\tau=0} \\ \theta^+ \end{bmatrix} = H \Delta_q H^{-1} \begin{bmatrix} h_d|_{\tau=1} \\ \theta^- \end{bmatrix},$$

which determines α_0^j.

Second, assume $\dot{h} = 0$ at the impact with $\tau = 1$. Again, $\left. \dfrac{\partial h_d}{\partial \theta} \right|_{\tau=0}$ is independent from α_0^j and α_1^j. Also $\left. \dfrac{\partial h_d}{\partial \theta} \right|_{\tau=1}$ is a function of these two (see Figure D.2b), one which we already determined above. Now remember (D.13). Achieving $\dot{h} = 0$ after the impact means

$$\dot{q}_0^+ = \Delta_{\dot{q}}(q_0^-) \, \dot{q}_0^-, \tag{D.29}$$

or equivalently

$$H^{-1} \begin{bmatrix} \left. \dfrac{\partial h_d}{\partial \theta} \right|_{\tau=0} \\ 1 \end{bmatrix} \dot{\theta}^+ = \Delta_{\dot{q}}(q_0^-) \, H^{-1} \begin{bmatrix} \left. \dfrac{\partial h_d}{\partial \theta} \right|_{\tau=1} \\ 1 \end{bmatrix} \dot{\theta}^-, \tag{D.30}$$

from which we calculate α_1^j. As a result, 32 α_i^j parameters that need to be optimized are given by $i \in \{2, 3, 4, 5, 6, 7, 8, 9\}$ and $j \in \{1, 2, 3, 4\}$. For optimization and benchmark results of this controller scheme see Chapter 4.

Bibliography

[Abbel, 2012] Abbel, P. (2012). Discretization. In *CS 287: Advanced Robotics Lecture Notes*. Accessed: 2015-05-06. Available from: http://www.cs.berkeley.edu/~pabbeel/ cs287-fa12/slides/discretization.pdf.

[Ahn and Hassibi, 2013] Ahn, H. J. and Hassibi, B. (2013). Global dynamics of epidemic spread over complex networks. In *2013 IEEE 52nd Annual Conference on Decision and Control (CDC)*, pages 4579–4585.

[Ames et al., 2012] Ames, A., Galloway, K., and Grizzle, J. (2012). Control lyapunov functions and hybrid zero dynamics. In *2012 IEEE 51st Annual Conference on Decision and Control (CDC)*, pages 6837–6842.

[Ames, 2012] Ames, A. D. (2012). First Steps toward Automatically Generating Bipedal Robotic Walking from Human Data. In *Robot Motion and Control 2011*, number 422 in Lecture Notes in Control and Information Sciences, pages 89–116. Springer London. Available from: http://link.springer.com/chapter/10.1007/978-1-4471-2343-9_8.

[Belle, 2008] Belle, G. v. (2008). *Statistical Rules of Thumb*. Wiley-Interscience, Hoboken, N.J, 2nd edition edition.

[Bellman, 1957] Bellman, R. (1957). A Markovian decision process. *Indiana University Mathematics Journal*, 6(4):679–684. Available from: http://www.iumj.indiana.edu/ IUMJ/FULLTEXT/1957/6/56038.

[Benallegue and Laumond, 2013] Benallegue, M. and Laumond, J.-P. (2013). Metastability for High-Dimensional Walking Systems on Stochastically Rough Terrain. In *Robotics: Science and Systems*.

[Bhounsule, 2014] Bhounsule, P. A. (2014). Numerical accuracy of two benchmark models of walking: the rimless spoked wheel and the simplest walker. *Dynamics of Continuous, Discrete and Impulsive Systems Series B: Applications and Algorithms*, 21:137–148. Available from: http://engineering.utsa.edu/~pab/pdw_benchmark.pdf.

[Bhounsule et al., 2014] Bhounsule, P. A., Cortell, J., Grewal, A., Hendriksen, B., Karssen, J. G. D., Paul, C., and Ruina, A. (2014). Low-bandwidth reflex-based

control for lower power walking: 65 km on a single battery charge. *The International Journal of Robotics Research*, page 0278364914527485. Available from: http://ijr.sagepub.com/content/early/2014/06/12/0278364914527485.

[Brown, 1914] Brown, T. G. (1914). On the nature of the fundamental activity of the nervous centres; together with an analysis of the conditioning of rhythmic activity in progression, and a theory of the evolution of function in the nervous system. *The Journal of Physiology*, 48(1):18–46. Available from: http://www.ncbi.nlm.nih.gov/pmc/articles/PMC1420503/.

[Byl, 2008] Byl, K. (2008). *Metastable Legged-Robot Locomotion*. PhD thesis, Massachusetts Institute of Technology.

[Byl and Tedrake, 2009] Byl, K. and Tedrake, R. (2009). Metastable Walking Machines. *The International Journal of Robotics Research*, 28(8):1040–1064. Available from: http://ijr.sagepub.com/cgi/doi/10.1177/0278364909340446.

[Chen and Byl, 2012] Chen, M.-Y. and Byl, K. (2012). Analysis and control techniques for the compass gait with a torso walking on stochastically rough terrain. In *American Control Conference (ACC), 2012*, pages 3451–3458. Available from: http://ieeexplore.ieee.org/xpls/abs_all.jsp?arnumber=6315669.

[Chevallereau et al., 2003] Chevallereau, C., Abba, G., Aoustin, Y., Plestan, F., Westervelt, E., Canudas-de Wit, C., and Grizzle, J. (2003). RABBIT: a testbed for advanced control theory. *IEEE Control Systems*, 23(5):57–79.

[Collins and Ruina, 2005] Collins, S. and Ruina, A. (2005). A Bipedal Walking Robot with Efficient and Human-Like Gait. In *Proceedings of the 2005 IEEE International Conference on Robotics and Automation, 2005. ICRA 2005*, pages 1983–1988.

[Collins et al., 2005] Collins, S., Ruina, A., Tedrake, R., and Wisse, M. (2005). Efficient Bipedal Robots Based on Passive-Dynamic Walkers. *Science*, 307(5712):1082–1085. Available from: http://www.sciencemag.org/content/307/5712/1082.

[Collins et al., 2001] Collins, S. H., Wisse, M., and Ruina, A. (2001). A Three-Dimensional Passive-Dynamic Walking Robot with Two Legs and Knees. *The International Journal of Robotics Research*, 20(7):607–615. Available from: http://ijr.sagepub.com/content/20/7/607.

[Dai and Tedrake, 2013] Dai, H. and Tedrake, R. (2013). L2-gain optimization for robust bipedal walking on unknown terrain. In *IEEE International Conference on Robotics and Automation (ICRA)*, pages 3116–3123. Available from: http://ieeexplore.ieee.org/xpls/abs_all.jsp?arnumber=6631010.

[Donald et al., 1993] Donald, B., Xavier, P., Canny, J., and Reif, J. (1993). Kinodynamic Motion Planning. *J. ACM*, 40(5):1048–1066. Available from: http://doi.acm.org/10.1145/174147.174150.

[Fingelkurts and Fingelkurts, 2004] Fingelkurts, A. A. and Fingelkurts, A. A. (2004). Making complexity simpler: multivariability and metastability in the brain. *The International Journal of Neuroscience*, 114(7):843–862.

[Goebel et al., 2012] Goebel, R., Sanfelice, R. G., and Teel, A. R. (2012). *Hybrid Dynamical Systems: Modeling, Stability, and Robustness*. Princeton University Press.

[Goswami and Kallem, 2004] Goswami, A. and Kallem, V. (2004). Rate of change of angular momentum and balance maintenance of biped robots. In *2004 IEEE International Conference on Robotics and Automation, 2004. Proceedings. ICRA '04*, volume 4, pages 3785–3790 Vol.4.

[Griffin and Grizzle, 2015] Griffin, B. and Grizzle, J. (2015). Walking Gait Optimization for Accommodation of Unknown Terrain Height Variations. In *American Control Conference*. Submitted.

[Grizzle et al., 2009] Grizzle, J., Hurst, J., Morris, B., Park, H.-W., and Sreenath, K. (2009). MABEL, a new robotic bipedal walker and runner. In *American Control Conference*, pages 2030–2036.

[Hanggi et al., 1990] Hanggi, P., Talkner, P., and Borkovec, M. (1990). Reaction-rate theory: fifty years after Kramers. *Reviews of Modern Physics*, 62(2):251–341. Available from: http://link.aps.org/doi/10.1103/RevModPhys.62.251.

[Hobbelen and Wisse, 2007] Hobbelen, D. and Wisse, M. (2007). A Disturbance Rejection Measure for Limit Cycle Walkers: The Gait Sensitivity Norm. *IEEE Transactions on Robotics*, 23(6):1213–1224.

[Hodgins and Raibert, 1991] Hodgins, J. and Raibert, M. (1991). Adjusting step length for rough terrain locomotion. *IEEE Transactions on Robotics and Automation*, 7(3):289–298. Available from: http://ieeexplore.ieee.org/stamp/stamp.jsp?tp=&arnumber=88138.

[Hurmuzlu and Basdogan, 1994] Hurmuzlu, Y. and Basdogan, C. (1994). On the Measurement of Dynamic Stability of Human Locomotion. *Journal of Biomechanical Engineering*, 116(1):30–36. Available from: http://dx.doi.org/10.1115/1.2895701.

[Hurmuzlu and Marghitu, 1994] Hurmuzlu, Y. and Marghitu, D. (1994). Rigid Body Collisions of Planar Kinematic Chains With Multiple Contact Points. *The International Journal of Robotics Research*, 13(1):82–92. Available from: http://ijr.sagepub.com/cgi/doi/10.1177/027836499401300106.

[Hurst, 2015a] Hurst, J. (2015a). *ATRIAS Biped Project Page.* Accessed: 2015-05-06. Available from: http://mime.oregonstate.edu/research/drl/atrias/.

[Hurst, 2015b] Hurst, J. (2015b). *ATRIAS Robot: Tackles an Obstacle Course.* Accessed: 2015-05-06. Available from: https://www.youtube.com/watch?v=1CfHbBAv6vo.

[Kajita et al., 2003] Kajita, S., Kanehiro, F., Kaneko, K., Fujiwara, K., Harada, K., Yokoi, K., and Hirukawa, H. (2003). Resolved momentum control: humanoid motion planning based on the linear and angular momentum. In *2003 IEEE/RSJ International Conference on Intelligent Robots and Systems, 2003. (IROS 2003). Proceedings*, volume 2, pages 1644–1650 vol.2.

[Kampen, 2011] Kampen, N. (2011). *Stochastic Processes in Physics and Chemistry.* Elsevier.

[Kuo, 2002] Kuo, A. D. (2002). The relative roles of feedforward and feedback in the control of rhythmic movements. *Motor Control*, 6(2):129–145.

[Kuo, 2007] Kuo, A. D. (2007). Choosing your steps carefully. *Robotics & Automation Magazine, IEEE*, 14(2):18–29. Available from: http://ieeexplore.ieee.org/xpls/abs_all.jsp?arnumber=4264364.

[Lagarias et al., 1998] Lagarias, J. C., Reeds, J. A., Wright, M. H., and Wright, P. E. (1998). Convergence Properties of the Nelder-Mead Simplex Method in Low Dimensions. *SIAM Journal of Optimization*, 9:112–147.

[Larsen and Grier, 1997] Larsen, A. E. and Grier, D. G. (1997). Like-charge attractions in metastable colloidal crystallites. *Nature*, 385(6613):230–233. Available from: http://www.nature.com/nature/journal/v385/n6613/abs/385230a0.html.

[Matthews, 1995] Matthews, K. (1995). Number Theory Web. Available from: http://www.numbertheory.org/courses/MP274/markov.pdf.

[McGeer, 1990] McGeer, T. (1990). Passive Dynamic Walking. *The International Journal of Robotics Research*, 9(2):62–82. Available from: http://ijr.sagepub.com/cgi/doi/10.1177/027836499000900206.

[Meyer, 2000] Meyer, C. D. (2000). *Matrix Analysis and Applied Linear Algebra.* SIAM.

[Miculescu and Karaman, 2014] Miculescu, D. and Karaman, S. (2014). Polling-systems-based control of high-performance provably-safe autonomous intersections. In *2014 IEEE 53rd Annual Conference on Decision and Control (CDC)*, pages 1417–1423.

[Morimioto et al., 2003] Morimioto, J., Zeglin, G., and Atkeson, C. (2003). Minimax differential dynamic programming: application to a biped walking robot. In *SICE 2003 Annual Conference*, volume 3, pages 2310–2315 Vol.3.

[Muller et al., 1997] Muller, R., Talkner, P., and Reimann, P. (1997). Rates and mean first passage times. *Physica A: Statistical Mechanics and its Applications*, 247(14):338–356. Available from: http://www.sciencedirect.com/science/article/pii/S0378437197003907.

[Oldenhuis, 2009] Oldenhuis, R. (2009). minimize - File Exchange - MATLAB Central. Available from: http://www.mathworks.com/matlabcentral/fileexchange/24298-minimize.

[Orin et al., 2013] Orin, D. E., Goswami, A., and Lee, S.-H. (2013). Centroidal dynamics of a humanoid robot. *Autonomous Robots*, 35(2-3):161–176. Available from: http://link.springer.com/article/10.1007/s10514-013-9341-4.

[Park et al., 2013] Park, H.-W., Ramezani, A., and Grizzle, J. W. (2013). A finite-state machine for accommodating unexpected large ground-height variations in bipedal robot walking. *IEEE Transactions on Robotics*, 29(2):331–345. Available from: http://ieeexplore.ieee.org/xpls/abs_all.jsp?arnumber=6399609.

[Park et al., 2012] Park, H.-W., Sreenath, K., Ramezani, A., and Grizzle, J. (2012). Switching control design for accommodating large step-down disturbances in bipedal robot walking. In *2012 IEEE International Conference on Robotics and Automation (ICRA)*, pages 45–50.

[Patrikalakis and Maekawa, 2010] Patrikalakis, N. M. and Maekawa, T. (2010). *Shape Interrogation for Computer Aided Design and Manufacturing*. Springer Berlin Heidelberg, Berlin, Heidelberg. Available from: http://link.springer.com/10.1007/978-3-642-04074-0.

[Pratt et al., 2001] Pratt, J., Chew, C.-M., Torres, A., Dilworth, P., and Pratt, G. (2001). Virtual Model Control: An Intuitive Approach for Bipedal Locomotion. *The International Journal of Robotics Research*, 20(2):129–143. Available from: http://ijr.sagepub.com/content/20/2/129.

[Raibert et al., 2008] Raibert, M., Blankespoor, K., Nelson, G., Playter, R., and the Big-Dog Team (2008). Bigdog, the rough-terrain quadruped robot. In *Proceedings of the World Congress of the International Federation of Automatic Control*, pages 10823–10825. Available from: http://web.unair.ac.id/admin/file/f_7773_bigdog.pdf.

[Sabanovic and Ohnishi, 2011] Sabanovic, A. and Ohnishi, K. (2011). Motion Control Systems. John Wiley & Sons. Available from: http://onlinelibrary.wiley.com/doi/10.1002/9780470825754.fmatter/summary.

[Saglam and Byl, 2014a] Saglam, C. and Byl, K. (2014a). Metastable Markov chains. In *2014 IEEE 53rd Annual Conference on Decision and Control (CDC)*, pages 2979–2985. Available from: http://ieeexplore.ieee.org/xpl/articleDetails.jsp?arnumber=7039847.

[Saglam and Byl, 2014b] Saglam, C. and Byl, K. (2014b). Quantifying the trade-offs between stability versus energy use for underactuated biped walking. In *2014 IEEE/RSJ International Conference on Intelligent Robots and Systems (IROS 2014)*, pages 2550–2557. Available from: http://ieeexplore.ieee.org/xpl/articleDetails.jsp?arnumber=6942910.

[Saglam and Byl, 2013a] Saglam, C. O. and Byl, K. (2013a). Stability and gait transition of the five-link biped on stochastically rough terrain using a discrete set of sliding mode controllers. In *IEEE International Conference on Robotics and Automation (ICRA)*, pages 5675–5682. Available from: http://ieeexplore.ieee.org/stamp/stamp.jsp?tp=&arnumber=6631393.

[Saglam and Byl, 2013b] Saglam, C. O. and Byl, K. (2013b). Switching policies for metastable walking. In *Proc. of IEEE Conference on Decision and Control (CDC)*, pages 977–983. Available from: http://ieeexplore.ieee.org/xpls/abs_all.jsp?arnumber=6760009.

[Saglam and Byl, 2014c] Saglam, C. O. and Byl, K. (2014c). Robust Policies via Meshing for Metastable Rough Terrain Walking. In *Proceedings of Robotics: Science and Systems*, Berkeley, USA. Available from: http://www.roboticsproceedings.org/rss10/p49.html.

[Saglam and Byl, 2015] Saglam, C. O. and Byl, K. (2015). Meshing Hybrid Zero Dynamics for Rough Terrain Walking. In *IEEE International Conference on Robotics and Automation (ICRA)*.

[Saglam et al., 2014] Saglam, C. O., Teel, A., and Byl, K. (2014). Lyapunov-based versus Poincare Map Analysis of the Rimless Wheel. In *IEEE Conference on Decision and Control (CDC)*. Available from: http://ieeexplore.ieee.org/xpl/articleDetails.jsp?arnumber=7039614.

[Santos et al., 2007] Santos, P. G. d., Garcia, E., and Estremera, J. (2007). *Quadrupedal Locomotion: An Introduction to the Control of Four-legged Robots*. Springer Science & Business Media.

[Shepard, 1968] Shepard, D. (1968). A Two-dimensional Interpolation Function for Irregularly-spaced Data. In *Proceedings of the 1968 23rd ACM National Conference*, ACM '68, pages 517–524, New York, NY, USA. ACM. Available from: http://doi.acm.org/10.1145/800186.810616.

[Smith, 2012] Smith, M. K. (2012). *Common mistakes in using statistics: Spotting and avoiding them*. Accessed: 2015-05-06. Available from: https://www.ma.utexas.edu/users/mks/statmistakes/terminologyrevariability.html.

[Sugihara, 2009] Sugihara, T. (2009). Standing stabilizability and stepping maneuver in planar bipedalism based on the best COM-ZMP regulator. In *IEEE International Conference on Robotics and Automation, 2009. ICRA '09*, pages 1966–1971.

[Talkner et al., 1987] Talkner, P., Hanggi, P., Freidkin, E., and Trautmann, D. (1987). Discrete dynamics and metastability: Mean first passage times and escape rates. *Journal of Statistical Physics*, 48(1-2):231–254. Available from: http://link.springer.com/article/10.1007/BF01010408.

[Tedrake, 2004] Tedrake, R. (2004). *Applied Optimal Control for Dynamically Stable Legged Locomotion*. PhD thesis, Massachusetts Institute of Technology.

[Tucker, 1975] Tucker, V. A. (1975). The Energetic Cost of Moving About: Walking and running are extremely inefficient forms of locomotion. Much greater efficiency is achieved by birds, fish and bicyclists. *American Scientist*, 63(4):pp. 413–419. Available from: http://www.jstor.org/stable/27845576.

[Ugurlu and Kawamura, 2012] Ugurlu, B. and Kawamura, A. (2012). Bipedal Trajectory Generation Based on Combining Inertial Forces and Intrinsic Angular Momentum Rate Changes: Eulerian ZMP Resolution. *IEEE Transactions on Robotics*, 28(6):1406–1415.

[Veendrick, 1980] Veendrick, H. J. (1980). The behaviour of flip-flops used as synchronizers and prediction of their failure rate. *IEEE Journal of Solid-State Circuits*, 15(2):169–176.

[Vukobratovic and Borovac, 2004] Vukobratovic, M. and Borovac, B. (2004). Zero-moment point - thirty five years of its life. *International Journal of Humanoid Robotics*, 1(01):157–173. Available from: http://www.worldscientific.com/doi/abs/10.1142/S0219843604000083.

[Westervelt et al., 2007] Westervelt, E., Chevallereau, C., Morris, B., Grizzle, J., and Ho Choi, J. (2007). *Feedback Control of Dynamic Bipedal Robot Locomotion*, volume 26 of *Automation and Control Engineering*. CRC Press. Available from: http://www.crcnetbase.com/isbn/9781420053739.

[Westervelt et al., 2003] Westervelt, E., Grizzle, J. W., and Koditschek, D. (2003). Hybrid zero dynamics of planar biped walkers. *IEEE Transactions on Automatic Control*, 48(1):42–56. Available from: http://ieeexplore.ieee.org/stamp/stamp.jsp?tp=&arnumber=1166523.

[Yadukumar et al., 2012] Yadukumar, S., Pasupuleti, M., and Ames, A. (2012). Human-inspired underactuated bipedal robotic walking with AMBER on flat-ground, up-slope and uneven terrain. In *2012 IEEE/RSJ International Conference on Intelligent Robots and Systems (IROS)*, pages 2478–2483.